

STRUCTURAL CHARACTERISTICS OF A SUBDUCTING OCEANIC PLATE OFF
WESTERN CANADA

by

DAVID ANTHONY WALDRON

B.A. (honours Theoretical Physics), Cantab, 1980

A THESIS SUBMITTED IN PARTIAL FULFILMENT OF
THE REQUIREMENTS FOR THE DEGREE OF
MASTER OF SCIENCE

in

THE FACULTY OF GRADUATE STUDIES
Department Of Geophysics And Astronomy

We accept this thesis as conforming
to the required standard

THE UNIVERSITY OF BRITISH COLUMBIA

December 1982

© David Anthony Waldron, 1982

In presenting this thesis in partial fulfilment of the requirements for an advanced degree at the University of British Columbia, I agree that the Library shall make it freely available for reference and study. I further agree that permission for extensive copying of this thesis for scholarly purposes may be granted by the head of my department or by his or her representatives. It is understood that copying or publication of this thesis for financial gain shall not be allowed without my written permission.

Department of Geophysics and Astronomy.

The University of British Columbia
1956 Main Mall
Vancouver, Canada
V6T 1Y3

Date 20th December 1982

Abstract

The plate tectonic regime off the southwest coast of British Columbia is convergent; the oceanic Juan de Fuca and Explorer plates are obliquely subducting beneath the continental America plate. To investigate the structural complexity of this region, the Vancouver Island Seismic Project was conducted in August 1980. The principal component of this project was a reversed refraction profile perpendicular to the continental margin, extending 350 km from the America plate to the deep ocean of the Juan de Fuca plate. This work deals with the marine section of the profile. Data from large explosive sources and an airgun were recorded on three ocean bottom seismographs (in the deep ocean, on the continental rise and on the shelf). Continuous seismic reflection profiles complemented the refraction information. To adequately model the seismic structure of this complex region required the application of ray-tracing procedures and a synthetic seismogram technique, based on asymptotic ray theory, for laterally varying media. Consistency between the seismic interpretation and previously published gravity anomaly variations across the margin was verified with the aid of empirical velocity-density relations. Additional seismic constraints were provided by multichannel reflection sections and sonic log data from a nearby well.

The aim of all procedures for data modelling was to obtain velocity and density models which had the least structure consistent with all available geophysical information. The interpreted structural section indicates that

the sediments thicken from 1 km in the deep ocean to 2 km at the base of the continental rise, where the eastward dip of the oceanic basement increases from 1.4° to about 3° and sediment velocities increase landwards. A stratified upper crustal velocity sequence has been derived below the deep ocean which is similar to that deduced from other studies on the Juan de Fuca plate. This stratification is discordant with the descending oceanic plate further east; it is replaced by a block of relatively low velocity material beneath the continental rise. This unit is interpreted to be a highly sheared and compressed *mélange*. Lower crustal structure remains constant over the entire marine profile, suggesting that the *mélange* material may have been formed as upper crustal layers were scraped off the descending oceanic plate. The lower crust has been modelled as a constant velocity gradient region, extending down to approximately 9 km below sea floor in the deep ocean. At this depth there is a strong decrease in velocity gradient, interpreted to be the Mohorovičić discontinuity. Resolution of Moho structure is poor, but no velocity discontinuity at the boundary is required by the data. There is an increase in the dip of the Moho under the continental rise from about 1° to 6° .

The refraction data are thus explicable in terms of a relatively simple, two-dimensional velocity model, which is consistent with multichannel, well-log, and gravity information.

Table of Contents

Abstract	ii
List of tables	vi
List of figures	vii
Acknowledgements	ix
CHAPTER 1 An Introduction	
1.1 The Tectonic Regime	1
1.2 Subduction? Evidence for and against	3
1.3 Geology of the Margin	6
CHAPTER 2 On the Interpretation of Seismic Data	
2.1 Marine Refraction Data Analysis	10
2.2 Travel Time Inversions	12
2.3 Synthetic Seismograms	16
2.4 Practical Interpretation	18
2.5 The Philosophy of Modelling	24
CHAPTER 3 The VISIP-80 Data Set	
3.1 The Vancouver Island Seismic Project	25
3.2 Data Description	27
3.3 Inherent Data Errors	35
3.4 Topography Corrections	39
3.5 Comments on Data Trends	41
CHAPTER 4 Data Interpretation - a detailed description	
4.1 Summary of the Approach Taken	44
4.2 Travel Time Modelling	45
4.3 Amplitude Interpretation of OBS #1 Data	50
4.4 Practical Use of WKBJ and ART	57
4.5 Amplitude Characteristics for all Receivers	60

4.6	Construction of Final Models	62
4.7	Final Models - a detailed description	62
4.8	Interpretation Summary	75
CHAPTER 5 Gravity Interpretation		
5.1	On the Analysis of Gravity Data	76
5.2	Gravity Data Description	78
5.3	Gravity Data Interpretation	80
CHAPTER 6 Summary and Discussion		
		86
Bibliography		
		92
Appendix A	WKBJ and ART Algorithms	99
Appendix B	Instrumentation and Data Digitization	104
Appendix C	Chevron Multichannel Data	105
Appendix D	Shell Cygnet Well	110
Appendix E	Structure of the Moho	111
Appendix F	Bubble Pulse Oscillations	114
Appendix G	2-D Gravity Modelling Algorithm	116
Appendix H	U.S.G.S. Multichannel Data	119

List of Tables

1.1	History of the continental margin	9
3.1	Inherent travel time errors	36
3.2	Instrument deployment times	37
5.1	Velocity vs. density in marine sediments	78
C.1	NMO velocities for Chevron data	107
E.1	The effects of Moho structure type	112

List of Figures

1.1	Tectonic map of the margin	2
1.2	Geology of the margin	7
1.3	Ponded sediments on the rise	8
2.1	Travel time non-uniqueness	14
2.2	Transition zones - travel times	20
2.3	Transition zones - amplitudes	23
3.1	The Vancouver Island Seismic Experiment	26
3.2	CSP data	27
3.3	Raw ocean bottom seismograph data	29
3.4	Airgun data	32
3.5	Explosion data	33
3.6	Seafloor and basement topography	38
3.7	Amplitude variations: OBS #1, #3, and #5	42
4.1	A preliminary travel time model	46
4.2	Amplitude characteristics: OBS #1	52
4.3	The effect of Moho depth on amplitude	56
4.4	Comparison of WKBJ and ART algorithms	58
4.5	Amplitude trends and charge size	61
4.6	Airgun models	63
4.7	OBS #1 Travel time model	66
4.8	OBS #1 Amplitude model	67
4.9	OBS #3 Travel time model	70
4.10	OBS #3 Amplitude model	71
4.11	OBS #5 Travel time model	73
4.12	OBS #5 Amplitude model	74
4.13	Final velocity structure	75

5.1	Location map of gravity profile	79
5.2	Gravity model	82
6.1	Final velocity and density structure	87
6.2	Geological structure of the upper crust	89
C.1	Chevron Standard multichannel data	105
C.2	V-Z structure from NMO velocities	108
D.1	V-Z structure from sonic log	110
E.1	Possible velocity variations at the Moho	112
G.1	Gravitational attraction of a polygon	116
H.1	Location of U.S.G.S. multichannel section	119
H.2	U.S.G.S. data and geological interpretation	120

ACKNOWLEDGEMENTS

Many friends and colleagues have helped me in the formulation and completion of this thesis, and in the enjoyment of my two years spent in Canada.

Firstly, I thank my parents and teachers in England, together with the Canadian Commonwealth Scholarship Committee, without whose help I would never have been able to come to Canada.

Dr. R.M. Clowes, my supervisor, provided friendly advice, encouragement, and support throughout my studies. His help has been invaluable. I also wish to thank Dr. R.M. Ellis for his help during Dr. Clowes' period of work in Costa Rica. Dr. G.K.C. Clarke and Dr. D.W. Oldenburg, by means of their contagious enthusiasm, have kept very much alive my interest in other areas of geophysics. I have always found the research environment in the Department of Geophysics and Astronomy at the University of British Columbia to be superb.

I greatly appreciate the patient, knowledgeable advice of Ken Whittall in all matters seismological. I have also had numerous informative discussions with George Spence. Thanks are due to Ed Waddington for, among other things, the use of his drafting equipment; without which most of the diagrams in this thesis would be a mess. My 'army' of drafting help was formed of: Norman Avolino, Kerrie Blakeley, Mark Charnell, Maj DePoorter, Terence Sunderland and Gail Weitzman.

Diane Donnelly became a source of amazement in the computer room for the speed and accuracy with which she typed this manuscript; I am very grateful to her for her fast fingers and quick wit.

Invaluable editorial comments were provided by Dr. R.M. Clowes and Dr. G.K.C. Clarke; I greatly appreciate their patient and thorough readings of this work.

The cooperation of the scientific staff at the Pacific Geoscience Centre on Vancouver Island was invaluable; without the use of their OBSs the data would not have existed. The Canadian Forces through the Defense Research Establishment Pacific provided the CFAV Endeavour, making the marine component of VISP-80 possible. The assistance of the Fleet Diving Unit, Pacific Maritime Command, who detonated the explosive charges at sea is appreciated.

Personal financial support was provided by a Canadian Commonwealth Scholarship. Principal support for the study was provided by EMR research agreements (Earth Physics Branch) 214/3/81 and 42/3/82. Additional funding was provided by NSERC operating grant #A7707 and strategic grant #G0738.

" We shall not cease from exploration,
And the end of our exploring,
Will be to arrive where we started,
And know the place for the first time."¹

¹T.S. Elliot, Little Gidding.

" What we call the beginning is often the end
And to make an end is to make a beginning.
The end is where we start from¹."

CHAPTER 1 AN INTRODUCTION

1.1 Plate Tectonics off the West Coast of British Columbia, Canada.

In the Vancouver Island region the plate tectonic regime is dominated by the relative motions of three main lithospheric plates: the Pacific, America and much smaller, intervening, Juan de Fuca plate system (see figure 1.1). A small northern part of this system, the Explorer plate, has been shown to be moving independently (Riddihough, 1977). Based on magnetic anomaly patterns, the current perpendicular convergence rates are about 3 cm yr⁻¹ for the Juan de Fuca-American and less than 2 cm yr⁻¹ for the Explorer-American plates, thereby producing left-lateral strike-slip movement along the Nootka fault zone at a rate of about 2 cm yr⁻¹ (Hyndman et al., 1979). Juan de Fuca ridge system consists of numerous en-echelon spreading axes, offset by short transform segments. Across this boundary the present full spreading rate of motion ranges from about 4 cm yr⁻¹ to 6 cm yr⁻¹.

Tectonic evolution of the western Pacific margin has been discussed by Atwater (1970), whilst the geological implications of changes in plate configuration are discussed by Muller (1977).

¹T.S. Elliot.

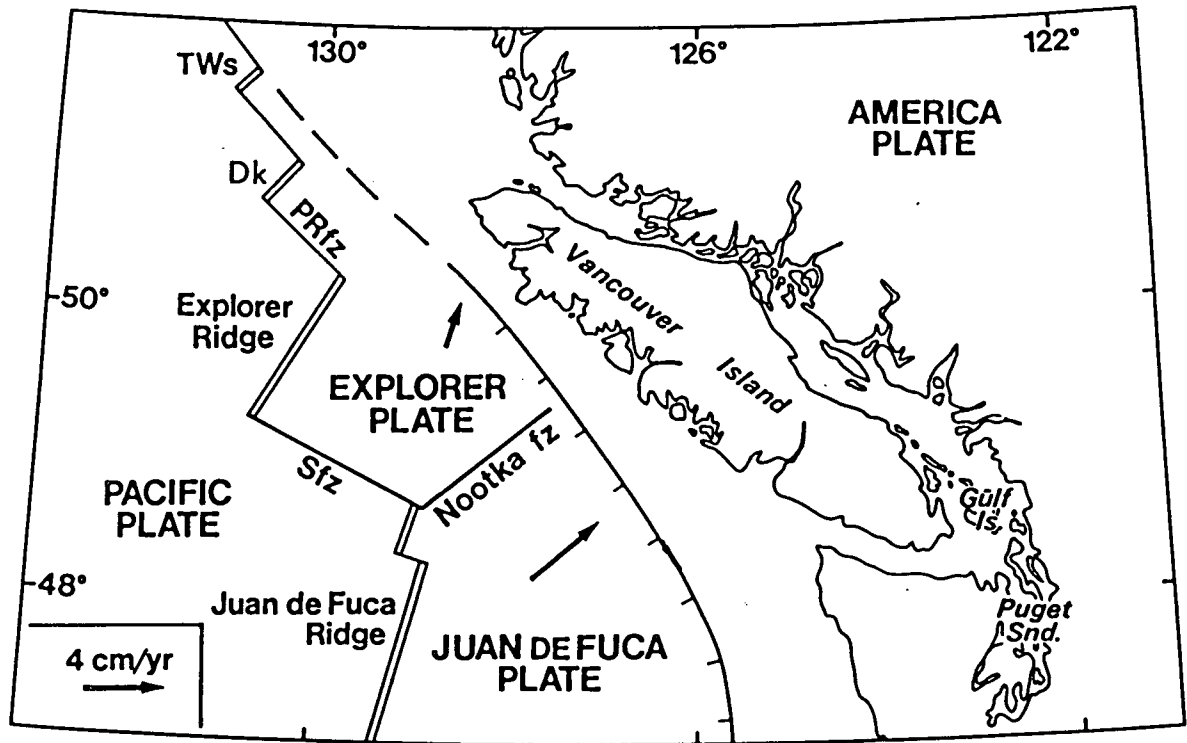


Figure 1.1 A tectonic map of the southern British Columbia continental margin.

The main lithospheric boundaries and plate motions relative to North America held stationary are shown. TWs = Tuzo Wilson knolls; PRfz = Paul Revere fracture zone; Sfz = Sovanco fracture zone, Dk = Dellwood knolls.

In the past few tens of millions of years the tectonic regime of the western Canadian margin has changed rapidly, leaving a very complex geological record. It has been well established that subduction has occurred along the west coast of British Columbia, Washington and Oregon in the past few million years, but there has been debate as to whether it continues at present, and if it does, whether it is happening in an aseismic manner (Crosson, 1972; Riddihough and Hyndman, 1976; Keen and Hyndman, 1979; Ando and Balazs, 1979; Savage et al., 1981; Hyndman and Weichert, 1982; Riddihough et al., 1982).

1.2 Subduction ? Evidence for and against

The continental margin off Vancouver Island shows a number of features which are uncharacteristic of subduction zones around the world. There is no deep margin trench, no deep earthquake suite in a Wadati-Benioff zone, or thrust fault-mechanisms beneath the continental slope and shelf; and there is limited activity in the Cascade volcanic chain.

It is generally believed that because of the proposed very slow sinking rate (3 cm yr^{-1}) and the young, thin nature of the subducting Juan de Fuca plate, many of the phenomena normally associated with subduction will either be absent or not detectable (Keen and Hyndman, 1979). However there are a number of pieces of evidence supporting current subduction beneath Vancouver Island:

- 1) The existence of old ($>10 \text{ Ma}$) magnetic lineations west of the Juan de Fuca ridge axis, but not to the east. The required symmetry in sea-floor spreading implies that older parts of the plate have disappeared beneath the continent (Vine, 1966; Morgan, 1968).

- 2) Compressive deformation of sediments on the continental slope west of Vancouver Island postulated to result from underthrusting of the America plate by the Juan de Fuca plate (e.g. Tiffin et al., 1972; Barr, 1974). The continental slope changes in character southwards from steep and narrow off the Queen Charlotte Islands and northern Vancouver Island to a much wider,

irregular slope off southern Vancouver Island, Washington and Oregon (figure 1.2). This seems to indicate a change in the interaction regime along the margin from transform faulting in the north to compression and subduction in the south.

3) A 'down-to-the-east' crustal tilt rate across western Washington is implied by precise levelling over a 70 year period. Ando and Balazs (1979) suggest that this tilt rate indicates aseismic slip in the Juan de Fuca plate subduction zone: which may have been continuous from 0.25 Ma (Adams and Reilinger, 1980). The lack of any major thrust earthquakes during the period of tidal and levelling observations is used by Ando and Balazs as evidence for aseismic subduction. Interpretation of the geodetic relevening data is still being debated; a review is given by Riddihough (1982).

4) The Nootka fault zone (Hyndman et al., 1979; Au, 1981) is approximately perpendicular to the margin. Left-lateral strike-slip motion along this fault requires compression along the margin to the south or sea floor moving away from the margin to the north. The latter possibility is very unlikely.

5) The gravity field shows the characteristic low and high gravity bands of active subduction zones, although the trench is much reduced by the complete sediment

infill (Riddihough, 1979).

6) The heat-flow pattern for southwestern British Columbia and for western Washington and Oregon exhibits the characteristic subduction zone pattern: a band of low heat flow extends from the trench to the volcanic arc about 200 km inland, and a much higher than normal heat flow extends for a considerable distance inland (Hyndman, 1976).

7) The oceanic basement is observed to dip under the continental rise, forming a sediment-filled trench; thereby implying subduction.

8) The andesitic volcanism of the Cascade mountains suggests the existence of a down-welling oceanic plate. Relatively recent volcanism implies that subduction has occurred and has continued up to at least 1 Ma ago (Riddihough and Hyndman, 1976).

9) There is a concentration of seismicity in the Puget Sound lowlands with a truncation of seismicity to the north at the 49th parallel (Rogers, 1982)- indicating some form of tectonic activity. The maximum depth of earthquakes in the region is about 60 km. This uncharacteristically shallow depth is thought to be due to the slow rate of convergence and the thin plate involved (Riddihough and Hyndman, 1976).

It is very difficult to detect 'present' subduction. Each source of geophysical information has a different time scale. Offshore magnetic anomalies can give information back several tens of million years, but their time resolution is little better than 1 Ma; earthquake data extend back only about 80 years (Rogers, 1982) and represent a very short, recent time interval.

In summary, the boundary between the America and Juan de Fuca plates is thought to be a zone of convergence or subduction, with underthrusting probably starting near the base of the continental slope with rates from 1 to 3 cm yr⁻¹.

1.3 Geology of the Margin

The continental margin off southern Vancouver Island consists of two distinct regions; the Cascadia and Tofino basins, separated by the continental slope (figure 1.2).

Cascadia Basin forms the Abyssal plain, bounded to the east by the continental rise, and to the west by the Juan de Fuca ridge. The oceanic basement here dips to the east and is conformably overlain by a hemiterogeneous¹ sequence formed in late Miocene-Pliocene time (Scholl, 1974). These beds are overlain by a landward-thickening turbidite wedge, formed during the last 1.0 Ma (Carson, 1973).

The continental slope has an average width of 70 km and

¹A hemiterogeneous sequence is composed chiefly of erosional detritus or pyroclastic debris, derived from a nearby landmass, and there is also a pelagic component.

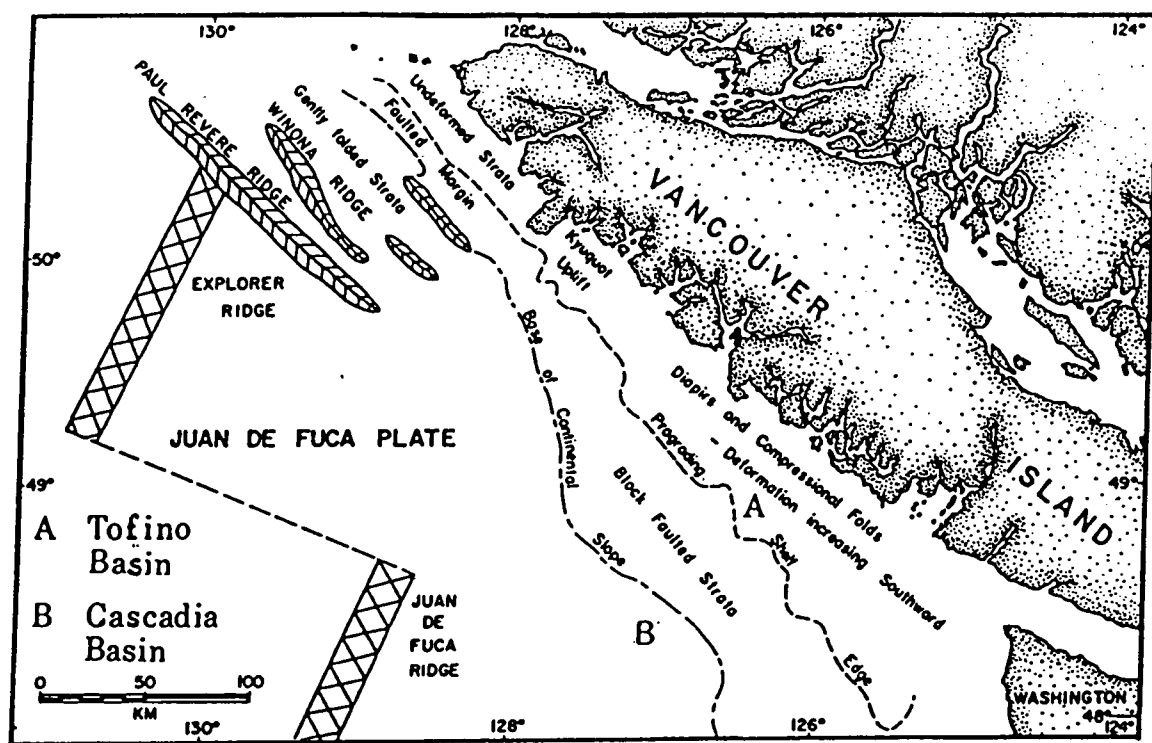


Figure 1.2 Near-surface structures of the continental margin. (after Tiffin et al., 1972)

The positions of Tofino and Cascadia Basins are shown. Note the increase in deformation southward on the continental shelf.

is composed of Quaternary and upper Tertiary strata which are deformed into a series of asymmetric folds and northeastward-dipping imbricate thrusts (Snively and Wagner, 1981). The lower slope is composed of deformed and uplifted Cascadia Basin strata forming discontinuous ridges, in general fault-bounded, behind which sediments are ponded, thereby subduing the relief (Barr, 1974; figure 1.3).

Tofino basin is a large Tertiary depositional area lying to the east of the continental slope. There are thick sequences of late Eocene to Pliocene mudstones containing abundant foraminifera (Tiffin et al., 1972) which indicate a bathyal depositional environment throughout most of the

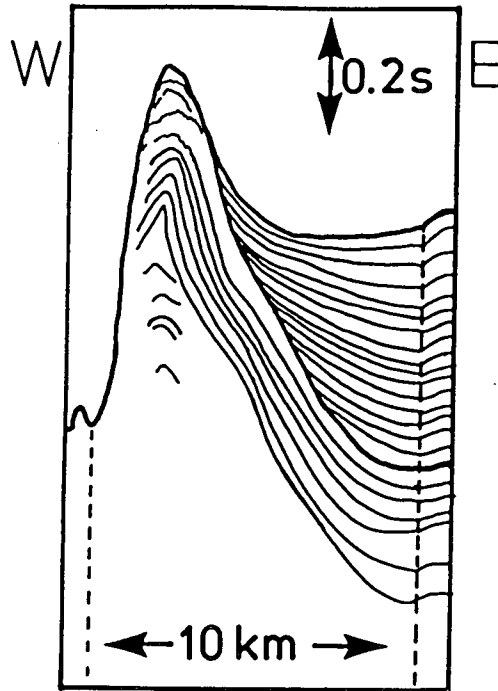


Figure 1.3 Poned sediments on the continental rise.

A line-drawing interpretation of part of the CSP profile (figure 3.2) has been made. The dashed lines are probable faults. Note the unconformity surface between the eastward flank of the ridge and the ponded sediments.

Tertiary. Subsequent uplift has exposed the deep water sediments on the shelf over much of the area. Eocene-Oligocene sediments occur in a belt along the inner shelf, while Miocene and Pliocene rocks lie seaward of this.

Snavely and Wagner (1981) propose the existence of a mass of highly sheared and compressed *mélange*¹ lying beneath the sediments of the continental rise. They name this unit the "Hoh *Mélange*" (middle Miocene), which is thought to have been

¹Definition of a *mélange*: A heterogeneous medley or mixture of rock materials. A mappable body of deformed rocks consisting of a pervasively sheared, fine-grained, commonly pelitic matrix, thoroughly mixed with angular and poorly sorted inclusions of native and exotic tectonic fragments, blocks or slabs.

uplifted prior to deposition of the continental slope Pliocene strata.

Comprehensive reviews of the geology of the continental margin may be found in Tiffin et al. (1972), or Chase et al. (1975). Shouldice (1971) has compiled a depositional history of the continental margin, which is summarized below.

Geologic Time	Depositional environment
Recent Pleistocene Pliocene	Regression in upper Pliocene Lesser one in lower Pliocene
Miocene	Major transgression in upper Miocene. Period of regression, crustal deformation, and uplift.
Oligocene	Transgressions of Oligocene and lower Miocene seas
Eocene	Widespread lower - middle Eocene submarine volcanic activity. Initial uplift followed by subsidence in late Eocene.
> Cretaceous	Mesozoic sediments. Intrusive and extrusive igneous features.

Table 1.1 History of the continental margin.

" It requires a very unusual mind to undertake analysis of the obvious'."

CHAPTER 2 ON THE INTERPRETATION OF SEISMIC DATA

2.1 Marine refraction data analysis - general comments.

In the analysis of seismic refraction data there are three groups of factors, which by their nature prevent a complete, accurate inversion:

- 1) Errors associated with the data
- 2) Real earth violation of simplifying assumptions
- 3) Limits on the resolution of velocity structures

1) The exact positions of source and receiver are not known in marine work. The magnitude of the distance errors varies with the type of receiver used (c.f. a fixed OBS and a drifting sonobuoy). In general, all shot locations and receiver positions are determined from near shore navigation systems supplemented by satellite checks. For studies off the west coast of Canada, the relative position accuracy is then 200 m with greater uncertainties in absolute position (Hyndman et al., 1979).

There are intrinsic timing errors associated with the receiver clock and shot detonation time, as well as travel time picking errors of first arrivals. Due to the lengthy nature of the marine seismic source wavelet (Appendix F), the picking of secondary arrivals is usually difficult and often

impossible. Thus certain sources of definitive information may be lost entirely, e.g. sub-critical reflections.

2) In all modelling of seismic data, simplifying assumptions restrict the range of possible earth structures and enable the use of standard analysis techniques. In most cases the simplification is to assume that velocity varies only with depth, i.e. a one-dimensional structure. The real earth is often highly variable; even at flat-lying, seemingly uncomplicated sites, heterogeneity can be inferred on a scale of kilometres (Spudich and Orcutt, 1980). Shot-to-shot random variations in amplitude give evidence of lateral variations in structure (e.g. Fowler and Keen, 1978). Even when two-dimensional models are considered, these can only be a very simple approximation to the real earth.

3) All seismic waves have finite, non-zero wavelength λ ; turning rays are therefore unable to resolve structural details which are smaller than about 1λ . The acoustic properties of a heterogeneous medium are averaged when a seismic wave passes through and, consequently, different earth structures having the same velocity profile when averaged over λ will be indistinguishable when viewed by seismic waves with wavelength λ . Typically, the wavelengths used to study the crust range from 0.5 to 2 km for explosive sources, 0.1 to 2 km for airguns and 0.5 m for downhole velocity-logging devices. In the majority of crustal material, velocity (and therefore wavelength) increases with depth. Thus, the maximum possible resolution that may be obtained decreases with depth.

The other intrinsic limit on the resolving power of the data is the spatial separation of the sources and/or receivers employed. The discrete nature of the information obtained makes identification of cross-over points between two branches in the travel time-distance graph accurate at best to the value of the separation between traces. Subtle changes in amplitude with distance may not be identified with confidence unless a reasonably dense sampling interval is obtained.

2.2 Travel Time Inversions

An important simplifying assumption is usually made: that the velocity c varies only with depth z i.e. one-dimensional structure.

With this restriction on possible models, the Herglotz-Wiechert formulae may be derived (Herglotz, 1907; Wiechert, 1904):

$$X(p) = 2 \int_0^{z(p)} \frac{p dz}{[(c(z))^{-2} - p^2]^{1/2}} \quad \text{where } \begin{array}{l} p = \text{ray parameter} \\ z(p) = \text{bottoming depth} \\ (p = dT/dX) \end{array}$$

$$T(p) = 2 \int_0^{z(p)} \frac{(c(z))^{-2} dz}{[(c(z))^{-2} - p^2]^{1/2}}$$

These expressions are a formulation of the forward problem: for a given model $c(z)$, the data $T(X)$ may be derived.

There is a construction method for the inverse problem: Abel's solution.

It may be shown that: (see Aki and Richards, 1980).

$$z(c) = -\frac{1}{\pi} \int_{c_0^{-1}}^{c^{-1}} \frac{X(p) dp}{[p^2 - c^{-2}]^{1/2}} \quad \text{where } c_0 = \text{velocity at } z = 0$$

This is an exact solution of the inverse problem: given data $X(p)$ we may derive the velocity-depth structure $z(c)$.

It would seem that one-dimensional travel time inversion, using the above formula, is a straightforward, purely mechanical procedure. In practice, the Abel inverse solution may not be used directly as the 'real' data are discrete, noisy, and band-limited. Even given a hypothetical situation where there were 'perfect' data, i.e. continuous, accurate and full-band; if only first arrivals are picked there might still be problems. Regions of rapid velocity increase with depth lead to triplications in the $T(X)$ curve. In order to derive a continuous $X(p)$ curve from the data both the normal and receding branches must be correctly identified, i.e. some later phases must be picked. An example of the non-uniqueness of solutions in this type of structure is given by Healey (1963); the data and possible models are shown in figure 2.1. Depth uncertainties from seismic first arrival travel times are discussed by Berry (1971).

In order to cope with the noisy and discrete nature of the data, travel time inversion techniques employ weighting and interpolation schemes. The reparameterization of travel time data, $T(X)$, into the delay time function - ray parameter domain, $\tau(p)$ (where $\tau(p) = T(p) - pX(p)$), is frequently

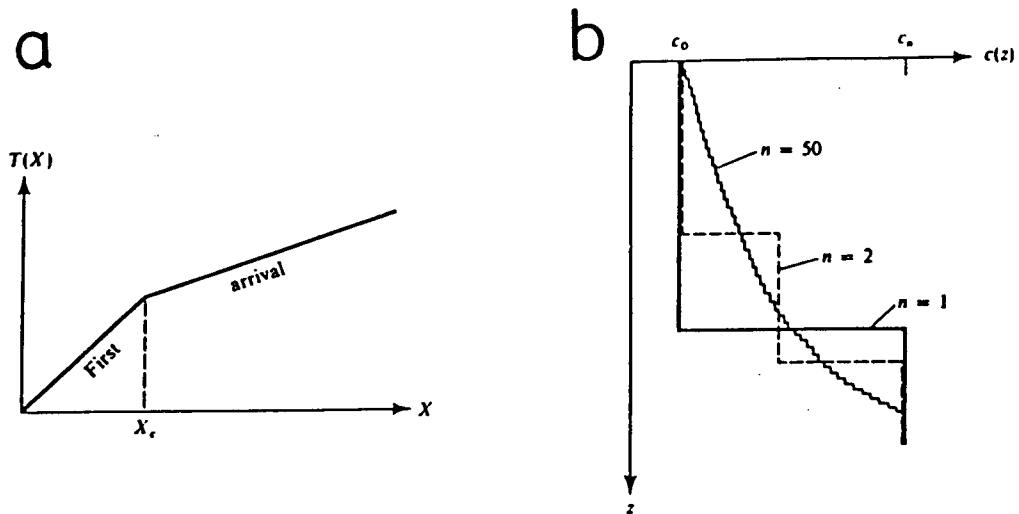


Figure 2.1 The non-uniqueness of first arrival travel time interpretations (after Healy, 1963).

- a) Travel time of the first arrival is known as shown here, but those of later arrivals are unknown.
 b) Velocity distributions that give the same first-arrival times as shown in (a); n is the number of layers.

performed (e.g. Kennett, 1976; Bates and Kanasewich, 1976). Use of this function is advantageous since it is single-valued and a monotonically decreasing function of p (McMechan and Wiggins, 1972). Also, it has been noted (Johnson and Gilbert, 1972) that first order errors in p only propagate to second order errors in τ , which is important for the construction of $\tau(p)$ from the data, $T(X)$.

Three one-dimensional travel time inversion schemes are summarized below:

- 1) Nonlinear extremal bounds (Bessonova et al., 1974). 'Averaging' operators are passed along the $\tau(p)$ bounds to obtain upper and lower bounds on possible velocity depth distributions. The derived extremal bounds are

very broad (Spudich and Orcutt, 1980; Au, 1981) and consequently are virtually useless for obtaining results of geophysical interest. Greater constraints may be placed on the extremal bounds with the addition of $X(p)$ data (Orcutt et al., 1980; and Jurkevics et al., 1980), but as the aim in most studies is to obtain a starting model for synthetic seismogram calculations, the small improvement with the $X(p)$ data addition is not significant.

2) Linearized inversion (Johnson and Gilbert, 1972). In this method an iterative improvement is made to a trial velocity-depth profile until the calculated $\tau(p)$ values lie within the error bounds for the observed τ . The final model has the tendency to minimize velocity gradients. This approach is summarized by Kennett and Orcutt, 1976; Kennett, 1976; and Cheung, 1978.

3) Linear programming inversion (Garmany et al., 1979). For this procedure, classes of extremal solutions are considered for which the depth to a given velocity is maximized or minimized subject to a finite number of data constraints. All models within the derived bounds do not satisfy the data, but any velocity within or on these bounds is realizable by at least one of the infinity of possible solutions, i.e. no v - z points can be discarded as unrealistic. The main advantage of this technique is that computation is very fast and

economical and a starting model for amplitude studies is easily obtained. This method is summarized by Au (1981).

2.3 Synthetic Seismograms

The amplitude of a seismic waveform is a potential source of information regarding earth structure through which the wave has passed. Amplitude interpretation is usually a trial-and-error, forward modelling procedure in which synthetic seismograms are subjectively compared to observed records. Work on the direct inversion of seismograms for velocity structure is currently being undertaken by C.H. Chapman and J. Orcutt. Clayton and McMechan (1981) have developed a method which does not directly utilize seismic wave amplitudes, but in which the whole data wave field is linearly transformed from the time - distance domain into the slowness - depth domain, where the velocity profile can be picked directly.

In formulating synthetic seismogram algorithms, assumptions are always made to simplify computation. The most common assumption made is that the earth is laterally homogeneous.

It is necessary to evaluate an expression of the form:

$$u(r,t) = \int ds e^{st} f(s) \int_{\Gamma} dk F(s,k) J_n(kr)$$

t transform r transform

↑ ↙ ↑ ↘ ↑ ↘

Displacement range Fourier or Laplace transform of the source time function Function describing wave propagation Bessel function

There are a number of methods available for computing a synthetic seismogram, given a one-dimensional velocity and density structure for an earth model:

- a) WKB method (Chapman, 1978; Appendix A)
- b) Reflectivity method (Fuchs and Muller, 1971)
- c) Generalized Ray Theory (GRT): (Wiggins and Helmberger, 1974)
- d) Full wave theory (FWT) (Richards, 1973; Choy, 1977)
- e) Disc-ray theory (DRT) (Wiggins, 1976)
- f) Asymptotic Ray Theory (ART) (Krebes and Hron, 1980)

These methods differ primarily in:

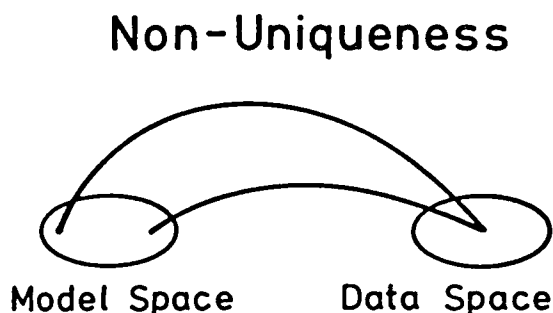
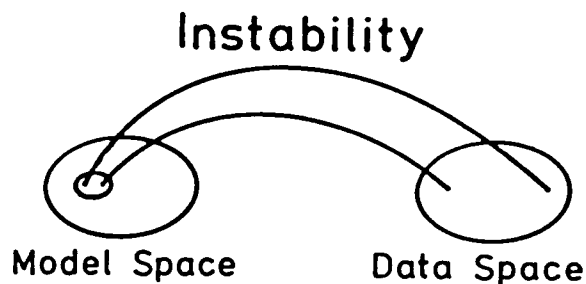
- i) the degree of approximation used in deriving F ,
- ii) the order in which the integrals over k and s are performed,
- iii) the path of integration, Γ .

There is always a trade-off between accuracy and expense.

Extensive reviews of the various methods can be found in Chapman (1978) and Richards (1979), while a comparison of the practical application of some methods is given by Spudich and Orcutt (1980). There are two inherent difficulties involved in the current use of synthetic seismograms for forward modelling purposes: instability and non-uniqueness.

Instability

The relation of the seismograms to the velocity models is non-linear and unstable, since small changes in the trial velocity models sometimes produce large changes in the resulting synthetic seismogram.



Non-uniqueness

The trial-and-error modelling technique yields no reliable error estimates on the velocity models which it produces. The solutions are inherently non-unique: two widely different models may produce the same theoretical data. True appraisal is not possible with the trial-and-error forward modelling approach

2.4 Practical Interpretation

2.4.1 Travelttime interpretation

The inability of discrete, noisy, band-limited travel time data to resolve details of the form of a velocity-depth distribution is well known (see for example Spudich and Orcutt, 1980). A clear illustration of the wide range of models which may be found to fit any given set of real travel time data is the computation of extremal bounds (see section

2.2). These limits are always found to be very broad, due to the relatively large errors inherent in the data.

The practical resolution that may be obtained with travel time data is illustrated in figure 2.2. The solid lines forming a triplication (a to d) represent the travel times through the mean oceanic crust (MOC) model of Raitt (1963, upper left). Synthetic travel time data have been calculated from gradient models which provide various rates of transition from the 6.69 to 8.1 km/s velocities of Raitt's model. It can be clearly seen from figure 2.2 that the most diagnostic feature of a rapid transition zone is the presence of secondary arrivals in the triplication region. A discrete boundary is only distinguishable from a 1 km thick transition region by the presence of sub-critical reflections (produced by the boundary, figure 2.2a), and from a 4 km transition zone by the presence of wide-angle reflections (to within 0.1 s error for mantle arrivals, figure 2.2c). It is also clear that if the travel time errors are large (>0.15 s) at offset distances greater than 50 km (perhaps due to complex structure), then an 8 km transition zone model is consistent with the first arrival travel time data (figure 2.2d).

Thus, the diagnostic characteristics of the travel time data are usually the secondary arrivals which, as has been noted (section 2.1, and appendix F) are often difficult or impossible to identify.

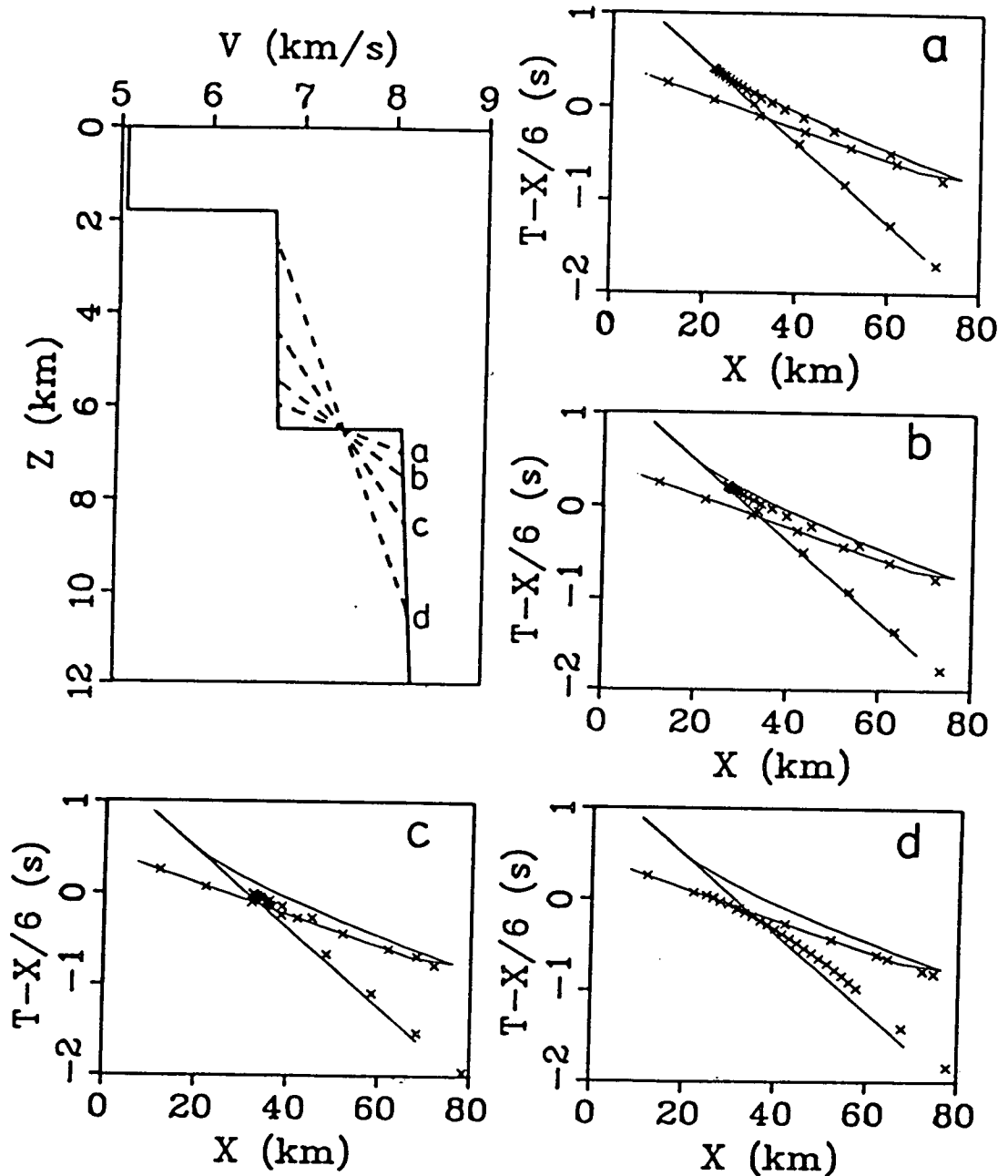


Figure 2.2 Transition zone characteristics and travel times.

Upper left: The solid line is the mean oceanic crust model (MOC) of Raitt (1963). A slight gradient has been introduced into the original constant velocity regions to generate turning rays there. The dashed lines, a, b, c, and d represent increasingly more gradual transitions from 6.69 km/s to 8.1 km/s.

In the four diagrams, a, b, c, and d; the crosses represent travel times through the transition zone velocity model as compared to travel times through the MOC model - shown by the solid line.

- a) 1 km thick transition zone (TZ).
- b) 2 km TZ.
- c) 4 km TZ.
- d) 8 km TZ.

2.4.2 Amplitude Interpretation

The observed amplitude of a seismic waveform depends upon three groups of factors:

- i) characteristics of the source
- ii) properties of the earth
- iii) instrument response

The influence of earth structure on seismic amplitude must be extracted from other effects in order for interpretation to proceed.

In marine refraction seismology a given data set usually consists of many sources recorded on a single receiver; the instrument response is then a constant factor. If a repetitive source is used (such as an airgun), the source function is assumed constant, enabling reliable comparison of relative trace amplitudes for a given profile. The use of explosion sources with variable charge sizes yields much more ambiguous amplitude information. Variations in trace character may then be due either to changes in sampled earth structure or the variable source characteristics. Attempts are usually made to compensate for the variation in charge size before relative amplitude modelling with explosion data. Empirical formulae relating charge size to amplitude of seismic energy generated are generally used (O'Brien, 1960; Kanestrøm and Øvrebø, 1978). The difficulty of reliably estimating these formulae is evident in this work (section 4.3) and has been noted elsewhere (e.g. Clee et al., 1974).

Relative amplitude modelling of explosion data should ideally be based upon sources of equal charge size, and if

'corrected' amplitudes are used, these should be interpreted with caution.

The proposed seismic model is invariably (by the nature of the data) a crude approximation to the real earth. Thus there may be significant unmodelled horizontal variation in structure, producing trace-to-trace amplitude variations. These should not be modelled with detailed vertical velocity structure, but traces of similar character must be grouped together and the general amplitude features modelled. Thus the more spatially dense the data are, the better the resolution which may be obtained with amplitude data.

The amplitude characteristics of gradient region variations on the mean oceanic crustal model of Raitt are shown in figure 2.3. The responses have been calculated using the WKBJ synthetic seismogram algorithm due to Chapman (1978). That the secondary arrivals are a very diagnostic feature of the data in determining the form of velocity variation is clear from the figure.

If the amplitude characteristics are clear, and the spatial density reasonably high, models which are indistinguishable on the basis of first arrival travel times become resolvable. The width of the main amplitude group (associated with wide-angle reflections) is greater the sharper the transition. The synthetic seismograms (figure 2.3) illustrate another, potentially misleading, effect - interference. There is relatively little amplitude between 40 and 50 km (figure 2.3c) due to the destructive interference between first and secondary arrivals. This occurs with the

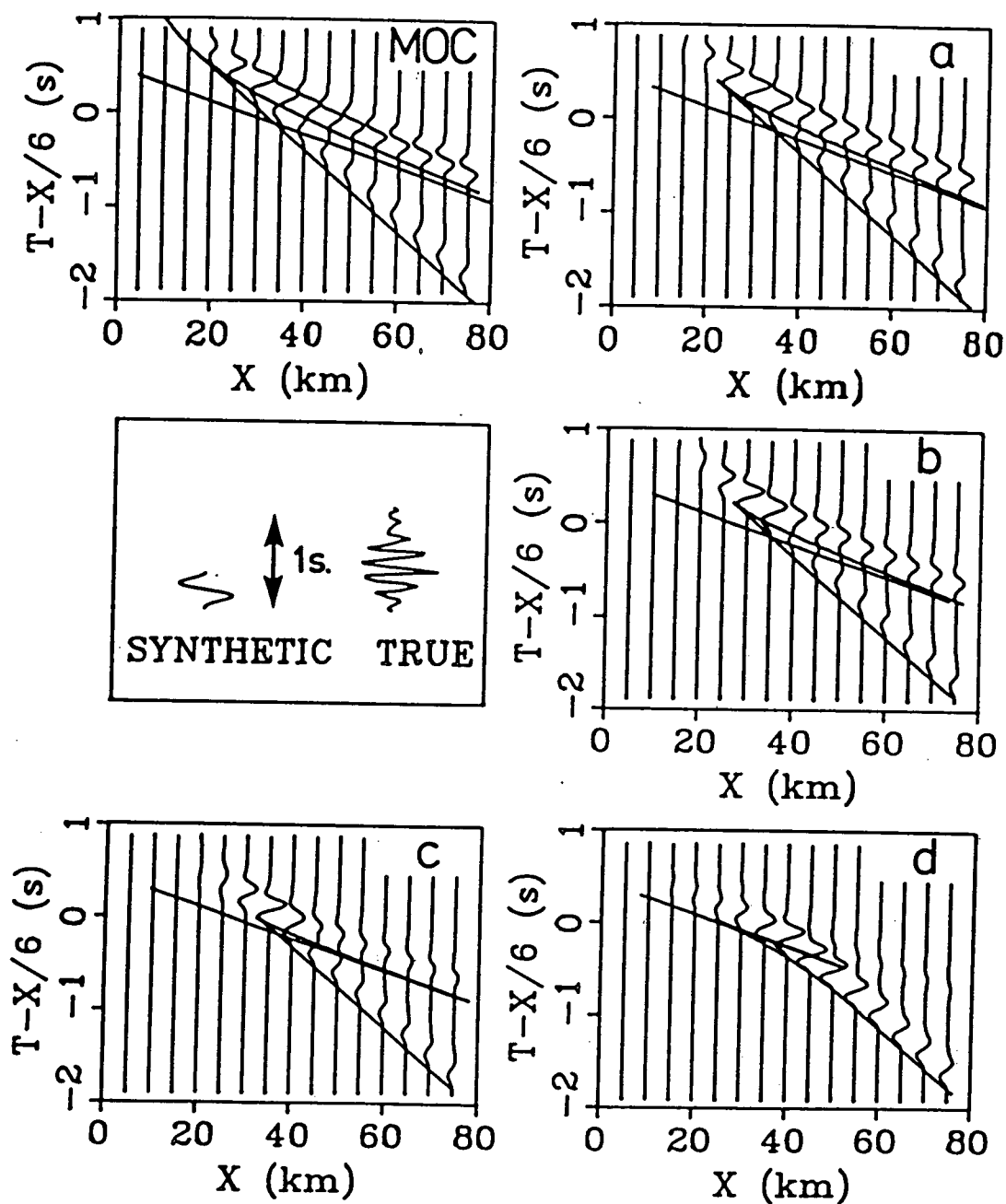


Figure 2.3 Transition zone characteristics and amplitudes.

Upper left: WKBj synthetic seismogram for the mean oceanic crust model (MOC) of Raitt (1963). Solid line links first arrival travel time points. a, b, c, and d are WKBj synthetic seismograms for the four transition zone models described in figure 2.2.

Middle left: A comparison of the relatively short synthetic wavelet used in the WKBj simulations with a typical wavelet received by an OBS (ocean bottom seismograph) from a marine explosion.

simple two lobe synthetic wavelet used, which is ~ 0.35 s in length. True marine data may have a characteristic wavelet ~ 1.0 s in length (figure 2.3; Appendix F), and thus there will be many complex interference effects between the wavelets arriving at any given point but being associated with different events. Anomalously low amplitude traces in the middle of large amplitude groups should generally be ignored as they may be the result of destructive interference, or be due to unmodelled lateral heterogeneities. Traces of this nature could equally well occur at the edges of a large amplitude group, where they would not be considered anomalously low; the amplitude group would merely be regarded as being less spatially extensive. Thus the lateral extent of large amplitude regions has this inherent uncertainty; an uncertainty which reduces the practical resolution that may be obtained between different earth models.

2.5 The Philosophy of Modelling

It is relatively easy to produce a complex velocity-depth model which is consistent with the data. Whilst it is possible that this model may represent the real earth, unless all the features are constrained by the data (or additional geophysical information), the complexity is misleading. Geological implications may be drawn from details in the velocity-depth model which could be eliminated and yet still achieve real data consistency. The aim in all seismic modelling should be to produce the v-z model which has the least structure compatible with all the data.

" The greatest tragedy of science - the slaying of a beautiful hypothesis by an ugly fact'."

CHAPTER 3 THE VISP-80 DATA SET

3.1 The Vancouver Island Seismic Project

In August 1980, CO-CRUST² conducted the Vancouver Island Seismic Project (VISP-80) which was a series of large scale refraction and reflection seismic experiments, utilizing both land-based and ocean bottom seismographs (OBSs).

The refraction program consisted of 4 profiles, lines I to IV (figure 3.1). Three of these were along strike, one on Vancouver Island, one on the continental shelf, and one in the deep ocean; and the fourth, across strike, extended from the deep ocean to the inland volcanic arc. The interpretation of the oceanic portion of this onshore-offshore profile is presented here.

To provide shallow information, continuous seismic profiling (CSP) was run with a 5 litre airgun. For successively deeper information a 32 litre airgun and explosive sources were recorded on four OBSs (1, 3, 5 and 6-2, figure 3.1). The 37 charges used on the 100 km long explosion profile ranged in size from 50 to 825 kg and were all

¹Thomas H. Huxley

²CO-CRUST (Consortium for Crustal Reconnaissance Using Seismic Techniques), in 1980, included participants from Earth Physics Branch (Ottawa), Pacific Geoscience Centre, Atlantic Geoscience Centre, and the Universities of Alberta, British Columbia, Manitoba, Saskatchewan, Toronto, and Western Ontario.

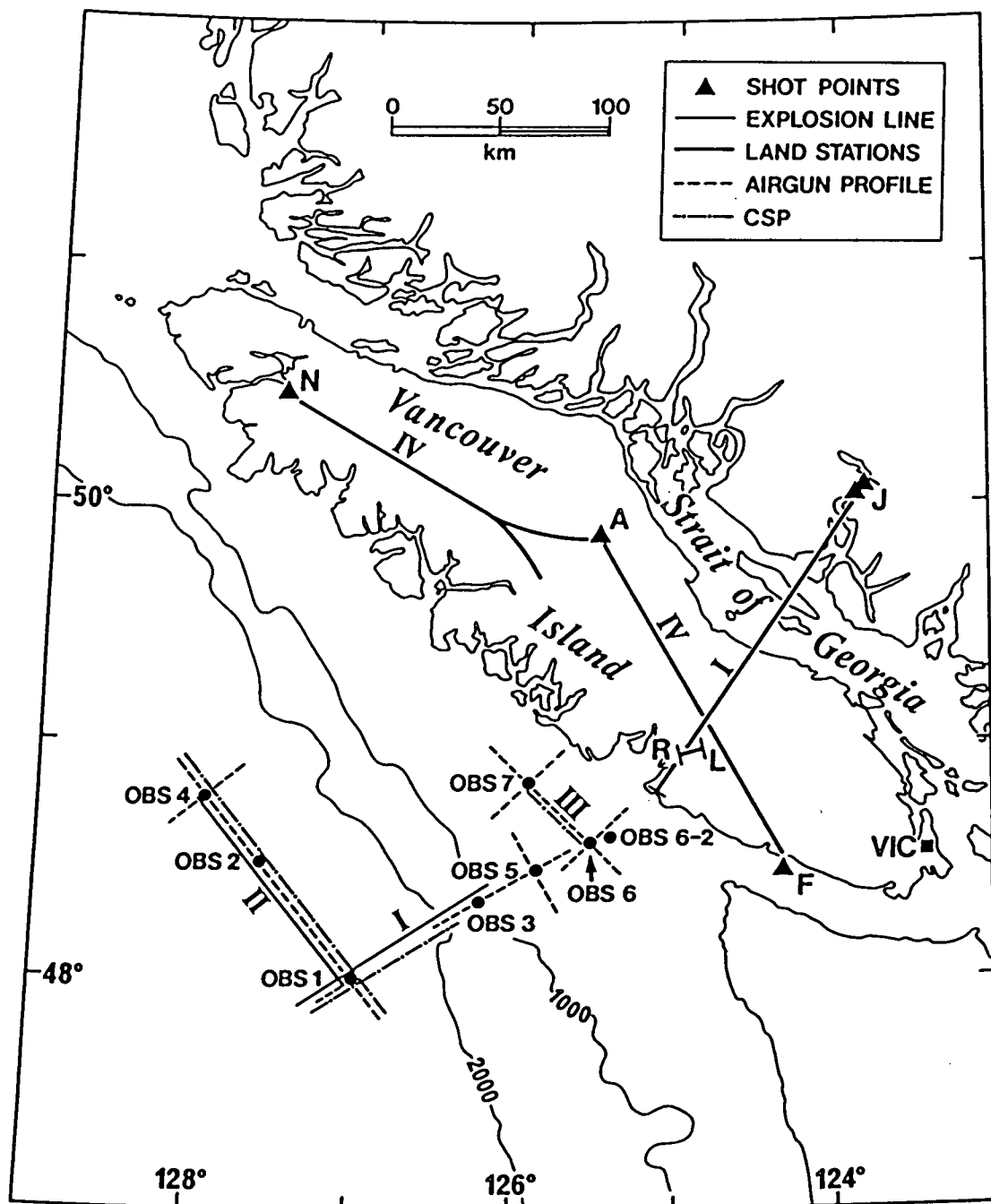


Figure 3.1 The Vancouver Island Seismic Project.

This location map shows the refraction lines (I-IV), the reflection line (RL), and the airgun and CSP lines. Bathymetry is in meters. Interpretation of the marine portion of line I is presented in this work.

detonated at a depth near the optimum for maximum seismic energy generation (Shor, 1963).

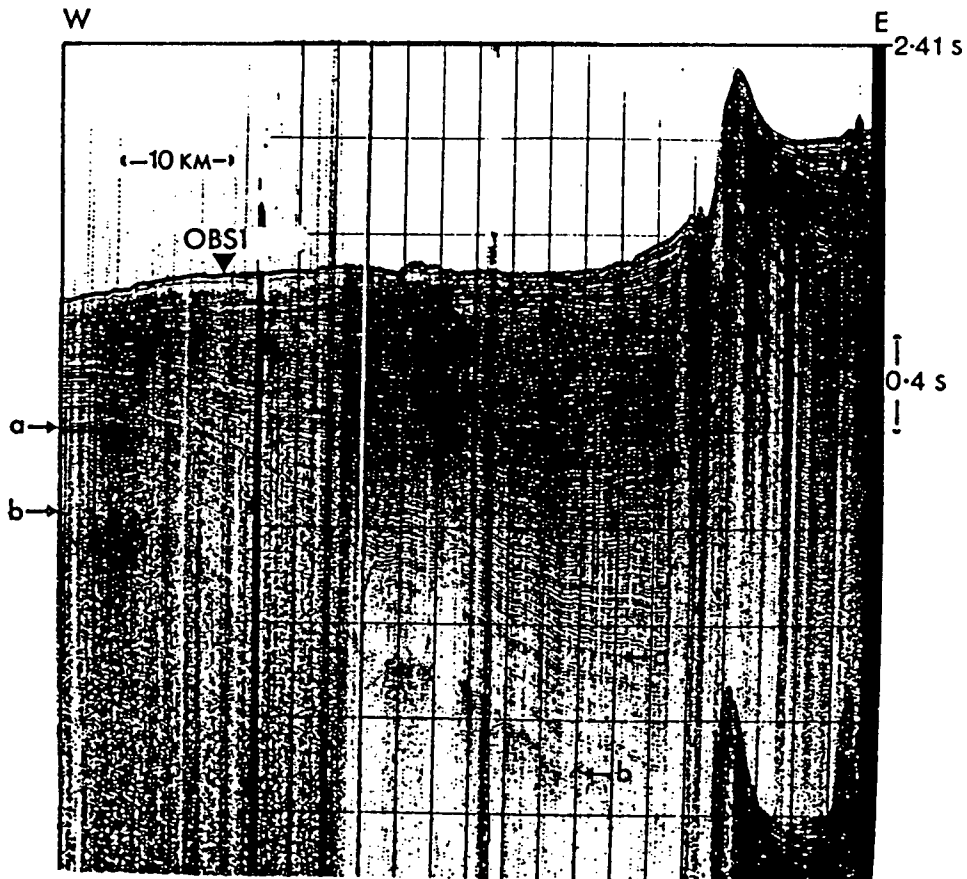


Figure 3.2 Continuous seismic profiling data along profile I

Reflections from the boundary between the late Pliocene and Quaternary sediments are indicated by 'a' and from the basement by 'b'. Note that the upper timing line is 2.41 s two way travel time, and that OBS #3 is located 9 km off the eastern end of the section.

3.2 Data Description

3.2.1 CSP Record

Continuous seismic profiling was carried out along the profile for a distance of almost 70 km west of the continental rise (figure 3.2). The section shows the basement, 'b', to be flat-lying on the westerly 8 km of the profile and then dipping at 1.4° towards the continent. The CSP over OBS1, but

perpendicular to line I, shows the basement to be faulted with raised horst structures close to the OBS position. The reflector 'a', ~ 0.4 s above the basement in figure 3.2 is thought to be an unconformity between the late Pliocene and Quaternary. The moderately deformed sediments have a dip at depth similar to the basement but become progressively more flat-lying towards the surface, and are terminated abruptly at the continental rise.

3.2.2 OBS Characteristics

The ocean bottom seismographs (OBSs) used in the VISP-80 project are described in Appendix B. Signals from two horizontal and one vertical 4.5 Hz geophones, plus an internal clock are recorded on analog magnetic tape. An example of the data from all four channels of the instrument is given in figure 3.3. There is cross-talk between the three data channels and the 20 Hz time code channel which is evidenced by the sharp peak in power close to 25 Hz (seen on the power spectrum of the noise for the vertical channel). The presence of cross-talk interference on the time channel (e.g. near the end of trace TC, figure 3.3) led to difficulties with the automatic reading of the time code via a computer algorithm.

The dominant frequency in the vertical channel seismic energy packet, shown by data in figure 3.2, is approximately 6 Hz. When bandpass filtering was applied to the data the limits used were 3 - 15 Hz. The kink in signal waveform at near-zero amplitude level is due to square root signal compression by the amplifiers, a feature which increases the dynamic range of

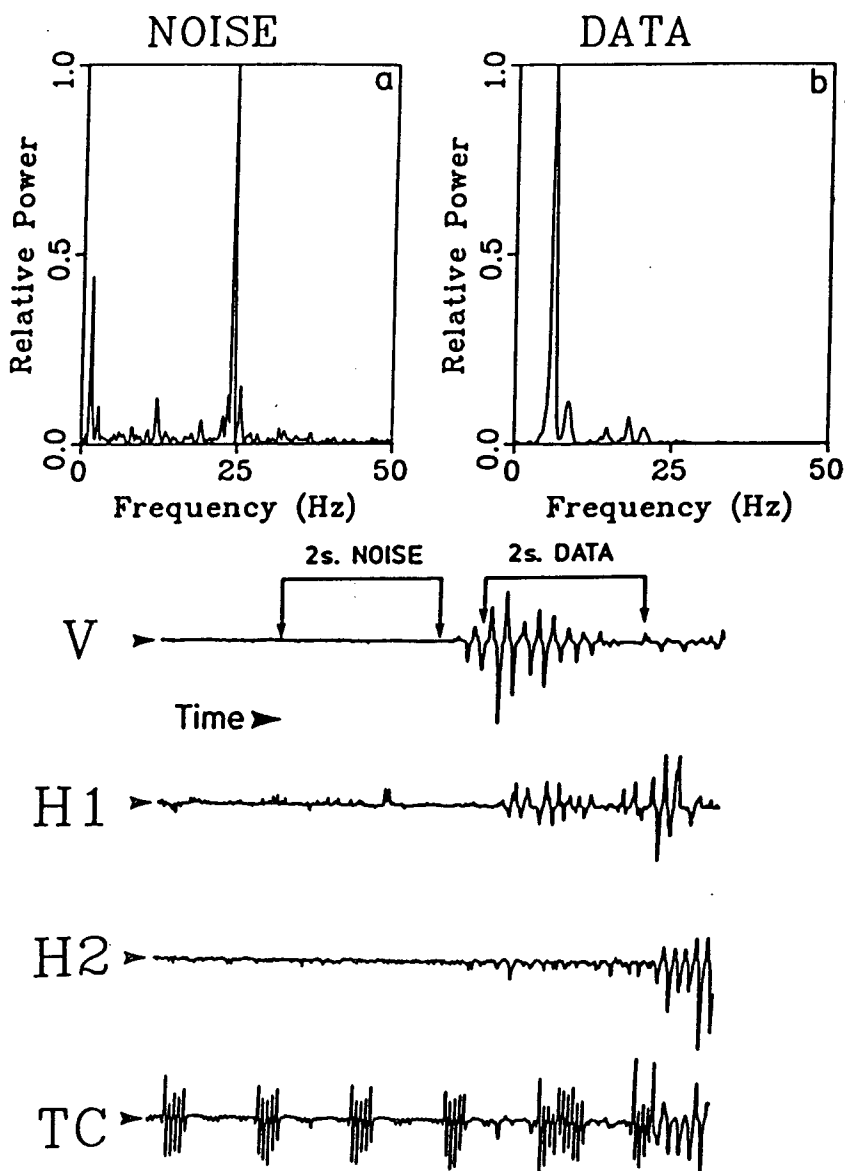


Figure 3.3 An example of raw ocean bottom seismograph data.

The four traces shown were recorded on OBS #5, at a source-receiver distance of 47 km. V - output from the vertical seismograph; H1 and H2 - output from the two horizontal seismographs; TC - 20 Hz time code.

a) Power spectrum for 2 seconds of 'noise' on the vertical channel, V, as shown. The large peak close to 25 Hz is due to cross talk from the time channel.

b) Power spectrum for 2 seconds of 'data' on channel V, as shown. The dominant frequency is 6 Hz.

the instrument but gives poor signal reproduction fidelity when squared after digitization to recover the relative amplitude information.

3.2.3 OBS Data Presentation

The six record sections constituting the seismic data set modelled in this study are shown in figures 3.4 and 3.5. The trace amplitudes on all sections are scaled with an r^2 spreading factor to enhance weak arrivals at greater distances. All the airgun data (figure 3.4) have been bandpassed with a 3 to 15 Hz eight pole, zero phase, Butterworth filter. The explosion data presented in figure 3.5 are unfiltered, but in order to compensate for the different charge sizes used, an amplitude normalization factor of $\text{weight}^{2/3}$ is applied. This expression is based on empirical results relating the size of the charge to the amplitude of seismic energy which it generates (O'Brien, 1960; Kanestrøm and Øvrebø, 1978). The validity of this normalization, as applied to the data presented here, is discussed in section 4.3.

On all sections the OBS clock drift has been removed using the assumption of linearity (section 3.3.1), and all source depths have been corrected; placing sources on the sea surface. First arrival travel time picks are indicated by arrowheads.

3.2.4 OBS #1: Airgun Data

First arrival picks can readily be made to almost 20 km offset on this section (figure 3.4). The velocity indicated along the entire length of the profile is close to 6.0 km/s, and there are no clearly defined major amplitude features. The steady build-up in energy with offset seen in the distant 10 km of the profile is merely an artifact of the r^2 spreading factor. A linear distance enhancement factor would give a more realistic appearance to the section. The large amplitude features seen in the upper left of this and the other airgun sections, are the direct water wave arrivals.

3.2.5 OBS #3: Airgun Data

First arrivals are clearly visible out to almost 10 km offset (figure 3.4). The absence of appreciable energy further out is due to the smaller airgun used (16 litre as compared to 32 litre for OBS #1), and also the relatively high attenuation expected in material below OBS #3. The less homogeneous nature of this medium is implied by the trace-to-trace fluctuations in first arrival travel times and amplitudes. The refraction arrival velocity increases from 2.0 to 3.0 km/s with offset.

3.2.6 OBS #5: Airgun Data

First arrivals are visible out to about 12 km offset. High attenuation, and the smaller airgun as mentioned above, are expected to account for the lack of energy at greater offsets. The velocities indicated are similar to those for the OBS #3 airgun section.

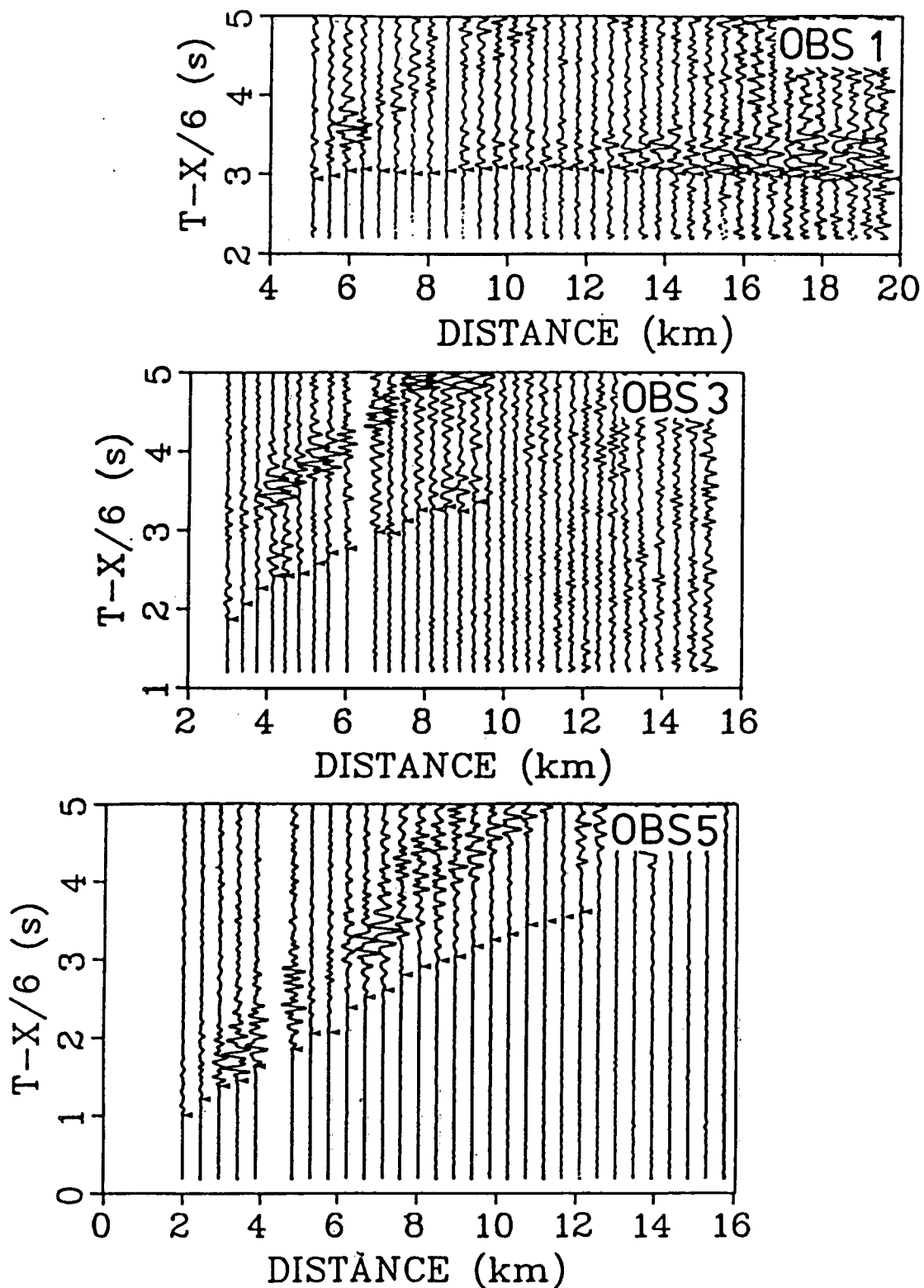


Figure 3.4 Airgun data.

Record sections for OBS #1, #3, and #5 are shown. A 32 litre gun was used for OBS #1, whilst a 16 litre source was used for OBSs #3 and #5. All the data have been bandpass filtered (3-15 Hz) and an r^2 spreading factor applied to enhance distant arrivals. First arrival travel time picks are indicated by arrowheads.

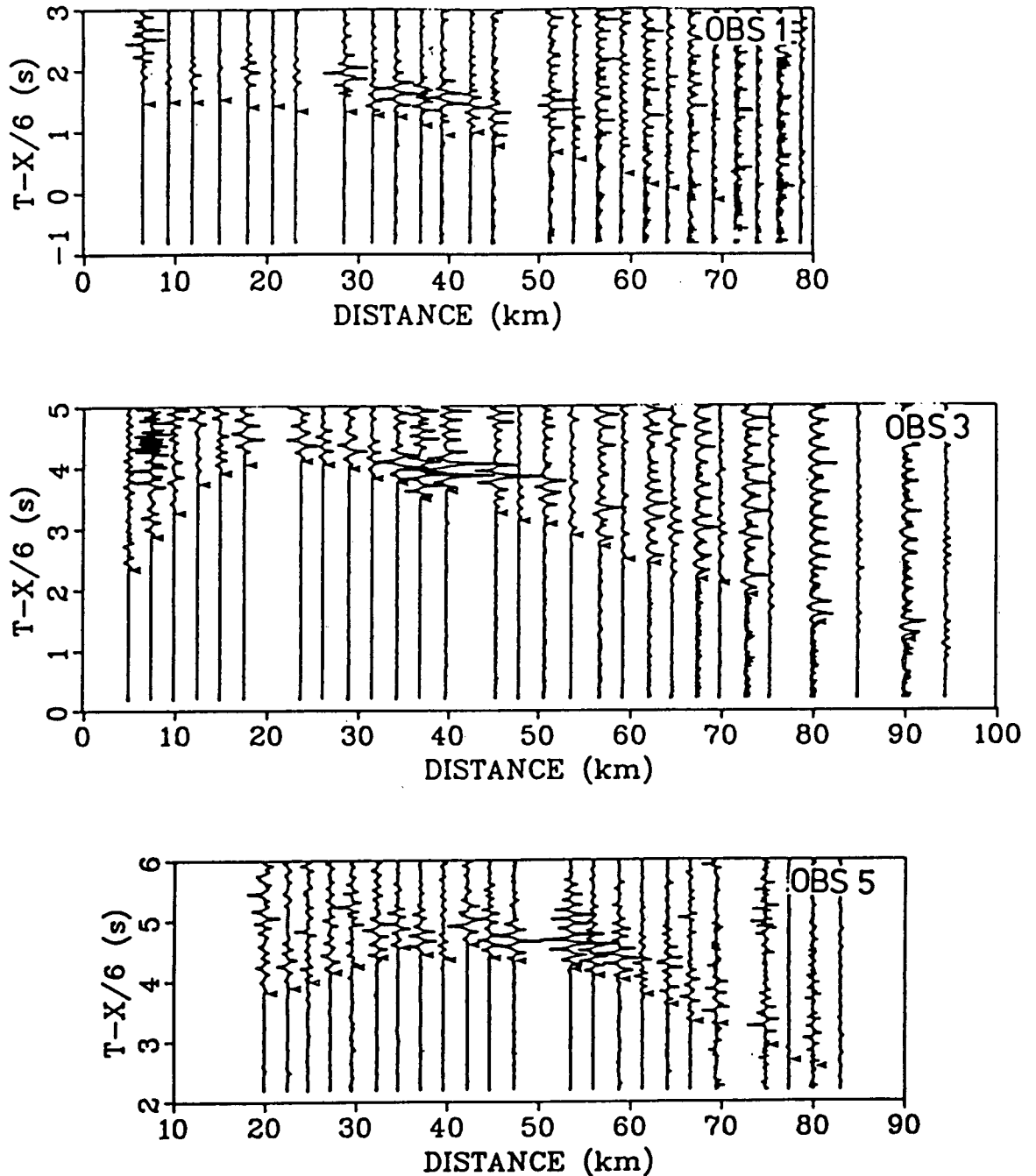


Figure 3.5 Explosion data.

Record sections for OBS #1, #3, and #5 are shown. The explosives were detonated on a 100 km line along profile I (figure 3.1). All the data have been bandpass filtered (3-15 Hz) and an r' spreading factor applied to enhance distant arrivals. An empirical charge size correction of W'' (where W is the charge weight in kg), has been used. The first arrival travel time picks are indicated by arrowheads. Misfires account for the two large trace separations on the sections. On the OBS #1 section, times are adjusted to place the shots at the 2.52 km depth of the OBS; for OBS #3 and #5, the travel time effect of the water column is retained.

3.2.7 OBS #1: Explosion Data

All shots on this section have been corrected to a datum depth of 2.52 km (the depth of OBS #1), by ray tracing through the water column (see figure 3.6). There are clear travel time picks out to about 50 km offset, past which little signal energy was received. The apparent refraction arrival velocity increases from 5.7 km/s to 8.0 km/s over the profile. There is a group of traces with increased amplitude between 12 and 18 km offset; the trace at 15 km is comparatively low in amplitude due to the over-compensation of the charge size weighting factor which was applied (section 4.3). The main amplitude group seen between 28 and 45 km may be slightly broader in extent, but is undefined at the edges due to the misfiring of charges at 26 and 48 km offset. The retardation of the main energy group at 51 km, relative to the closer arrivals, suggests the presence of some lateral heterogeneities at the crust-mantle boundary. The oscillatory trace-to-trace variation in apparent noise level is at least partly an artifact of the charge size correction. There is a small d.c. bias on all traces, which becomes increasingly more apparent at large offsets, due to the effect of the r^2 enhancement factor.

3.2.8 OBS #3: Explosion Data

There is clear signal energy seen out to 95 km on the section. Reasonably accurate picks (error < 0.6 s) can be made out to 60 km offset. The apparent refraction arrival velocity increases from 2.8 km/s to 8.2 km/s over the profile. The only

well defined large amplitude group lies between 33 and 46 km. The oscillatory noise level and d.c. bias mentioned above are clearly visible on this section also.

3.2.9 OBS #5: Explosion Data

First arrival energy can be seen out to 80 km on this profile. Accurate picks (error < 0.06 s) have been made out to 67 km offset, with less accurate picks beyond this distance. The apparent refraction velocity increases from 4.5 km/s to 10 km/s over the profile. There are amplitude variations over the nearer part of the section, but no clearly defined groups. The main amplitude group between 47 and 58 km lacks clear definition due to misfire of the shot at 50 km offset.

3.3 Inherent Data Errors

3.3.1 Travel Time Errors

There are four sources of travel time errors.

- 1) Origin time calculation
- 2) Digital sampling rate fluctuations
- 3) OBS internal clock drift
- 4) Picking Error

The estimated magnitude of these errors is summarized in table 3.1.

Cause	Maximum estimated error
origin time calculation	± 0.03 s
Digital sampling rate fluctuations	< 0.003 s
OBS internal clock drift	< 0.001 s
picking error	0 (0.1) s

Table 3.1 Inherent travel time errors.

1) The shot origin time may be estimated from the shot depth d the distance from ship to shot x and the water velocity V_w . The distance x must in turn, be estimated from the ditch time t_s and the average ship speed over that time interval V_s . The origin time, t_o , is then given by:

$$t_o = t_1 - \frac{\sqrt{d^2 + x^2}}{V_w}$$

where t_1 = the arrival time of the direct water wave (recorded on a hydrophone towed immediately behind the ship).

The shot depth may be estimated in 2 ways: the reflection method or the bubble pulse method (see Horn (1982) for discussion). The maximum probable error is generally ± 30 m. This value, in addition to errors in t_s , V_w , V_s , and t_1 , gives a maximum estimated error in the order of ± 0.03 s.

2) Sample rate fluctuations in the digitization process (see Appendix B) lead to timing errors of less than 0.003 s.

3) The internal OBS clocks do not maintain their accuracy during the period of deployment; there is clock drift relative to the WWVB standard time signal. Comparisons between OBS clock times and WWVB time were made immediately prior to instrument release and after recovery. A linear regression through the differences between the two times provides a drift curve for each OBS clock, which was then used to calculate drift corrections for each shot. The instrument drift rates are given in Table 3.2.

Instrument	Down Time	Total Drift	Drift/Hour
OBS #1	10 days	+2.461 s	+0.00958 s
OBS #3	11 days	-0.779 s	-0.00275 s
OBS #5	12 days	-2.538 s	-0.00857 s

Table 3.2 Instrument deployment times.

4) The picking error varies with signal/noise ratio, but is generally between 0.5 and 0.1 s.

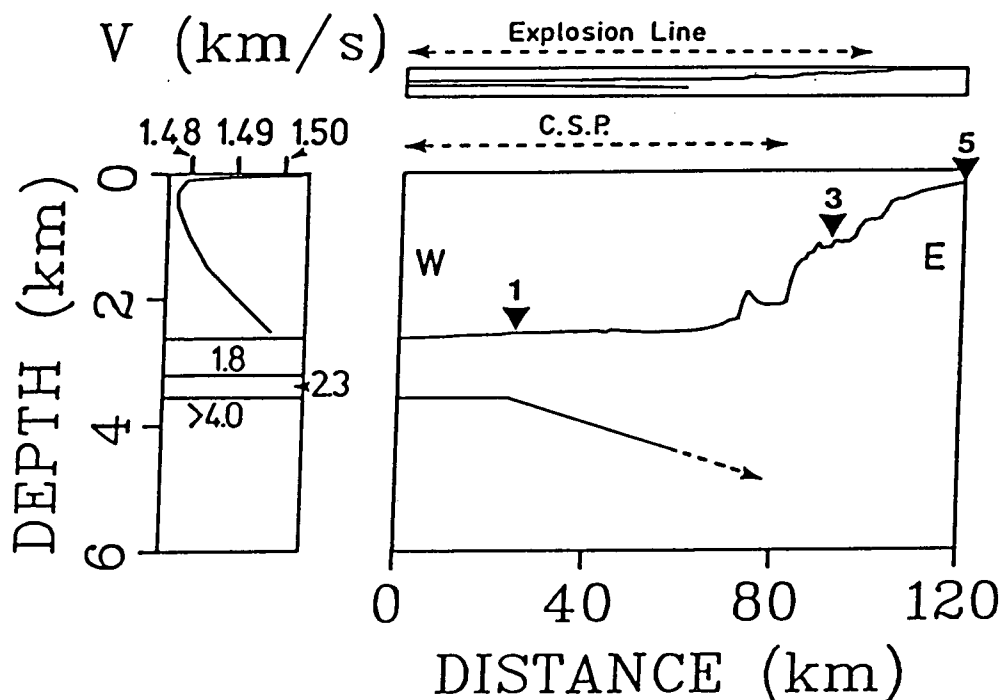


Figure 3.6 Seafloor and basement topography.

Lower right: The seafloor topography, obtained from echo-soundings, and the basement topography, interpreted from the CSP record (figure 3.2). Vertical exaggeration is 14:1. Positions of the three OBSs are indicated by inverted triangles.

Note that there is no clear indication of the basement topography east of the continental rise.

Upper right: The lateral extent of the CSP and explosion profiles, together with a 1:1 representation of the topography variation.

Left: A standard sound velocity profile for the water column, together with the chosen velocities for the sub-surface material.

3.3.2 Distance Errors

All shot locations and OBS positions are determined from Loran C Navigation, supplemented by regular satellite fixes. Relative accuracy of these positions is about 200 m with an

absolute accuracy of 300 m. Shot-receiver distances determined in this fashion have higher accuracy than those calculated using direct water wave travel times (Au, 1981).

3.4 Topography Corrections

In many marine refraction studies (e.g. Horn, 1982; and Au, 1981), attempts are made to remove the effects of sediment and basement relief in order to simulate one-dimensional structure. Two different approaches are commonly chosen to accomplish these corrections (see discussion in Au, 1981).

The degree of seafloor relief along the profile considered in this study is variable (see figure 3.6): high on the continental slope to the east but subdued on the abyssal plain. The form of the sediment-basement interface is determined from CSP records (see figure 3.2) for the westernmost 50 km of the profile. No profiling was conducted east of the continental rise in the VISP-80 project but other CSP records in the area (Barr, 1974) do not delineate the interface east of the rise.

Due to the lateral variation in magnitude of the relief, different approaches to corrections for the topography were used for the individual data sets.

The airgun profile recorded on OBS #1 (figure 3.4) was conducted over relatively subdued sediment and basement relief which was accurately determined from 3.5 kHz depth sounding and CSP data. All shots were corrected to an equivalent source depth of 2.52 km (the depth of the OBS) by ray tracing through the water column. The sound velocity profile of the water

column (figure 3.6) is based upon a compilation of the National Oceanographic Data Center in Washington, D.C.. The OBS depth was chosen as an upper sediment datum and an averaged basement depth as the lower datum. Corrections for the variation in depth of the water-sediment and sediment-basement interfaces were then obtained by appropriately replacing one type of material with another above or below the reference datum. The magnitude of the resulting time and distance corrections is relatively insensitive to the chosen ray parameter but extremely sensitive to sediment and basement velocities used (Detrick and Purdy, 1980). This approach was used in the present study as the sediment velocities are constrained by additional information (see Appendices C and D).

The near 50 km of the explosion profile recorded on OBS #1 passed over almost flat seafloor and an eastwardly dipping sediment-basement interface (see figure 3.2). For the purposes of one-dimensional velocity inversion (see section 2.2), the shots were corrected to the sloping basement, effectively removing the sedimentary wedge. In subsequent two-dimensional modelling (section 4.2.2) the sediments were recombined, as interpreted from the CSP, and shots placed on a datum with the OBS (as for the airgun data above).

The airgun data recorded on OBS #3 and #5 (see figure 3.4) were corrected to datum levels at the instrument depths. No basement corrections were made as the data did not sample this deep, and consequently no information on the form of the interface was obtained.

The explosion profiles recorded on OBSs #3 and #5 were shot largely in deep water, whilst the instruments recorded at shallow depths on the continental rise. The data were modelled with the water column present since correcting to datum levels at the OBS depths would involve replacing up to 2 km of water with sediment of uncertain velocity. The structure under OBSs #3 and #5 was known to be laterally variant, indicating a need for two-dimensional modelling techniques; thus the inclusion of seafloor topography in the modelling provided no additional complications for interpretation.

3.5 Comments on Data Trends

3.5.1 Airgun Sections

For OBS #1 on the deep ocean floor, the velocities indicate a relatively shallow, high velocity medium (consistent with the basement depth indicated by the CSP record), whilst the clear arrivals suggest a comparatively homogeneous structure. OBSs #3 and #5, on the continental rise and slope respectively, indicate velocities characteristic of compacted, compressed sediments. The slightly erratic, lower energy arrivals suggest some degree of lateral heterogeneity resulting in increased attenuation of the seismic energy.

3.5.2 Explosion Sections

The main amplitude group moves out to greater offset from OBS #1 to #5 (see figures 3.5 and 3.7), implying that the lower crustal structure from which the energy returns is deeper to the east.

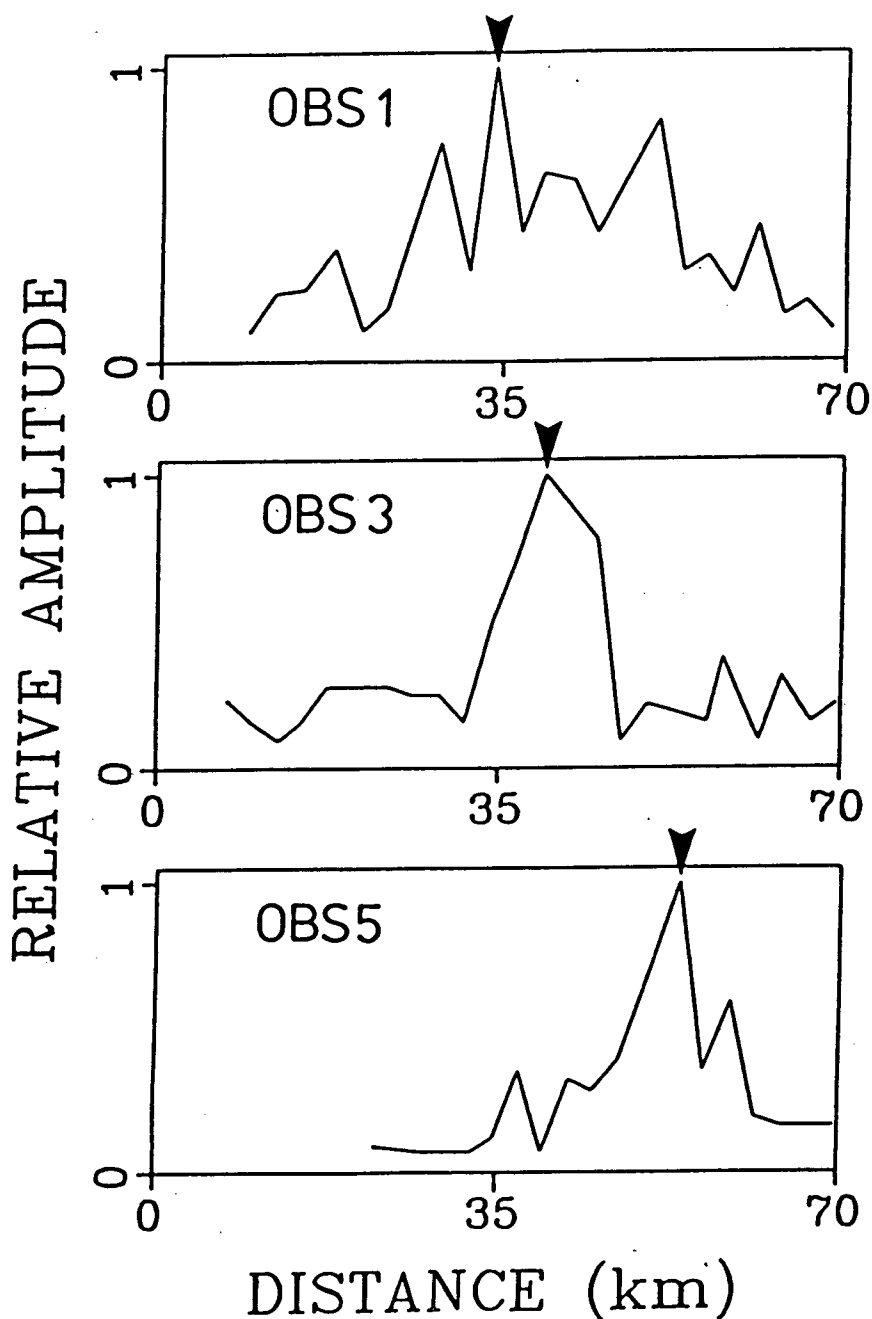


Figure 3.7 Relative amplitude variations for OBS #1, 3 and 5.

The values shown are the maximum trace amplitudes observed on the record sections (figure 3.5) during the second following the first arrival travel time. The oscillatory nature of the distributions is due to the inaccurate charge size correction. Note the movement of the main amplitude peak, indicated by the arrowhead, to greater offset from OBS #1 eastwards to OBS #5.

The apparent velocity at large offset on all sections lies between 8 km/s and 10 km/s; increasing from OBS #1 eastwards to OBS #5. This suggests an increase in dip of the Moho, or else a significant lateral increase in mantle velocity eastwards. The latter possibility is very unlikely.

"that small model of the barren earth,
Which serves as paste and cover to our bones¹."

CHAPTER 4 DATA INTERPRETATION a detailed description

4.1 Summary of the Approach Taken

To adequately model the complex seismic structure of the continental margin requires application of ray tracing procedures and synthetic seismogram techniques for inhomogeneous media. For the purpose of one-dimensional velocity inversion, shots recorded on OBS #1 were corrected to the sloping basement, effectively removing a wedge of sediment. The adjusted first arrival travel time-distance data were then transformed into the τ - p domain and a linear programming technique (section 2.2; Garmany et al., 1979) applied to find a one-dimensional model which had the maximum velocity at the shallowest depth. Two-dimensional models satisfying the uncorrected travel times were then determined from the initial structures by trial-and-error application of the ray tracing technique of Whittall and Clowes (1979). To incorporate the dynamic information, the WKBJ synthetic seismogram algorithm of Chapman (1978) was then used to refine the assumed one-dimensional velocity structure in the descending oceanic crust by subjective comparison of computed and observed records. Combination of the dipping slab model with overlying sediments then gave a two-dimensional model

¹Shakespeare: Richard II.

which was tested for consistency with the observed data using an asymptotic ray theory (ART) synthetic seismogram algorithm for laterally varying media (McMechan and Mooney, 1980). Eastward extrapolation of the OBS #1 model provided starting models for interpretation of the OBS #3 and #5 explosion data.

The final model thus obtained for all the data sets was then mutually consistent and compatible with all of the information.

4.2 Travel Time Modelling

4.2.1 Airgun data recorded on OBS #1

The raw data were corrected to a source depth equivalent to that of the instrument and topography was removed as described in section 3.4. One-dimensional travel time inversion by linear programming gave a preliminary velocity model which was subsequently modified by ray-tracing. The structure is defined to almost 4 km by these data (to the bottom of region B, inset of figure 4.1) and is very similar to that found by Au and Clowes (1982) approximately 100 km to the northwest on the Juan de Fuca plate.

4.2.2 Explosion data recorded on OBS #1

The near 50 km of the profile was corrected to place all shots and the instrument on the sloping basement (section 3.4). The resulting one-dimensional sub-sedimentary structure, deduced from travel time inversion, was then recombined with the sedimentary wedge to yield a laterally varying starting model for ray tracing. A model derived by this method is shown

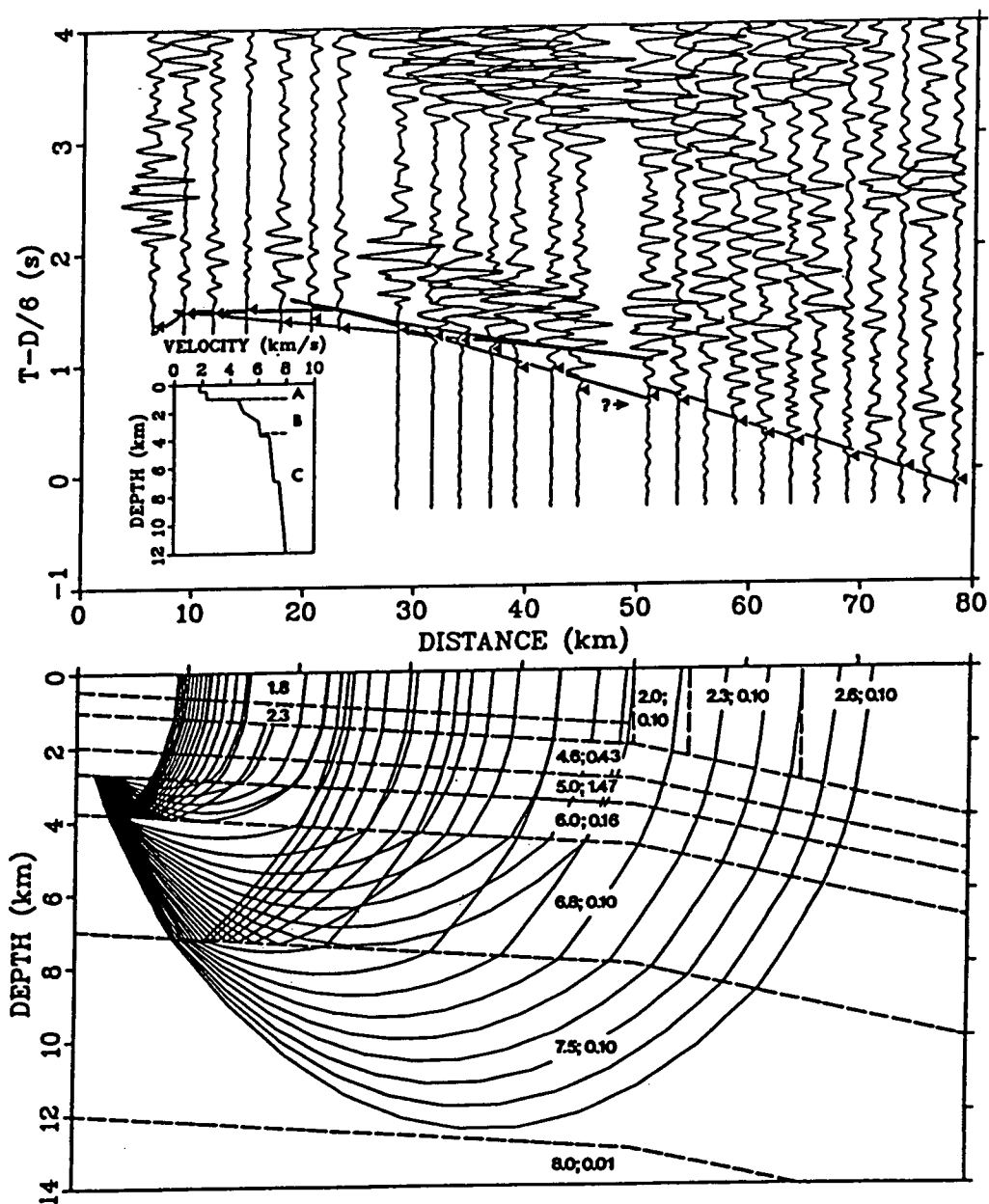


Figure 4.1 A preliminary travel time model for OBS #1

Upper: Filtered (3-15 Hz) record section for OBS #1 explosion data. Times are adjusted to place the shot at the 2.52 km; depth of the OBS, and the amplitudes adjusted with an r^2 factor. The large amplitude secondary arrivals which replicate the features of the first arrivals are probably a shear phase converted from P-waves at the sediment-basement interface below the OBS. Arrows are first arrival picks; solid line links travel times calculated through a preliminary velocity-depth model beneath OBS #1, shown in the inset. The boundaries of A are from the CSP data (figure 3.2) with the velocities assumed; the structure of B from interpretation of the airgun profile (figure 3.4); and the structure of C from the explosion data.

Lower: A preliminary two-dimensional velocity model, from the OBS #1 travel time data, showing ray paths for explosion arrivals. Velocities (km/s) are given for the top of each layer followed, after the semi-colon, by the velocity gradient (km/s/km).

in figure 4.1. The 1.4° eastward dip of the sub-sedimentary layers over the first 50 km was deduced from the CSP record (figure 3.3). Boundaries below the sediment-basement interface are chosen to dip at the angle of this contact. The margin of the continental rise is approximated by a vertical boundary (50 km east of OBS 1) and the expected lateral change in sediment velocity has been modelled by three additional artificial vertical boundaries. With these velocities, simultaneous modelling of the data and the extended onshore-offshore profile requires that dip of the sub-sediment layers increase to $4^\circ \pm 1^\circ$ at the start of the rise. In this preliminary two-dimensional travel time model, the first arrival energy beyond 50 km was modelled as being due to turning rays in the lower crust. A velocity gradient of 0.1 km/s/km is required to produce these rays and mantle velocities (~ 8.0 km/s) are reached near 12 km, a depth similar to that found along a seismic profile on the northern Juan de Fuca plate by Au and Clowes (1982). When rays were traced through this model into OBS #3 the travel time fit was reasonable, but subsequent refinement, based on the continental slope sediment velocity information provided by the OBS #3 airgun data, and the Shell Anglo Cygnet well log (Appendix D), improved the agreement.

4.2.3 Airgun data recorded on OBS #3

These data were corrected to a source depth of 1.12 km (position of OBS) and the seafloor topography corrected (section 3.4). The linear programming inversion procedure gave

a velocity of 2.0 km/s in the top 1.2 km of sediment, underlain by a gradient region beginning at 2.6 km/s and increasing at 0.3 km/s/km. The data define structure down to almost 2 km.

4.2.4 Explosion data recorded on OBS #3

These data have a higher degree of associated non-uniqueness than the corresponding explosion line recorded on OBS #1. With OBS #1 the dip of the basement for nearer shots is known independently (from CSP records) and sediment velocities may be better estimated from other refraction studies in the area and from the Chevron Standard multichannel data (Appendix C). The basement dip under OBS #3 is unknown, although presumably $>1.4^\circ$, whilst only shallow sedimentary information is available over a limited distance range. In fitting the travel times there is thus a trade-off between the magnitude of an eastward sediment velocity increase and the dip of the basement. The closer shots do give additional sediment velocity information, sampling deeper than the airgun, but the sparse shot spacing and expected structural complexity of the continental rise do not lead to well constrained solutions.

The a priori modelling assumption used for the OBS #1 data set (i.e. that all boundaries below the sediment-basement interface are taken to dip at the angle of that contact) was introduced to artificially constrain the two-dimensional solution, with its high degree of non-uniqueness. As noted above, the solution for the OBS #3 data set is even less well

constrained; indicating the need to retain this assumption. The closer 50 km of the OBS #1 explosion data are the most diagnostic for the sub-sedimentary structure and thus amplitude modelling of these data was conducted to give velocities and depths for the crust under the deep ocean (section 4.3) before full interpretation of the OBS #3 data

4.2.5 Airgun data recorded on OBS #5

These data were corrected to a source depth of 0.16 km (position of the OBS) and seafloor topography corrections (section 3.4) were applied. The linear programming inversion procedure gave a velocity of 1.6 km/s near the sea floor, with the velocity rapidly increasing to 2.0 km/s at ~ 0.5 km, then increasing at 0.5 km/s/km.

The data define structure down to about 2 km depth. The velocity variation is consistent with that derived from interval transit times obtained in the Shell Anglo Cygnet well (Appendix D), which was situated ~ 18 km from the OBS #5 site.

4.2.6 Explosion Data Recorded on OBS #5

The easternmost shot of the explosion line was denoted over the continental rise, ~ 20 km east of the OBS position. The data are unreversed, but constraint is provided by the passage of rays beyond 30 km offset through material sampled by OBS #1 and #3. Linear programming techniques were not applied to the data, due to the expected high degree of lateral heterogeneity. Initially a two-dimensional model was constructed which incorporated the structure derived for

OBS #1 and #3 and continued the dipping layers of the crust beneath the continental rise. This was then used as a starting model for trial-and-error forward modelling using the ray-tracing technique.

Various layer dips and upper sediment structures were tried in an attempt to achieve consistency with the observed travel time data. It rapidly became apparent that the assumption of discrete upper crustal layers dipping beneath OBS #5 was incompatible with observations. In order to satisfy the trend of the first six arrivals (20-32 km on OBS #5 explosion section, figure 3.5), a velocity of ~ 4.5 km/s was required at 4 km depth. Interpretation of a multichannel line (almost co-linear with the line considered here, see appendix H). suggested the presence of a *mélange* at about this depth (Snively and Wagner, 1981). The upper crustal layers were replaced with a block of material with velocity ~ 4.6 km/s at 4 km, increasing at 0.2 km/s/km. The structure of the lower crust remained as before.

4.3 Amplitude Interpretation of OBS #1 Explosion Data

General comments regarding amplitude interpretation are given in section 2.4.2 and a discussion of the computation of synthetic seismograms in Appendix A.

For trial-and-error amplitude modelling of this data set, the WKBJ synthetic seismogram algorithm (Chapman, 1978) was used. In order to approximate one-dimensional structure, the data were again corrected to the dipping basement, removing a wedge of sedimentary material. The effect of this material on

observed amplitudes was expected to be negligible, due to the near vertical nature of rays passing through the sediment. This expectation was confirmed by the close agreement found in derived relative amplitudes (for a given model) between a WKBJ synthetic seismogram through the sub-sedimentary structure and an asymptotic ray theory two-dimensional synthetic seismogram, for which the model incorporated the sedimentary wedge.

Only modelling of the general amplitude features is justified due to the lack of spatially dense data, and the probability of significant lateral heterogeneities in addition to the dipping sub-sedimentary layers.

The relative amplitude of the first 1s of first arrival energy on the traces recorded on OBS #1 is shown as a function of distance in figure 4.2. Three main features were modelled; the primary large amplitude group (B; 30-40km), the secondary amplitude group (A; 12-20 km), and the decay region (C; >45 km). It is clear from the figure that the trace-to-trace amplitude variation is erratic. This is due in part to suspected lateral heterogeneities and focussing effects and to the inaccurate correction for varying charge size. The corrected and uncorrected relative amplitudes are compared in figure 4.2. Ideally the effect of a precise charge size adjustment factor on the amplitudes should be to smooth the trace-to-trace variation. No such smoothing is noticeable (in some cases the traces become more erratic), a feature which has led to concern about the validity of the charge size correction. It is certainly a more reliable procedure to model relative amplitudes from identical charge sizes, although this

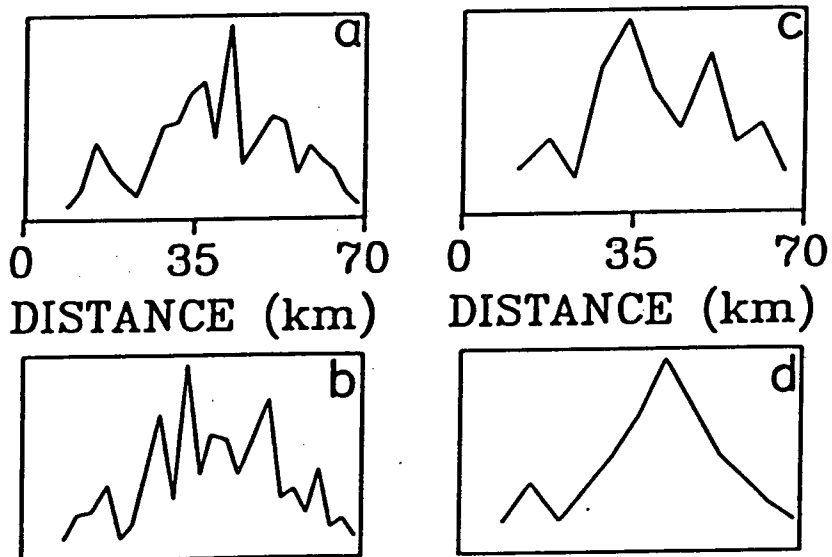
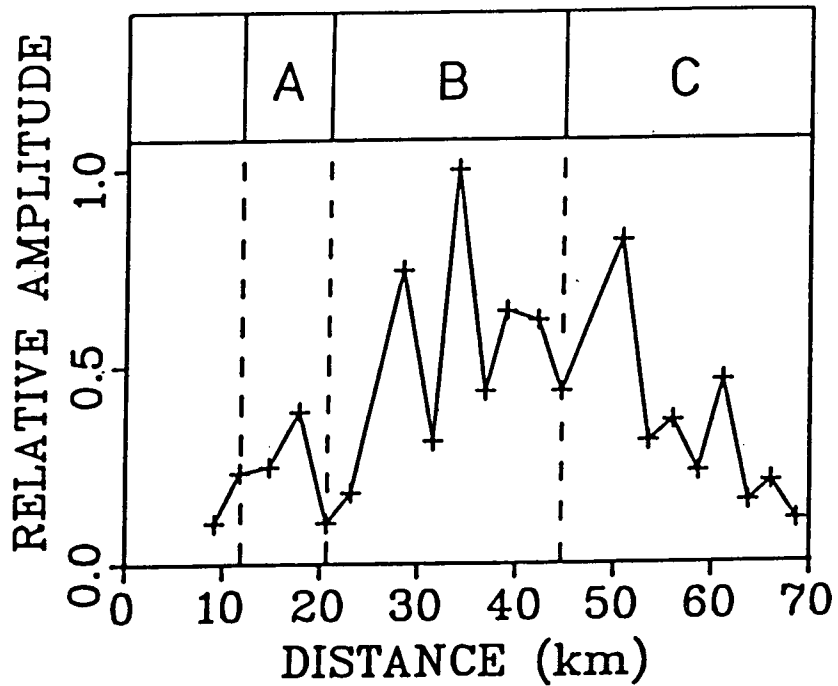


Figure 4.2 Amplitude characteristics of OBS #1 explosion data.

Upper: Relative amplitude variation vs. distance for OBS #1. The values shown are the maximum trace amplitudes observed on the record section (figure 3.5) during a 1s interval following the first arrival travel time. Each cross corresponds to one trace.

The data show three main features, which were considered significant for modelling:

- A) Secondary large amplitude group
- B) Primary large amplitude group
- C) Decay of amplitude past 45 km.

Lower: Diagrams to illustrate the effect of charge size variation, and its correction, on the relative amplitude vs. distance distribution for OBS #1.

- a) Uncorrected for charge size variation
- b) Corrected for charge size variation
- c) Only 50 kg charges considered
- d) Only 200 kg charges considered.

method halves the effective spatial data density for the VISP-80 data set.

As noted in section 2.5, "the aim in all seismic modelling should be to produce the velocity-depth model which has the least structure still compatible with all the data." The preliminary velocity variation beneath OBS #1 (inset figure 4.1), derived from travel time modelling of OBS #1 data has three distinct structural characteristics:

- i) a velocity discontinuity at 3.75 km
- ii) a velocity discontinuity at 7.00 km
- iii) a gradient region in the lower crust with Moho velocities (8.0 km/s) at 12 km.

4.3.1 Boundary at 3.75 km

The position of some form of velocity increase is constrained to be centered at 3.75 ± 0.5 km by the travel time data, with the given errors. Calculated travel times through the model are sensitive to the form of the velocity variation (see synthetic examples; figure 2.2). The presence of a region of rapid velocity increase at 3.75 km is clearly indicated by the near high amplitude group (12-20 km offset). Following the modelling policy of producing a smoothest velocity variation consistent with the data, the boundary was changed to a 1 km thick velocity transition zone (gradient = 0.8 km/s/km). Further smoothing of the variation removed the observed amplitude decrease around 24 km, and was thus rejected.

4.3.2 Boundary at 7.0 km

The presence of this boundary, or a region of rapid velocity increase, has the effect of splitting the main amplitude group into two sub-groups. This could be consistent with the observed data, but as noted above, the crude spatial sampling together with uncertainty regarding the validity of the charge size correction means that only a general fit to the main amplitude group can be made. This feature was removed entirely from the model and replaced with a smooth increase from just below the velocity increase around 3.75 km to the Moho.

4.3.3 Lower crust and Moho structure

The decay of amplitude beyond 45 km offset is a clear feature of the data, although there is an anomalously high amplitude for a shot at 50 km. On the record section (figure 3.5, upper) this energy packet is shifted later in time relative to the corresponding feature for closer shots. The energy is due, at least in part, to some secondary arrival and may be a local focussing effect from the Moho region: a denser sampling in X would be needed to resolve this point. This high amplitude energy packet cannot be satisfactorily modelled by using the methods and approximations employed here as it is only defined by one point on the relative amplitude-distance plot.

A large range of Moho models has been found to be consistent with the observed travel time and amplitude data. The only requirement for synthetic seismogram modelling is

that models produce a decay in amplitude after 50 km offset. The initial model derived from travel time inversion (inset, figure 4.1) does not satisfy this condition; high amplitudes are produced out to 75 km offset; indicating a Moho significantly shallower than 12 km.

The different possible types of velocity transition at the Moho, and their effects on observed amplitudes are discussed in Appendix E. In the OBS #1 explosion data, no clearly identifiable sub-critical reflection energy is observed on the record section (figure 3.5). Thus, the observations favour choice of a smooth, gradational, change in velocity at the Moho, although the possibility of a small step-function velocity boundary is not inconsistent with the data as the resolution of these features is low (due to the long source wavelet and low spatial sampling density).

The effect of Moho depth, represented by a change in velocity gradient, on relative amplitude-distance distributions is summarized in figure 4.3. The position of the main amplitude peak is quite sensitive to Moho depth, moving further out as the boundary becomes deeper. By comparison with the real data, the preferred depth for the gradient change is 9.3 km, although as noted above, the position of the peak in amplitude is ambiguous due to the different charge sizes used. With this preferred model the gradient changes from 0.2 km/s/km to 0.01 km/s/km at a velocity of 8.0 km/s. The value for mantle gradient is that used in the modelling of the onshore-offshore profile by Spence (personal communication, 1982). Combination of this velocity structure in the dipping

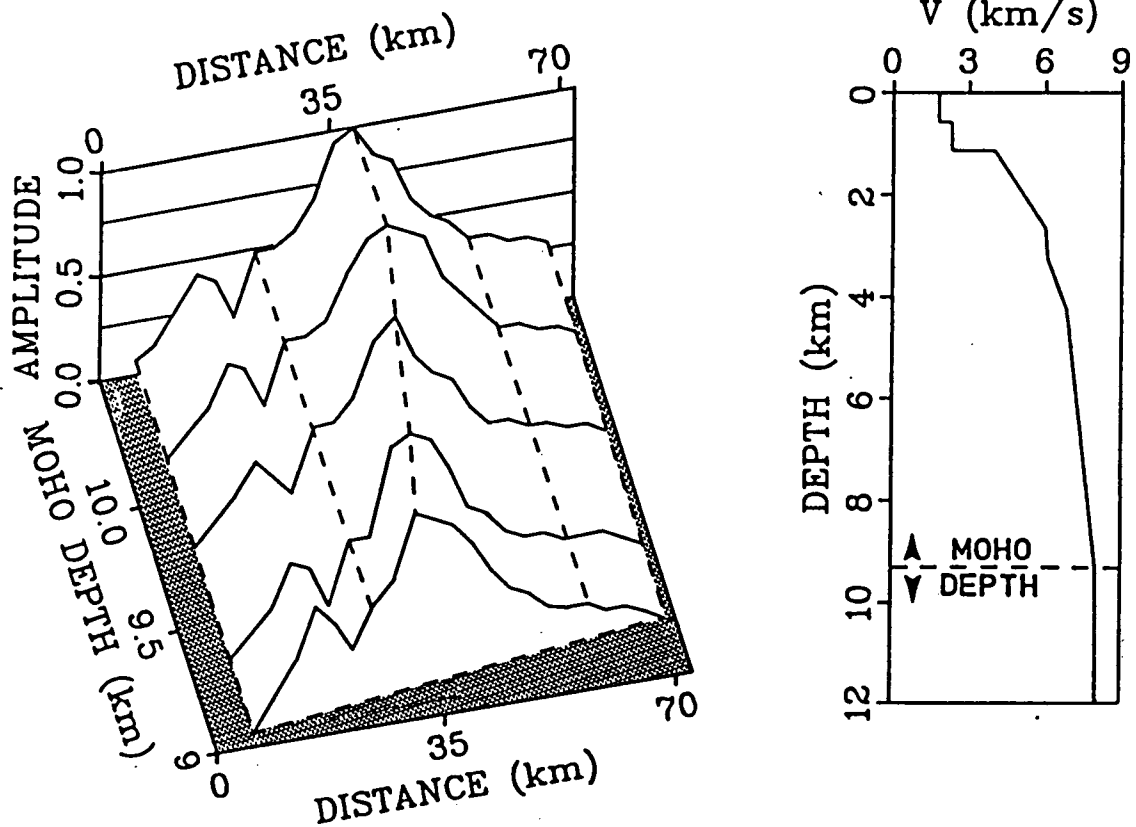


Figure 4.3 The effect of Moho depth on amplitude distributions.

Left: A three-dimensional plot of the Moho depth used in a model against the relative amplitude-distance distributions produced by the WKB synthetic seismogram algorithm used with that model. Note the movement of the main amplitude group to greater offset with increasing Moho depth.
 Right: Preferred velocity-depth structure under OBS #1. Moho-depth is defined as the change in velocity gradient at 8.0 km/s. -

plate with the sedimentary structure produces good agreement with observed data (figure 4.7, and 4.8). The arrivals beyond 40 km are modelled as head waves, produced in the model by a minute velocity discontinuity at the Moho. The weak arrivals seen on the section (figure 3.5) beyond 50 km offset may be true head waves, interference head waves, or turning rays from

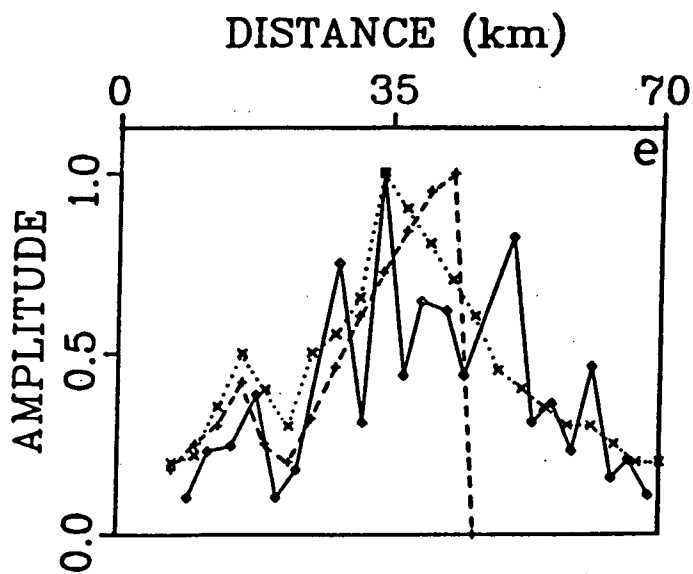
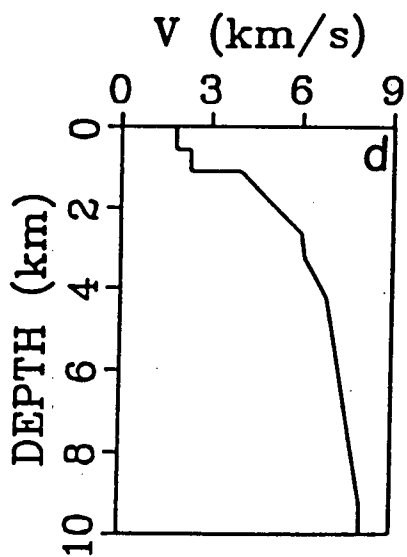
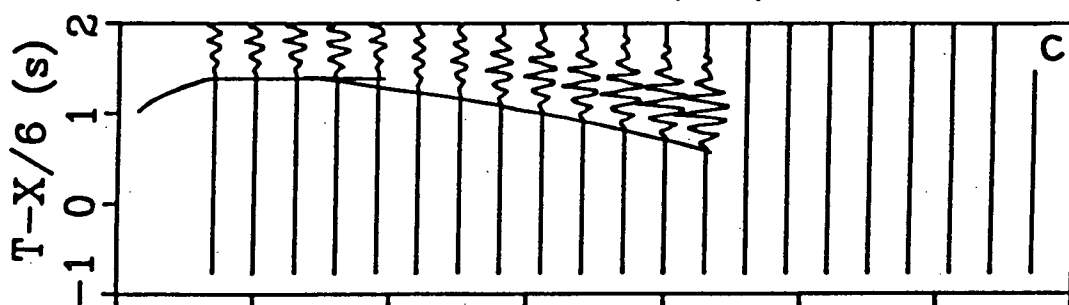
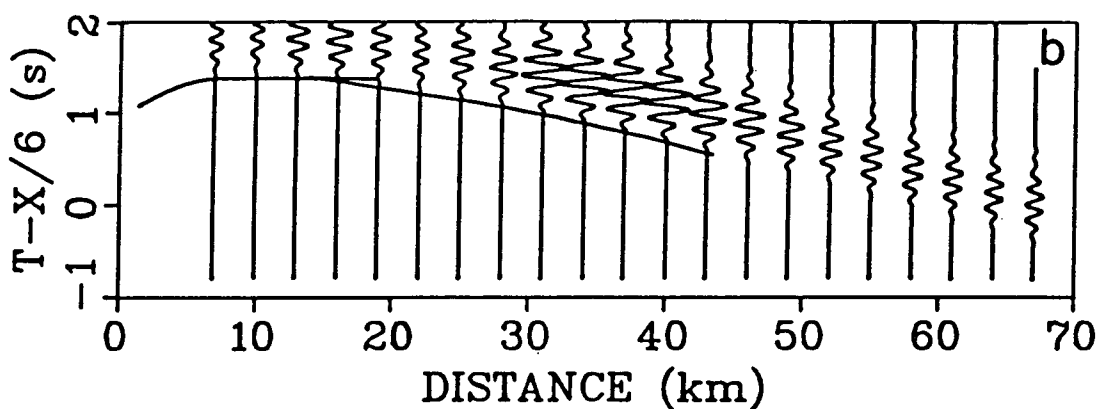
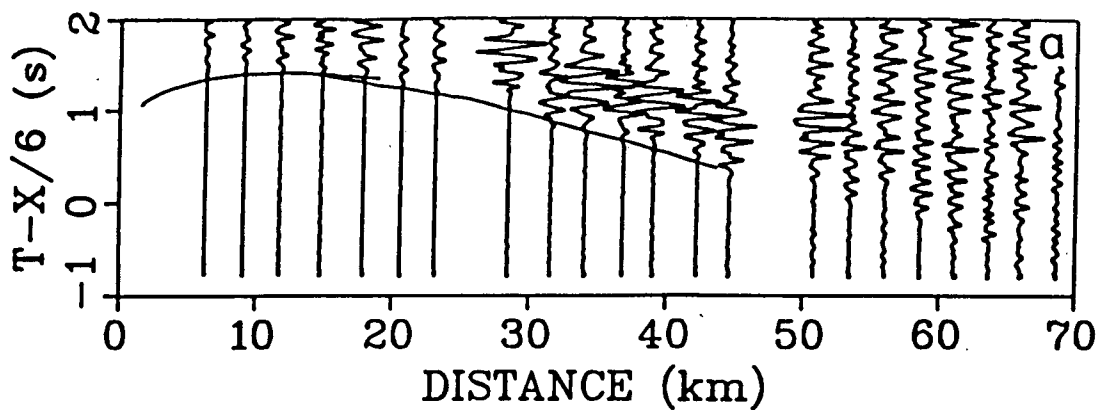
the mantle. With the low mantle velocity gradient assumed here, the arrival time difference between these different types of rays is negligible. These arrivals do constrain the dip of the Moho under the continental rise to $3^{\circ} \pm 1^{\circ}$, assuming no lateral change in upper mantle velocity.

4.4 Practical Use of WKBJ and ART Algorithms

As noted above (section 4.3), the effect of a sedimentary wedge on the amplitude of first arrivals is negligible, but a comparison of ART and WKBJ synthetic seismograms through the same model does not show absolute agreement. This is illustrated in figure 4.4. The OBS #1 explosion data, corrected to a sloping basement, are compared to the WKBJ and ART synthetic seismograms, calculated through the preferred velocity-depth structure below OBS #1. Relative trace

Overleaf: Figure 4.4 A comparison of the WKBJ and ART synthetic seismogram algorithms.

- a) OBS #1 explosion data with the travel time effect of water column and thickening of sediments eastwards removed. Solid line links the first arrival travel times from the model.
- b) WKBJ synthetic seismogram calculated through the preferred velocity-depth model for OBS #1 (d). The source wavelet used was taken from a clear arrival energy packet in the real data (see figure 2.3), and is of approximately one second duration.
Note the presence of diffractions beyond 45 km offset.
- c) ART synthetic seismograms, calculated through the preferred model (d), using the same source wavelet as in (b).
Note the absence of diffractions past 45 km offset.
- d) Preferred velocity-depth model for OBS #1.
- e) Relative amplitude distributions corresponding to the seismograms in a, b, and c.
Solid line links the trace amplitudes for the real data, which have been corrected for charge size variation. Values shown are the maximum trace amplitudes observed on the seismogram during the second following the first arrival travel time.
Dotted line links the trace amplitudes for WKBJ seismograms, whilst the dashed line corresponds to the variation for the ART seismograms.
Note that the main amplitude peak for the ART variation is shifted 7 km relative to that for WKBJ and the real data.



amplitudes for the three sections are compared at the bottom of the figure. The highest amplitude for the WKBJ solution occurs at 34 km, corresponding to that observed for the charge-size-corrected real data. Amplitude then decays smoothly with increasing offset. The ART solution produces a smooth build-up in amplitude, corresponding to rays turning in the velocity gradient of the lower crust. The maximum amplitude then corresponds to the Moho grazing ray. At greater offsets no energy is received. Head waves are not included in the ART approach and the mantle gradient is too low to give turning rays with the ray density used to generate arrivals in the crustal material. As can be clearly seen from figure 4.4, not only is there a difference in the amplitude behaviour for WKBJ and ART beyond the main peak, but also in the position of that peak. The peak in the ART solution is 7 km further out than that for the WKBJ, as calculated through the preferred one-dimensional model. This lack of agreement between the two methods reflects the different mathematical approaches used. The WKBJ method is a wave-field approach and includes the effects of geometrical diffraction. This leads to the smooth decay of amplitude, seen in a region where classical ray theory would predict no energy, and to the shifting of the main amplitude peak closer in- due to destructive interference in the region of the change in velocity gradient (at the Moho).

The zero-order ART method is based, by definition, on ray theory; no diffraction or interference effects are considered, leading to the observed differences from the WKBJ solution.

In two-dimensional modelling of the three OBS data sets considered here, relative changes in amplitude characteristics have been matched by corresponding changes in the synthetic seismograms computed using ART. Thus the size of the shift in main amplitude peak from instrument to instrument (figure 3.7) has been modelled, but the peak occurs at larger offset on the synthetic section as compared to the real data. This consistent discrepancy is due to the inherent inaccuracies of the zero-order ART method, discussed above.

4.5 Amplitude Characteristics for all Receivers

A comparison of the relative amplitude information obtained from all three instruments is shown in figure 4.5. The first column shows the variation when all 35 charges are considered. The distributions are very spiky, due to application of an empirical charge-size correction (section 4.3). The second column gives the distributions for 18 50 kg charges; here the shift of main amplitude peak to greater offset, with more easterly placement of the instrument, is clearly seen. The third column represents 13 200 kg charges; the trend is less clear when fewer shots are being considered.

As noted above (section 3.5.2), the shift in main amplitude peak with OBS position is due to the eastwardly deepening crustal structure. The Moho dip is determined from the shift in relative amplitude peak from instrument to instrument. There is considerable ambiguity associated with position of the peak due to the spatially discrete data and inaccurate charge size correction. The peak for OBS #1 occurs

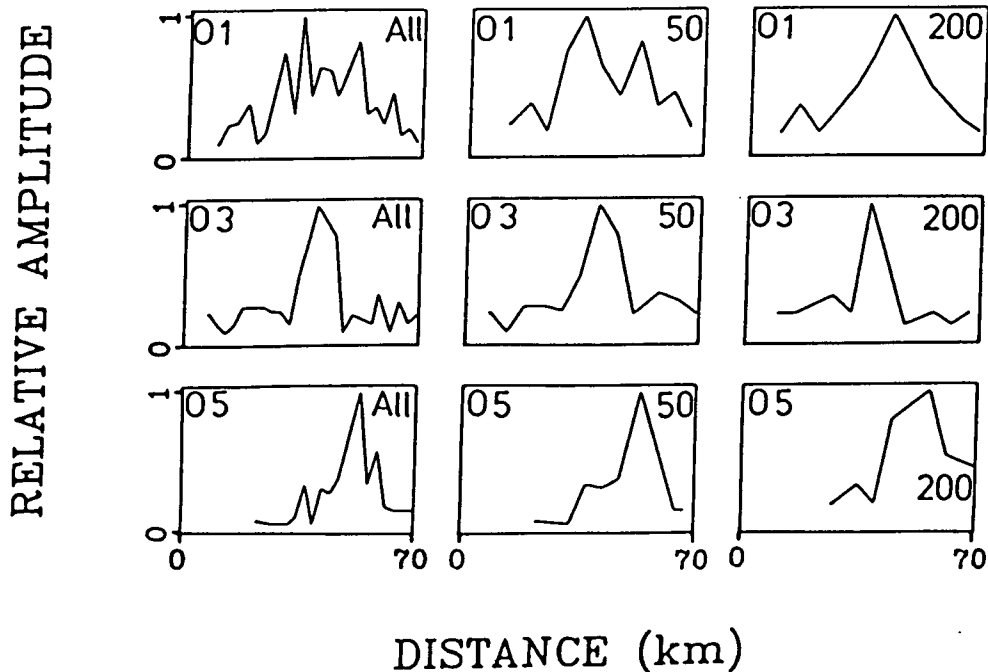


Figure 4.5 Relative amplitude trends and charge size.

These diagrams illustrate the effect of considering different combinations of charges on the relative amplitude distributions for OBS #1, #3, and #5.

The upper diagrams are the variations for OBS #1.

Left: Considering all charges and correcting for the variation in size.

Middle: considering only 50 kg charges

Right: considering only 200 kg charges.

The diagrams for OBS #3 and #5 follow the same pattern: OBS #3, middle; OBS #5, bottom.

Note the large change in distribution shape with different charge combinations. The movement of the main amplitude peak to greater offset from OBS #1 to OBS #5 is present in almost all combinations.

at approximately 34 km offset, for OBS #3 at 40 km, and for OBS #5 at 54 km. The Moho depth is only sampled once for each data set and thus Moho dip refers to the trend of the line connecting sampled points. Some constraint is provided by head waves or mantle turning rays, although the travel time picks involved generally have large error.

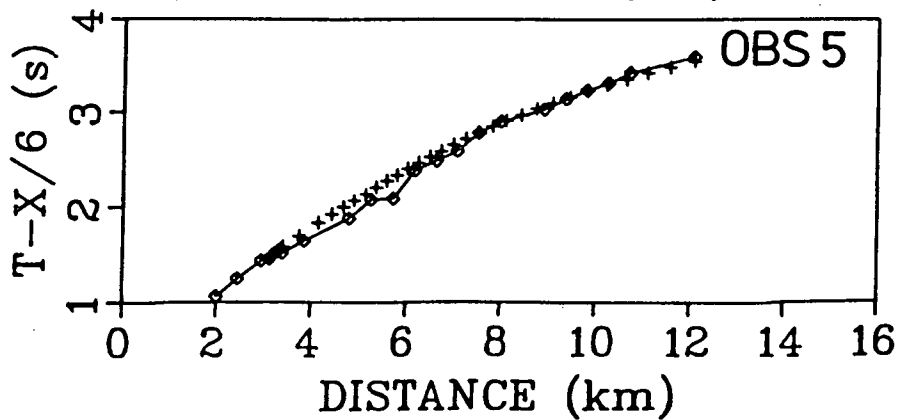
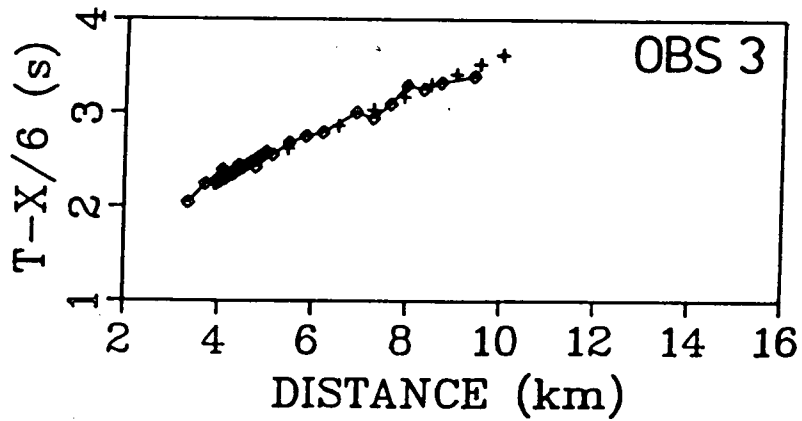
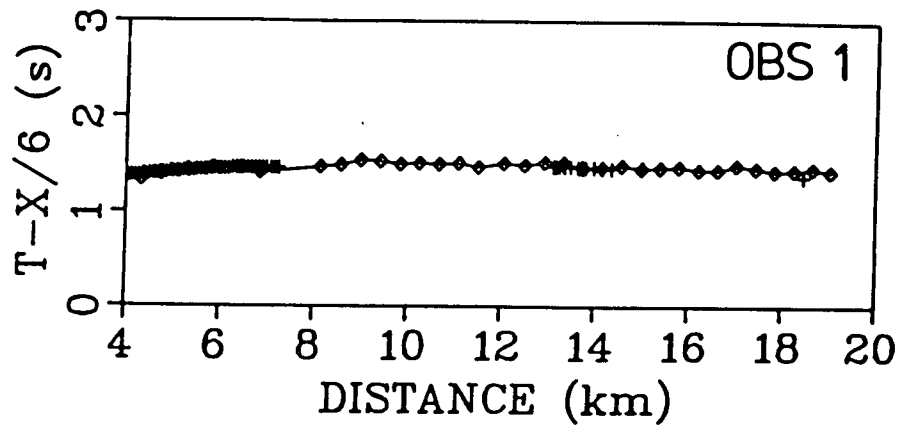
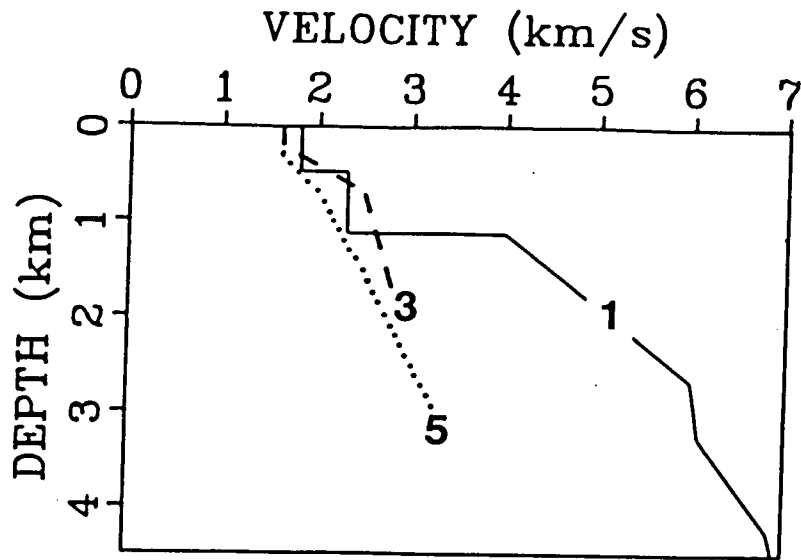
4.6 Construction of Final Models Fitting all the Data

The descending slab structure beneath OBS #1 and #3 was constructed from the one-dimensional structure for OBS# 1 which was derived using the WKBJ algorithm. Under OBS #5 the upper crustal structure was replaced with a block of constant velocity gradient material, required to fit the travel time data. Forward modelling was then performed to produce final models for each of the data sets which were mutually consistent.

4.7 Final Models - a detailed description

One-dimensional seismic structures satisfying the airgun travel time data are shown in figure 4.6, together with a comparison of these data with travel times derived from ray-tracing. Travel time modelling of the explosion data for the three OBSs is illustrated in figures 4.7, 4.9, and 4.11; whilst amplitude modelling with the ART algorithm is shown in figures 4.8, 4.10, and 4.12. Values for the preferred velocities and velocity gradients for the entire structural section are given in figure 4.13.

In all models a group of rays turning in the lower crust produces the observed main amplitude group. The sharp cut-off produced by the ART algorithm is not physical, as noted in section 4.4.



4.7.1 Airgun Models (Figure 4.6)

OBS #1: The derived structure exhibits features characteristic of the upper crust in this region (e.g. Au, 1981; Cheung, 1978). The data constrain sub-sedimentary material velocities and indicate a region of rapid velocity increase (1.4 km/s/km) below the sediment-basement interface. At approximately 2.6 km a velocity of 6.0 km/s is attained and there is a decrease in velocity gradient. Between 3.25 and 4.25 km depth there is a region of relatively rapid velocity increase (gradient = 0.76 km/s/km). The structure is constrained down to almost 4.5 km depth by the airgun information.

OBS #3: The data do not directly constrain the upper few 100 m of sediment, but in order to preserve travel times the velocities must be low: close to 1.6 km/s. At about 200 m depth there is a rapid increase in velocity (gradient = 1.7 km/s/km) to a depth of 0.7 km where the velocity is 2.5 km/s. Here there is a decrease in gradient to 0.3 km/s/km . The structure is constrained down to about 1.8 km depth by the airgun data.

Overleaf: Figure 4.6 Airgun models and data comparison.

Upper: preferred, one-dimensional, shallow velocity-depth structures beneath the three OBSs.

Solid line: under OBS #1

Dashed line: under OBS #3

Dotted line: under OBS #5.

Note that the sediment velocities ($<4.0 \text{ km/s}$) for OBS #1 were derived from CSP and multichannel information, not from direct interpretation of the airgun data.

Lower: comparisons of real travel times with those calculated through the models above. The solid line links the actual first arrival travel time picks, whilst the crosses are computed values.

OBS #5: The derived structure indicates a low velocity 1.6 km/s in the top 200 - 300 m, below which there is a region of rapid velocity increase (gradient = 1.0 km/s/km). At 0.7 km depth, and a velocity of 2.0 km/s, there is a lowering of the gradient to 0.55 km/s/km. The structure is constrained down to almost 3 km depth by the airgun data. The top 2 km of structure are compared to sonic log data in figure D.1; the agreement is good.

4.7.2 OBS #1 Explosion Profile Model (Figures 4.7 and 4.8)

The preferred velocity-depth variation below OBS #1 is illustrated in figures 4.3, 4.4, and 6.1. Derived structure beneath the instrument is typical of marine crust in this region (e.g. Au, 1981). Upper crustal velocities, defined by the airgun data are described in section 4.7.1. The simplest lower crustal structure compatible with the data is a constant velocity gradient of approximately 0.2 km/s/km, changing to 0.01 km/s/km at the Moho where the velocity is 8.0 km/s. This lower crustal gradient region leads to a group of turning rays (figure 4.7b and 4.8a) which produce the observed large amplitudes between 25 and 45 km (figure 4.8 c).

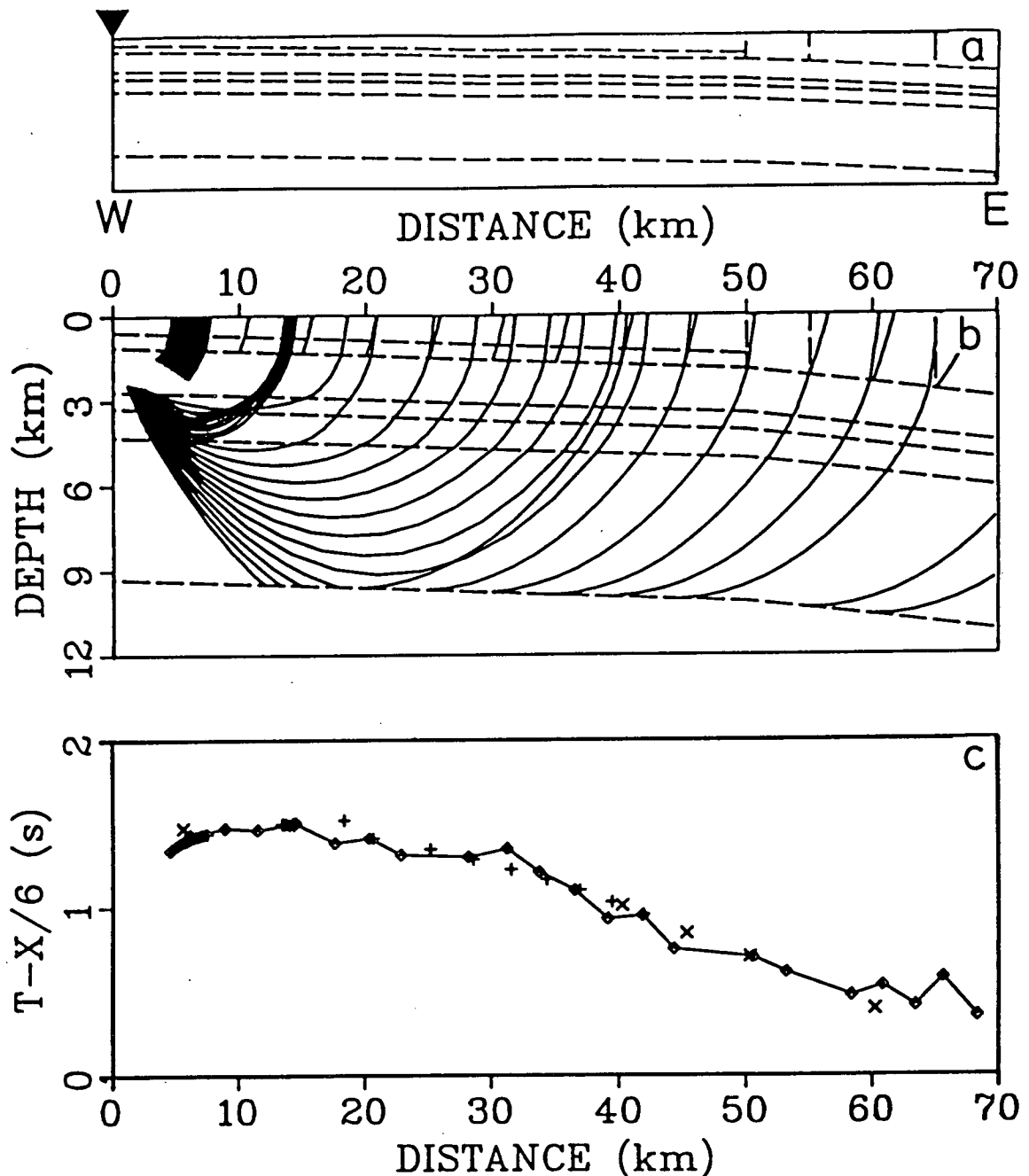


Figure 4.7 OBS #1 travel time model and data comparison.

(a) 1:1 representation of the model boundaries (dashed lines) which separate regions of different velocity and/or velocity gradient, the values of which are shown in figure 4.13.

Note that OBS #1 lies at the western end of the model. The water column is not included in the model.

(b) Ray tracing through the model, following the method of Whittall and Clowes (1979). Rays close to the origin have been artificially blanked off. Regularly spaced arrivals emerging from boundaries 2 and 6 represent head waves. The arrival time difference between head waves produced at the lower boundary (the Moho), and turning rays in the upper mantle is negligible. Head waves are represented here for the purpose of illustration.

(c) Comparison of real and synthetic travel time data. The solid line links real first arrival travel time picks, whilst the crosses are arrival times computed from the ray trace in (b). Vertical crosses are turning rays; diagonal ones, head waves.

The dip of the subducting crust increases from 1° to almost 3° beneath the continental rise. Crustal layers all dip at the same angle as discussed in section 4.2.2. The artificial vertical boundaries in the continental rise region model the lateral increase in velocity from 1.9 to 2.6 km/s.

Overleaf: Figure 4.8 OBS #1 Amplitude model and data comparison.

(a) Ray-trace through a cubic-splined grid of velocity values defining the preferred model, following the ART method of McMechan and Mooney (1980).

Due to the requirements of the algorithm, there are no vertical boundaries; lateral changes in velocity occur smoothly.

The lack of rays at large offset (past 45 km) is, in reality, a severe decrease due to the small velocity gradient in the upper mantle.

The water column is not included in this model.

(b) Synthetic seismograms calculated from the ray-trace above, using asymptotic ray theory (ART). The solid line links first arrival travel times.

Inset shows the relative amplitude variation corresponding to the seismograms. The source wavelet used was obtained from a real data trace, and is illustrated in figure 2.3

Note the sharp cut-off in amplitude past 45 km due to the absence of rays traced by the program in (a).

(c) Filtered (3-15 Hz) record section for OBS #1 explosion data. A charge size correction and an r' enhancement factor have been applied. Times are adjusted to place the shots at 2.52 km depth, thus removing the water column effect.

Solid line links first arrival travel times through the model. Inset shows the relative amplitude variation corresponding to the seismograms.

4.7.3 OBS #3 Explosion Profile Model (Figures 4.9 and 4.10)

The velocity-depth distribution in this model is essentially that for OBS #1, with the distance scale reversed. The sediments under the continental rise have higher velocities than those under OBS #1 as described in section 4.7.1. The triangular wedge at the easterly end is the block of mélange material described in section 4.2.6. Note that the models for OBS #3 (and #5) include the water column, whereas those for OBS #1 do not.

A secondary large amplitude group has been produced by the ART model for OBS #3 but this is not seen in the real section (figure 4.10c). The discrepancy is thought to be due to the high degree of attenuation expected in the continental rise region.

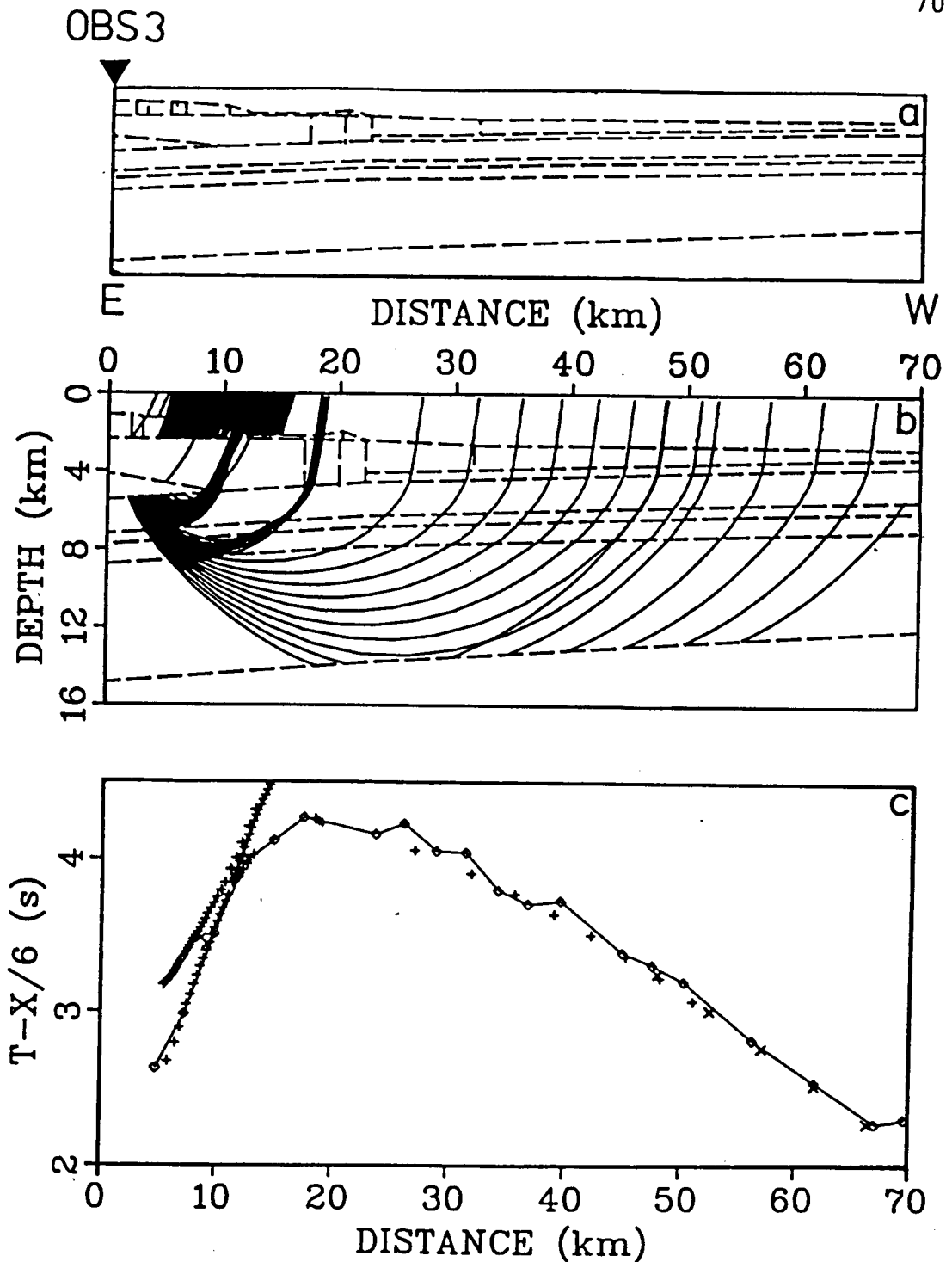


Figure 4.9 OBS #3 Travel-time model and data comparison.

- (a) 1:1 representation of the model boundaries (dashed lines). Values for velocities and velocity gradients are given in figure 4.13. Note that OBS #3 lies at the eastern end of the model. The water column has been included in this model.
- (b) Ray trace performed through the model. Rays close to the origin have been artificially blanked off. Regularly spaced arrivals emerging from the lower boundary (Moho) represent head waves.
- (c) Comparison of real and synthetic travel time data. Solid line links real first arrival travel time picks, whilst crosses are arrival times computed from the ray trace in (b). Vertical crosses are turning rays; diagonal ones, head waves.

OBS 3

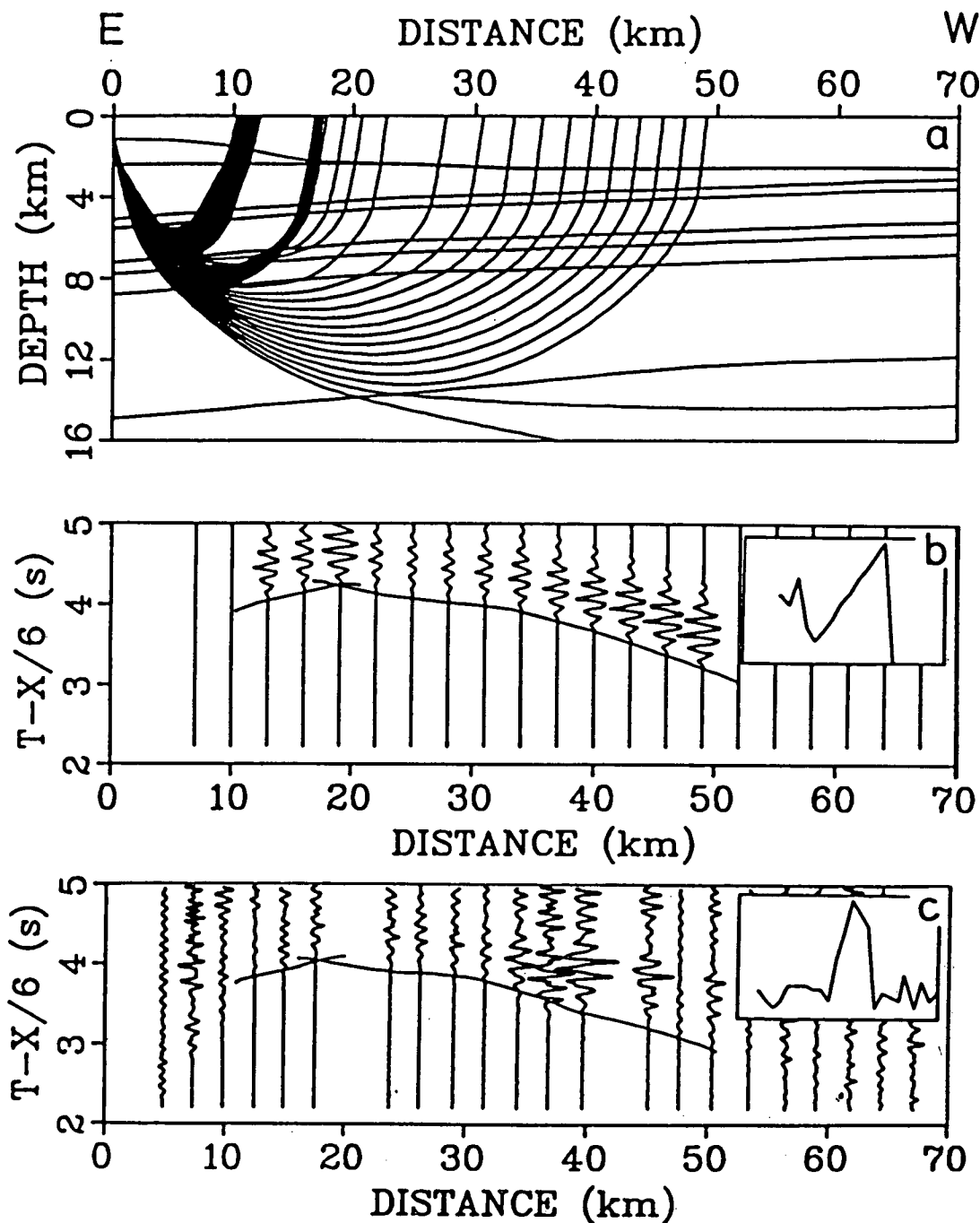


Figure 4.10 OBS #3 Amplitude model and data comparison.

(a) Ray trace performed through a cubic-splined grid of velocity values defining the preferred model. The water column and seafloor topography is included.

(b) Synthetic data calculated from the ray trace above, using ART. Inset shows the relative amplitude variation corresponding to the seismograms.

(c) Filtered (3-15 Hz) section for OBS #3 explosion data. Distance and charge size corrections as for OBS #1 (figure 4.8). Times include the effect of the water column.

Inset shows the corresponding relative amplitude variation.

4.7.4 OBS #5 Explosion Profile Model (Figures 4.11 and 4.12)

The westernmost 70 km of this model is just that used to satisfy the OBS #1 and #3 data. Shallow sediments under the continental slope have relatively high velocities as described in section 4.7.1. At approximately 4 km there is a block of high velocity material ($V > 4.6$ km/s) which has been correlated with a postulated Miocene mélange unit (section 4.2.6). The velocity gradient in this block is about 0.2 km/s/km. The vertical boundary separating this unit from the layered upper crust to the west is not thought to be real, but crudely approximates the expected smooth lateral velocity change. Turning rays in the block of material beneath the rise produce an amplitude group not seen in the real data (figure 4.12). This lack of agreement is thought to be due to attenuation in the highly sheared medium and the very simplified model which must be used for the calculations.

The lower crustal structure remains constant over the whole model, being a velocity gradient region of approximately 0.2 km/s/km. The dip of the Moho increases under the continental slope to approximately 6° .

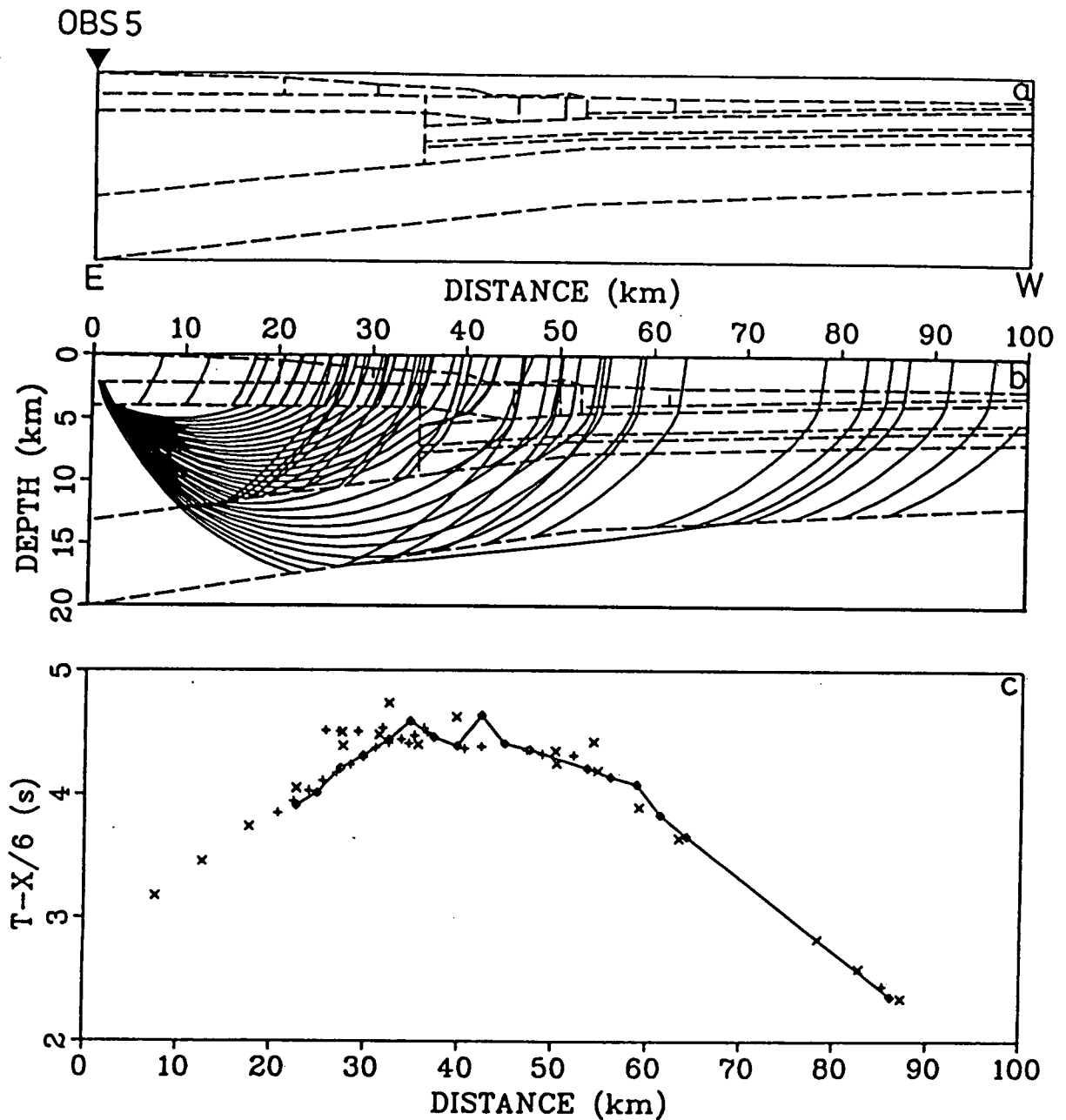


Figure 4.11 OBS #5 Travel-time model and data comparison.

- (a) 1:1 representation of model boundaries (dashed lines). Values for velocities and velocity gradients are given in figure 4.13. Note that OBS #5 lies at the eastern end of the model. The water column and seafloor topography are included.
- (b) Ray trace performed through the model. Regularly spaced arrivals emerging from boundaries 3 and 5 represent head waves. Note that the vertical boundary at 35 km is not thought to be real, but crudely approximates a smooth lateral velocity change.
- (c) Comparison of real and synthetic travel time data. Solid line and crosses as for figures 4.7 and 4.9.

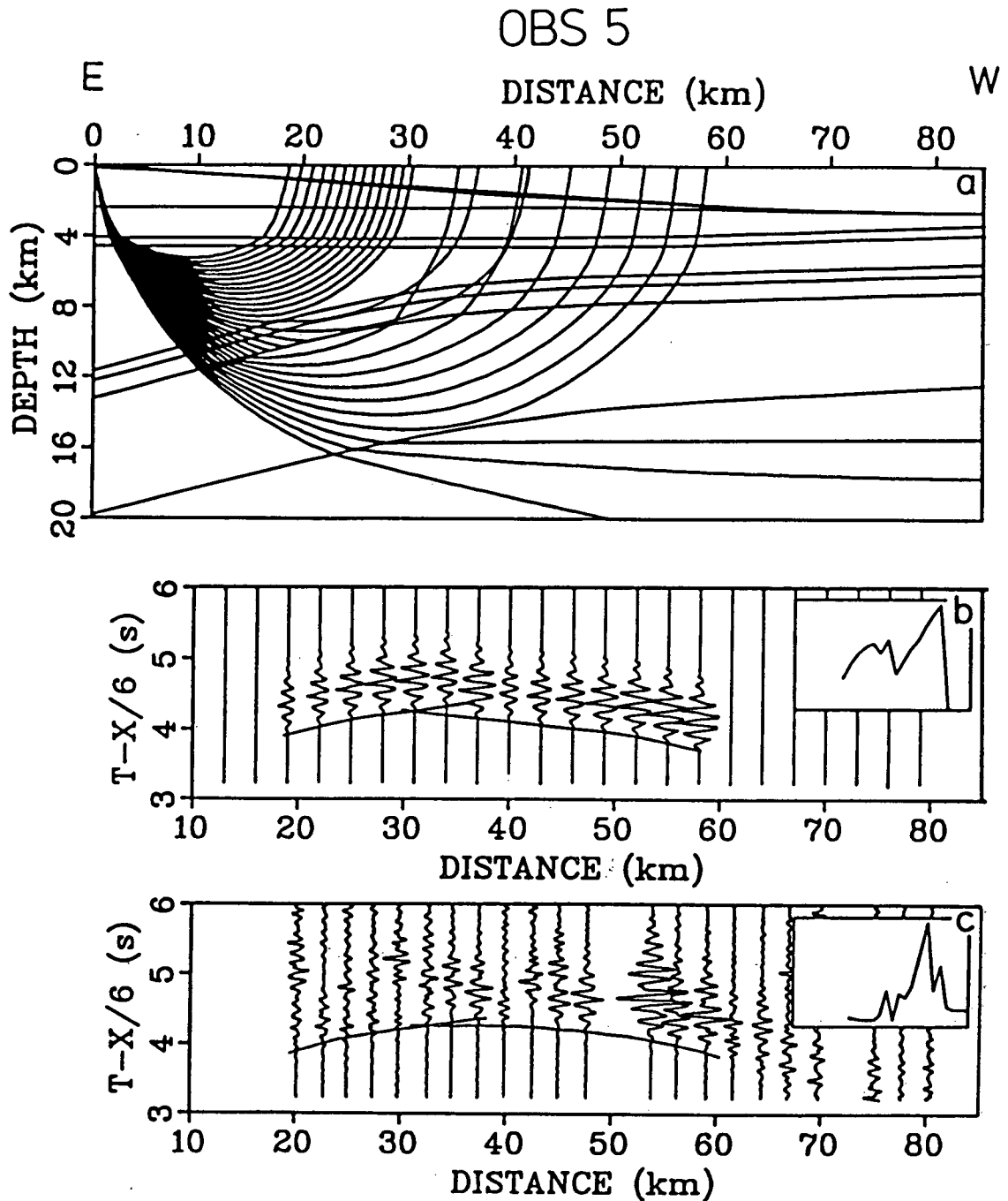


Figure 4.12 OBS #5 Amplitude model and data comparison.

(a) Ray trace performed through a cubic-splined grid of velocity values defining the preferred model. The water column and seafloor topography are included.

(b) Synthetic data calculated from ray trace above, using ART. Inset shows the relative amplitude variation corresponding to the seismograms.

(c) Filtered (3-15 Hz) section for OBS #5 explosion data. Corrections as for OBS #3 (figure 4.10).

Inset shows the corresponding relative amplitude variation.

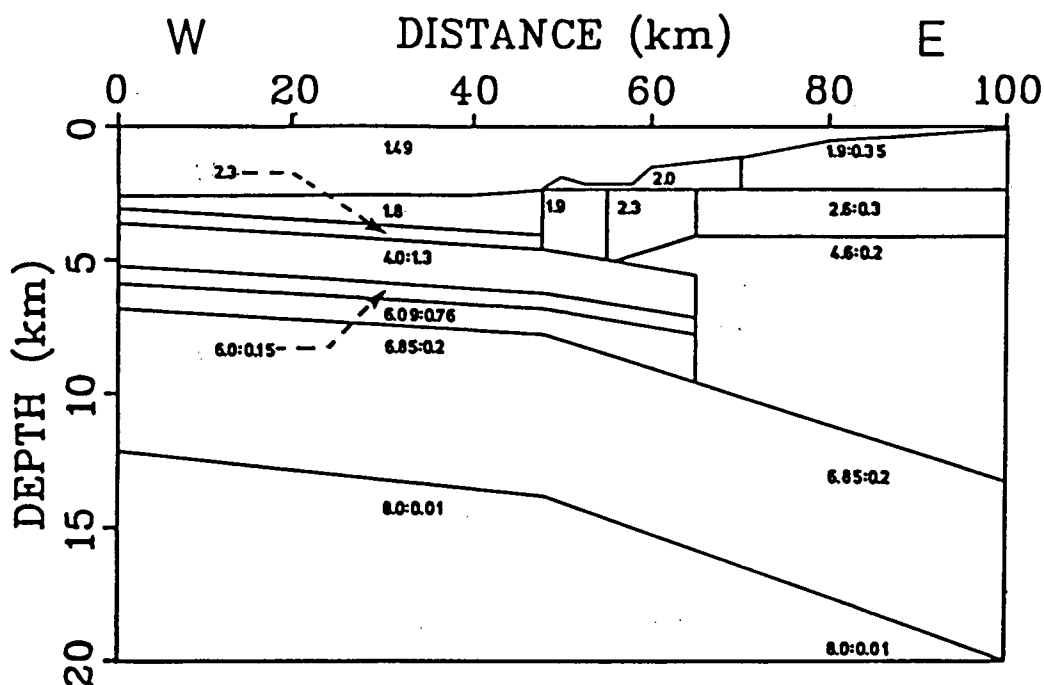


Figure 4.13 Final velocity structure.

Preferred velocities for the continental margin are shown here. The first number gives velocity (in km/s) at the top of a region, followed after the colon by the velocity gradient (in km/s/km) if one was used.

4.8 Interpretation Summary

A two-dimensional seismic structural section has been derived which is consistent with the travel time and amplitude information contained in the separate record sections. Preferred values for velocities and velocity gradients are shown in figure 4.13. Features of the model are discussed in Chapter 6.

Any derived seismic structure should be consistent with observed gravity variations over that structure. Consistency between gravity data and the preferred seismic model has been checked by conversion of compressional-wave velocities to densities, and is discussed in the next chapter.

" Gravity and lightness are only attraction and flight. Nothing is naturally heavy or light'."

CHAPTER 5 Gravity Interpretation

5.1 On the Analysis of Gravity Data

The interpretation of gravity information has a higher degree of associated non-uniqueness than that involving seismic travel time and amplitude data. A given anomaly may be produced by an infinite number of bodies of varying density, shape, and depth.

The most frequently used method of gravity anomaly interpretation is by two-dimensional forward modelling (e.g. Molnar, 1977). Modifications to an initial model are based upon a subjective "goodness of fit" criterion when comparing the calculated and observed gravity variations. Oldenburg (1974) has formulated an iterative inversion scheme involving Fourier transforms of the gravitational anomaly. The method is fast enough to be practical for an iterative approach, but is limited by the assumptions that an observed anomaly is caused by a single surface between two constant density media and that the perturbing body is two-dimensional.

In all gravity interpretations additional geophysical information is used to constrain the models and in general, only large scale features are modelled. Detailed models containing many small blocks of material of different density,

¹Giordano Bruno

such as that due to Couch and Braman (1979), should be viewed with extreme caution. Whilst fitting the observed gravity variation almost exactly, the degree of model complexity is misleading; many different combinations of small blocks with differing densities and depths could fit the data equally well.

The aim behind gravity modelling should be the same as that behind refraction data analysis, i.e. to produce the model which has the least structure compatible with all the data. For the purposes of crustal studies, it is generally not necessary to model small variations in the gravity anomaly which may be due to local, near-surface variations in density.

In many interpretations, discontinuities in structure derived from seismic data analysis are used to delineate blocks of material of differing density. Whilst this procedure may be valid in many situations, it should be treated with caution as seismic velocity variations do not depend solely on density variations.

In order to constrain a seismic velocity model with a gravity data interpretation, regions of different wave velocity must be assigned densities. Empirical relations between density and velocity are derived from laboratory measurements on rock samples. In marine work, samples are often obtained from the Deep Sea Drilling Project (DSDP) and are tested under pressure and water saturation conditions closely resembling those experienced by material in situ.

The most used velocity-density curve has been that of Nafe and Drake; first published in 1957, and updated several

times (Nafe and Drake, 1963; Talwani et al., 1959b). Hamilton (1978) presents separate v - ρ relationships for principal sediment and rock types in the sea floor; some v - ρ values for sediments are given in Table 5.1.

V (km/s)	ρ (g cm ⁻³)
1.9	2.0
2.0	2.1
2.25	2.2
2.50	2.3
2.8	2.4
3.3	2.5

Table 5.1 Compressional-wave velocity vs. density in marine sediments. $\rho=0.917+0.744V-0.08V^2$ (after Hamilton, 1978)

5.2 Gravity Data Description.

A gravity anomaly map (free air over the ocean, Bouguer on land) has been compiled for the region including southwestern British Columbia and northwestern United States (Riddihough, 1979). A number of profiles perpendicular to the coast were interpreted to study the change in subduction regime from northern Vancouver Island to Oregon. In particular, profile 2 (figure 5.1) was nearly coincident with VISP-80 line I.

The large scale structure of the continental margin along this profile was modelled by Riddihough (1979), using the gravity data and additional seismic constraints. As noted in section 1.2, the broad features of the gravity field, the parallel 'low-high' system corresponding to the trench and the

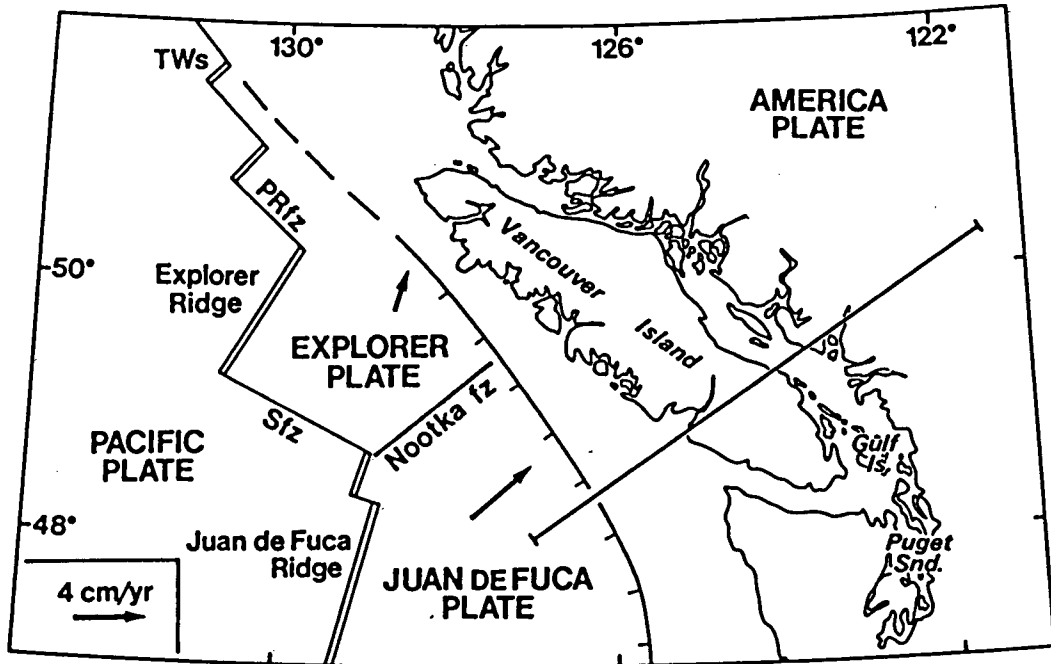


Figure 5.1 Location map of gravity profile.

Solid line indicates position of the profile, superimposed on a simplified tectonic map of the region.

arc-trench gap, are features which elsewhere are characteristic of an active margin.

In figure 5.2 (lower) the free air gravity anomaly over the marine portion of the profile in figure 5.1 is shown. Over Cascadia Basin on the west, the average gravity anomaly is near zero, indicating that the region is essentially in isostatic equilibrium. The anomaly becomes negative over the continental slope, reflecting the sediment-filled margin trench. The positive anomaly over the outer shelf is due to shallowing water depth and the greater sediment densities here. Rapidly decreasing gravitational attraction over the inner shelf reflects low density Tofino Basin sediments.

5.3 Gravity Data Interpretation

5.3.1 Method

Forward modelling of the gravity information was performed with the aid of an algorithm which computes the gravitational attraction due to arbitrarily shaped polygons in two dimensions, as described in Appendix G. The continental margin off Vancouver Island is thought to be an approximately linear feature over 50 km to the north and south. Thus, the assumption of two-dimensionality of the layers is expected to introduce relatively small errors.

An initial input model for the algorithm was constructed by forming regions of fixed density with boundaries in the same positions as those of the preferred seismic model (figure 4.13). The densities of the sedimentary blocks were chosen from the average seismic velocities for the regions by use of the relationships shown in table 5.1. Upper crustal density was taken as 2.62 g cm^{-3} after Couch and Braman (1979), whilst a lower crustal density of 2.92 g cm^{-3} was used, following Riddihough (1979). A velocity-density relation for the block of highly sheared *mélange* proposed by Snavely and Wagner (1981), and indicated by the VISIP-80 data, may only be guessed at, as the true nature of the material is unknown. In forward modelling, the *mélange* block density was left as a free parameter.

The allocation of densities to compressional-wave velocity regions is inherently inaccurate for two reasons. Firstly, the relationships between v and ρ are empirical and one velocity is related to a range of densities; secondly,

many regions in the seismic model have velocity gradients, but only one density is used to model the region. It is therefore possible to perturb the densities of a given gravity model whilst still maintaining consistency with a corresponding seismic structure.

In order to model observed gravity variations over the 100 km long profile between OBS #1 and #5, a density structure must be assumed well beyond the limits of this profile, and must extend much deeper than the maximum depth sampled by the seismic data to eliminate end effects. The central region of the Juan de Fuca plate is thought to be approximately laterally homogeneous; thus structure west of the seismic profile was modelled as plane layers with the same density stratification as the units below OBS #1. East of the profile the earth is known to be highly laterally variable. The structure proposed by Riddihough (1979) was employed to model the descending crust and transition to continental material beneath Vancouver Island. Densities down to 200 km depth were incorporated into the model; values for lithospheric mantle ($\rho=3.34 \text{ g cm}^{-3}$, thickness 13.1 km) and asthenospheric mantle ($\rho=3.295 \text{ g cm}^{-3}$, thickness 176.5 km) were taken from Riddihough (1979).

Synthetic gravity variations were computed at stations 10 km apart; a separation similar to that between the real data points obtained from the gravity anomaly map.

5.3.2 Model Description

The preferred density structure for the continental

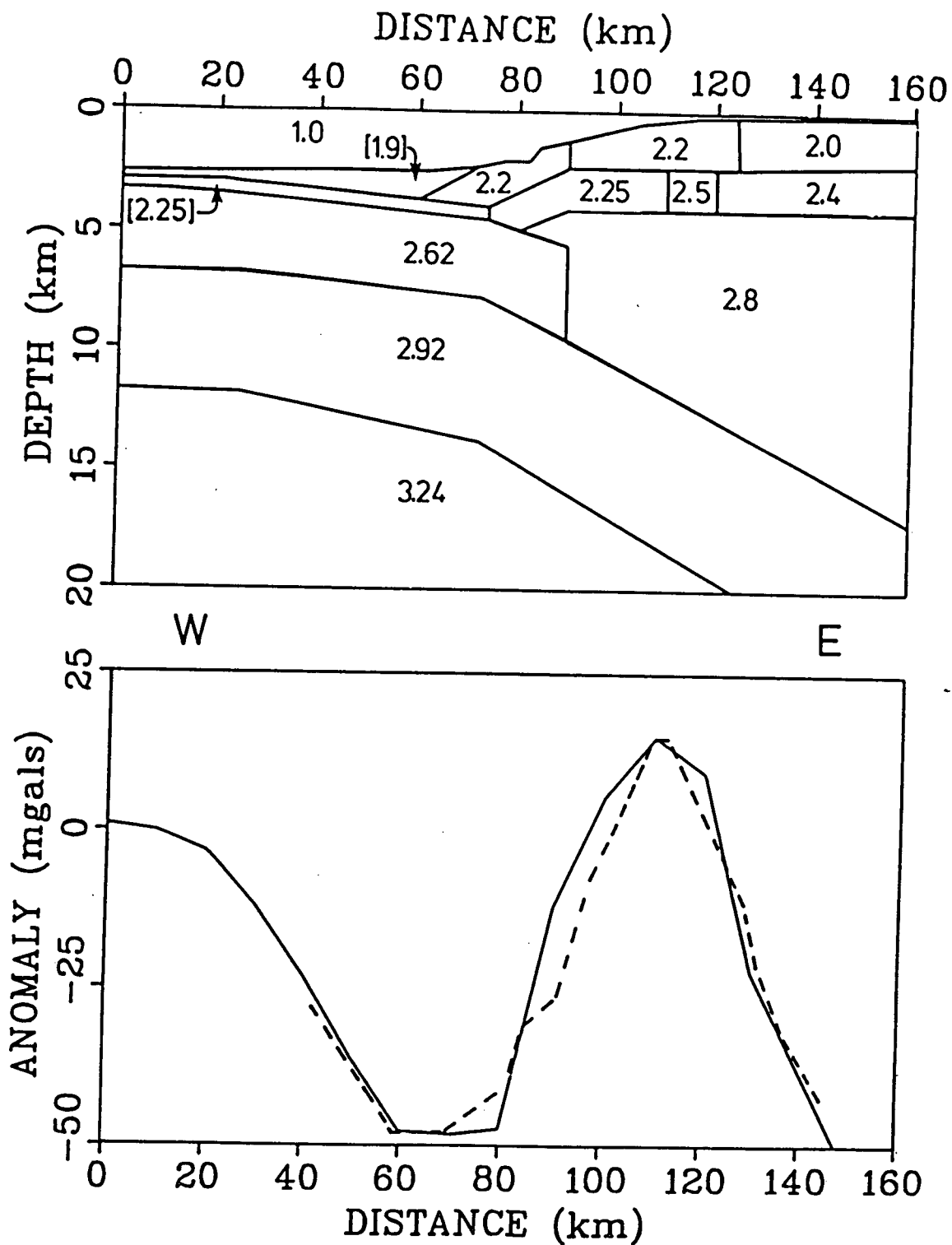


Figure 5.2 Gravity model and data comparison.

Upper: Preferred gravity structure. The boundaries correspond to those in the seismic model (figure 4.13). Densities are shown in g cm^{-3} .
 Lower: Computed anomaly (solid line), compared to real data (dashed line); there is close agreement. Station spacing for both variations is 10 km.

margin is shown in figure 5.2 (upper). The seismic profile extends from approximately 25 to 125 km on the distance scale shown. All sub-sedimentary boundaries correspond exactly to those in the preferred seismic model (figure 6.1); however, the upper crustal structure between OBS #1 and the continental rise is given one density (2.62 g cm^{-3}), whereas the seismic model includes three different velocity gradient regions. The difference in calculated anomaly between this procedure and allocation of densities to the individual layers of the upper crust is negligible.

Derived densities and seismic velocities (figure 6.1) are consistent (given the inherent uncertainties involved in the allocation of ρ to v) with the empirical relationships shown in table 5.1. Major boundaries between blocks of sediment with differing density are not thought to be real. Relatively smooth variations in the physical properties of the material are expected, although some shallow fault bounded blocks are indicated by the CSP data (figure 1.3), and deeper faults have been interpreted from a multichannel reflection section (Appendix H).

The upper sedimentary block lying between 124 km and the eastern edge of the model (figure 5.2) represents the Tofino Basin sediments. This structure lies to the east of OBS #5, and is thus unconstrained by the VISP-80 seismic data. As noted in section 5.2, the presence of relatively low density Tofino Basin sediments is required to produce a rapid decrease in gravitational attraction over the inner shelf.

The preferred density for the block of mélangé material

is 2.8 g cm^{-3} . This is undoubtedly an average value. The boundaries of this region are only crudely defined by seismic refraction data; both velocities and densities are expected to be highly laterally and vertically variable within the block. A density of 2.8 g cm^{-3} and seismic velocities ranging from 4.6 to 6.0 km/s are too high for standard marine sedimentary material (Hamilton, 1978); these values are more characteristic of basalts than of sediment. V - ρ relations in basalts from the boreholes of the Deep Sea Drilling Project (Christensen and Salisbury, 1975) indicate a velocity of $\sim 5.7 \text{ km/s}$ for a density of 2.8 g cm^{-3} . The lower average seismic velocity derived for the *mélange* ($\sim 5.3 \text{ km/s}$) may be due to the highly sheared nature of the basaltic material composing the block. Seismic velocity may be further reduced by incorporation of sedimentary material into fissures formed in the upper section of the block. Thus the preferred average velocity and density values are consistent with the notion that a *mélange* has been formed by deformation of upper oceanic crustal material.

The computed gravity anomaly from the preferred model is compared with real data in figure 5.2 (lower). Broad features of the anomaly have been matched i.e. the amplitude and wavelength of the sine function shaped variation. The greatest discrepancies between observed and calculated values occur in the continental rise region. This disagreement is expected, due to the modelling of this complex area with simple, block structures.

The real gravity data have been modelled by using simple,

relatively large scale regions of constant density. Errors will be introduced as described above from violations of the two-dimensionality assumption, and inaccurate allocation of densities to seismic velocities. When reasonable fits to observed gravity anomalies can be produced with very simple sub-sedimentary structures, the lack of constraint provided by gravity data becomes apparent.

Although it is encouraging to find consistency between the gravity and seismic models, it should be remembered that the gravity data only constrain possible density structures very loosely, due to the inherent non-uniqueness of the data inversion. For example, gravity information provides no additional details regarding position of the relatively low density contrast Moho boundary.

" The end proveth everything¹."

CHAPTER 6 Summary and Discussion

A structural model for the subducting Juan de Fuca plate at the continental margin off British Columbia has been interpreted from a seismic refraction profile recorded on three ocean bottom seismographs. Derived seismic models were constrained by continuous seismic profiles, multichannel seismic reflection sections, well-log data, and gravity information. The modelling procedure adopted throughout this study was to produce the simplest velocity and density structures possible, whilst retaining consistency with all geophysical information available. The term 'simplest' as applied here is a subjective quality. No purely mathematical definition can be expressed for two-dimensional seismic structures.

The derived structural model for the continental margin is shown in figure 6.1. Each of the blocks has a fixed density, compressional-wave velocity at the upper boundary, and velocity gradient. Vertical boundaries in the model are not thought to be real, but crudely approximate smooth lateral changes in velocity and density.

Velocities for the sediments are constrained by travel times from a CSP, normal moveout velocity determinations, travel times from multichannel reflection sections, sonic logs

¹John Gower

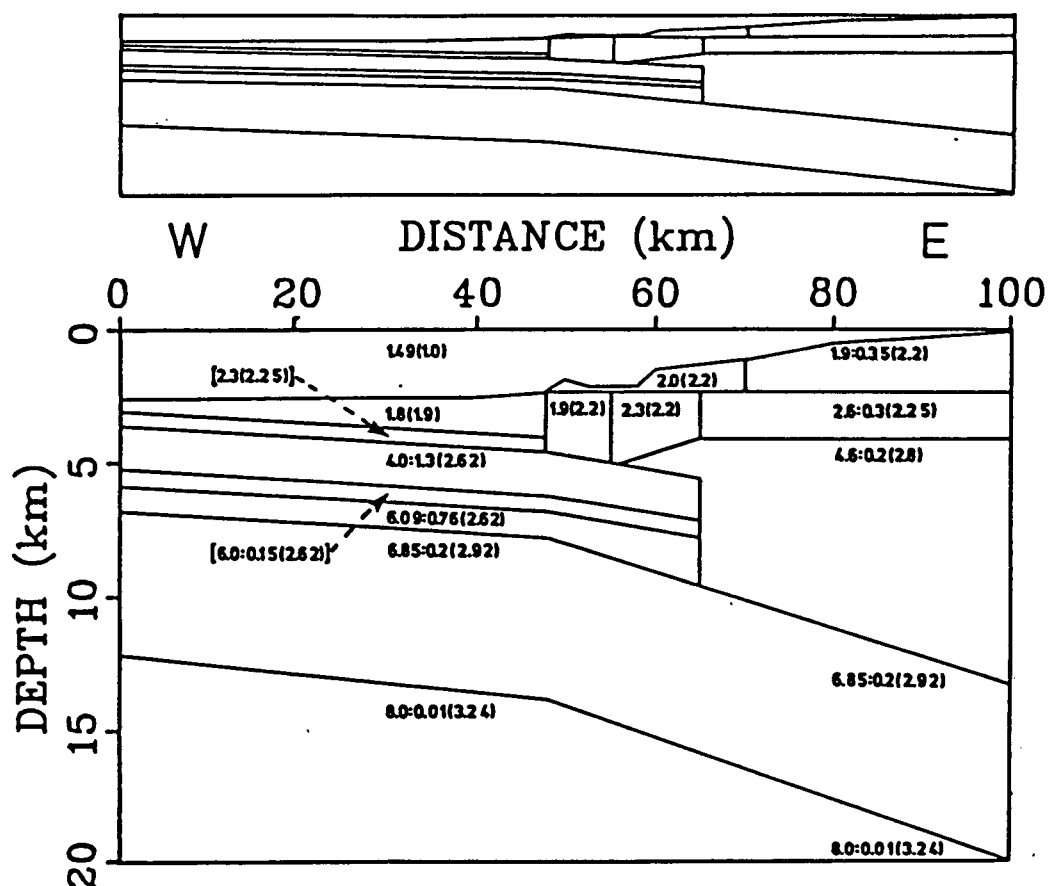


Figure 6.1 Final velocity and density structure.

Upper: 1:1 representation of model boundaries.

Lower: Preferred velocities and densities for the continental margin are shown here. The first number gives velocity (in km/s) at the top of a region, followed after the colon by the velocity gradient (in km/s/km; if one was used). The number following, in brackets, is the density (in g cm^{-3}).

from a nearby well, and the interpretation of VISP-80 airgun data. These velocities increase eastwards in the continental rise region; a concomitant increase in density is also required. Such increases are due to greater compression and compaction of material at the margin. These compressive structures (asymmetric folds and northeastward dipping imbricate thrusts; figure 6.2) result from the relative

northeastward underthrusting of the Juan de Fuca beneath the North America plate. East of OBS #5 where there is no seismic control, gravity modelling requires that the density of upper sedimentary material must decrease; an accompanying decrease in seismic velocities is expected. This is consistent with seismic reflection data which shows the presence of undeformed sediments in Tofino Basin on the continental shelf.

The stratified upper crustal velocity sequence which has been derived beneath the deep ocean is similar to that deduced from other studies on the Juan de Fuca plate. In terms of the conventional layered model of the oceanic crust, layer 1, the 1 km thick sequence of marine sediments, ranges in velocity from 1.8 km/s to 2.3 km/s. Layer 2, probably containing pillow basalts and sheeted basalt dikes (Christensen, 1978), ranges in velocity from 4.0 km/s, at the sediment-basement interface, to almost 7.0 km/s at ~ 7 km depth. A relatively high velocity gradient region ($dv/dz=0.76$ km/s/km) marks the transition from layer 2 to layer 3, the lower crust.

The sediment-basement interface dips eastward at 1.4° ; sub-basement layers are assumed to be dipping at the same angle. These layers, separated by changes in velocity gradient, increase in dip to about 3° under the continental rise. Beneath the outer edge of the continental shelf there is a structural change from the relatively high velocity layers of the upper oceanic crust to a lower average velocity block ($v \approx 5.3$ km/s) of constant gradient, extending down more than 5 km from a depth of 4 km. There is no evidence for a sharp transition from one region to the next; the transition is

thought to be a comparatively gradual one. The position of this block agrees well with that of a middle Miocene mélangé unit proposed by Snavely and Wagner (1981), (figure 6.2).

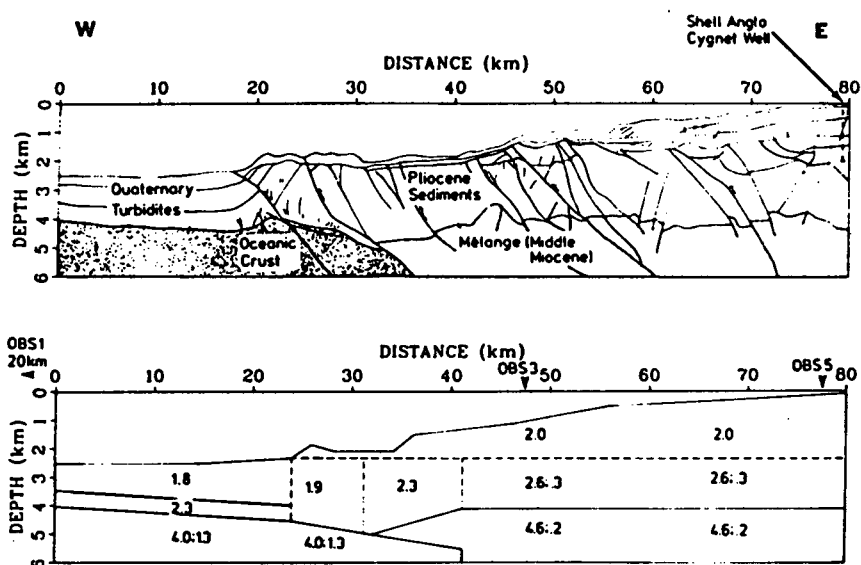


Figure 6.2 Geological interpretation of the upper crustal structure.

Upper: A geological interpretation based on U.S.G.S. multichannel data (appendix H) after Snavely and Wagner (1981). The structural horizons which were picked on the travel time section have been rescaled to depth by using the refraction velocities derived in the VISP-80 data interpretation (Chapter 4).

Lower: Preferred model for upper crustal structure. Numbers indicate seismic velocities of the blocks (in km/s); followed, after the semi-colon, by the velocity gradient (in km/s/km), if a gradient was used.

Note that the block of 4.6 km/s material agrees well with the position of the mass of mélangé proposed by the U.S.G.S. study.

The lower crust has been modelled as a constant velocity gradient region, extending down to 9 km below sea floor in the deep ocean, and may consist of metadolerite sheeted dikes underlain by metagabbro and olivine-pyroxene gabbros (Salisbury and Christensen, 1978). This velocity structure

remains constant over the entire marine profile, suggesting that the overlying mélange material may have been formed as upper layers were scraped off the descending oceanic plate.

Absolute plate motion studies (Minster and Jordan, 1978) indicate that the Juan de Fuca plate is subducting beneath, and also being overridden by the North American plate. The mélange unit may represent a downward continuation of the "accretionary wedge" envisaged by the imbricate thrust model for subduction zones, (Beck, 1972; Seely et al. 1974). However, analysis of drilling data at convergent margins (e.g. Moore et al. 1982) does not indicate incorporation of basaltic basement into an accretionary wedge, either by offscraping or underplating¹ of material. It is conceivable that the young age of the Juan de Fuca plate together with the overriding motion of the North America plate produce a unique tectonic regime where there is accretion of sub-sedimentary material at the margin.

Complete detachment of the upper crust from the descending plate below, if it occurs, must be a relatively recent process; 3 km of crustal material would produce a mass 900 km^2 in cross-section in 1 Ma. It is more probable that the mélange material merely indicates a resistance to subduction by the continental crust, the upper oceanic crustal layers being compressed and deformed whilst still remaining attached to the Juan de Fuca plate.

¹In the process of underplating, sedimentary material is added to the accretionary wedge from below, in addition to being scraped off in the continental rise region.

The Moho has been modelled as a change in velocity gradient from 0.2 km/s/km in the lower crust to 0.01 km/s/km in the upper mantle. Resolution of Moho structure is poor, but no velocity discontinuity at the boundary is required by the data, although a small change of the order of 0.2 km/s is still compatible with the data. There is an increase in Moho dip under the continental rise from about 1° to 6° .

The convergent margin structure between Juan de Fuca and America plates is anything but simple. It would have been possible to satisfy all of the seismic, gravity, and additional information more closely by introducing sufficient structural complexity into the model. This approach was rejected. Obtaining features common to all physically plausible structures is considered to be more valuable than exactly fitting data with large associated errors. Consequently, the interpreted model (figure 6.1) is not a representation of the real earth, but rather an illustration of certain basic structural features associated with this convergent tectonic environment.

BIBLIOGRAPHY

- Adams, J., and R. Reilinger, Time behaviour of vertical crustal movements measured by releveing in North America: a geologic perspective. In Proc. 2nd Int. Symp. on problems related to redefinition of North American Vertical Geodetic Networks (NAD). Can. Inst. Surveying, Ottawa, Ont., pp. 327-339, 1980.
- Aki, K., and P.G. Richards, Quantitative Seismology - Theory and Methods. W.H. Freeman and Company, San Francisco. 2 vols. 1980.
- Ando, M., and E. Balazs, Geodetic evidence for aseismic subduction of the Juan de Fuca plate. J. Geophys. Res., 84, 3023-3028, 1979.
- Atwater, T., Implications of plate tectonics for the Cenozoic tectonic evolution of western North America. Geol. Soc. Am. Bull., 81, 3513-3536, 1970.
- Au, C.Y.D., Crustal structure from an ocean bottom seismometer survey of the Nootka fault zone. Ph.D. Thesis, Univ. of British Columbia, Vancouver, 131 pp. 1981.
- Au, C.Y.D., and R.M. Clowes, Crustal structure from an OBS survey of the Nootka fault zone off western Canada. Geophys. J. R. Astron. Soc., 168, 27-48, 1982.
- Barr, S.M., Structure and tectonics of the continental slope west of southern Vancouver Island. Can. J. Earth. Sci., 11, 1187-1199, 1974.
- Bates, A.C., and E.R. Kanasevich, Inversion of seismic travel times using the tau method. Geophys. J. R. Astron. Soc., 47, 59-72, 1976.
- Beck, R.H., The oceans, the new frontier in exploration. Aust. Pet. Ex. Assoc. J., 12, 1-21, 1972.
- Berry, M.J., Depth uncertainties from seismic first-arrival refraction studies. J. Geophys. Res., 76, 6464-6468, 1971.
- Bessonova, E.N., V.M. Fishman, V.Z. Ryaboyi, and G.A. Sitnikova, The tau method for inversion of travel times - I. Deep seismic sounding data. Geophys. J. R. Astron. Soc., 36, 377-398, 1974.
- Braile, L.W., and R.B. Smith, Guide to the interpretation of crustal refraction profiles. Geophys. J. R. Astron. Soc., 40, 145-176, 1975.
- Carson, B., Acoustic stratigraphy, structure, and history of

- Quaternary deposition in Cascadia Basin. *Deep Sea Res.*, 20, 387-396, 1973.
- Červený, V., I.A. Molotkov, and J. Pšenčík, Ray method in Seismology, Universita Karlova, Praha, 214 pp, 1977.
- Červený, V., Ray theoretical seisograms for laterally inhomogenous structures. *J. Geophys. Res.*, 46, 335-342, 1979.
- Chapman, C.H., A new method for computing synthetic seisograms. *Geophys. J. R. Astron. Soc.*, 54, 481-518, 1978.
- Chase, R.L., D.L. Tiffin, and J.W. Murray, The western Canadian continental margin. In *Canada's Continental Margins and Offshore Petroleum Exploration*, edited by C. Yorath, E. Parker and D. Glass. *Can. Soc. Pet. Geol., Memoir 4*, 701-721, 1975.
- Cheung, H.P.Y., Crustal structure near Explorer Ridge: ocean bottom seismometer results parallel to Revere-Dellwood fracture zone. M.Sc. Thesis, Univ. of British Columbia, Vancouver, 80 pp, 1978.
- Choy, G.L., Theoretical seisograms of core phases calculated by frequency-dependent full wave theory, and their interpretation. *Geophys. J. R. Astron. Soc.*, 51, 225-312, 1977.
- Christensen, N.I., Ophiolites, seismic velocities, and oceanic structure. *Tectonophysics*, 47, 131-157, 1978.
- Christensen, N.I., and M.H. Salisbury, Structure and constitution of the lower oceanic crust. *Rev. Geophys. Space Phys.*, 13, 57-86, 1975.
- Clayton, R.W., and G.A. McMechan, Inversion of refraction data by wave field continuation. *Geophysics*, 46, 860-868, 1981.
- Clee, T.E., K.G. Barr, and M.J. Berry, Fine structure of the crust near Yellowknife. *Can. J. Earth. Sci.*, 11, 1534-1549, 1974.
- Clowes, R.M., and S. Knize, Crustal structure from a marine seismic survey off the west coast of Canada. *Can. J. Earth. Sci.*, 16, 1265-1280, 1979.
- Couch, R., and D. Braman, Geology of the continental margin near Florence, Oregon. *Oregon Geology*, 41, No. 11, 1979.
- Crosson, R.S., Small earthquakes, structure and tectonics of the Puget Sound region. *Bull. Seismol. Soc. Am.*, 62, 1133-1172, 1972.

- Davydova, N.I., Possibilities of the DSS technique in studying properties of deep-seated seismic interfaces, in *Seismic Properties of the Mohorovičić Discontinuity*, edited by N.I. Davydova, National Technical Information Service, U.S. Dept. of Commerce, Springfield, Va, 4-22, 1975.
- Detrick, R.S., and G.M. Purdy, The crustal structure of the Kane fracture zone from seismic refraction studies. *J. Geophys. Res.*, 85, 3759-3777, 1980.
- Dix, C.H., Seismic velocities from surface measurements. *Geophysics*, 20, 68-86, 1955.
- Fowler, C.M.R., and C.E. Keen, Oceanic crustal structure - Mid-Atlantic Ridge at 45° N. *Geophys. J. R. Astron. Soc.*, 56, 219-226, 1978.
- Fuchs, K., On the properties of deep crustal reflectors. *Geophysics*, 35, 133-149, 1969.
- Fuchs, K., and G. Muller, Computation of synthetic seismograms with the reflectivity method and comparison with observations. *Geophys. J. R. Astron. Soc.*, 23, 417-433, 1971.
- Garmany, J., J. Orcutt, and R. Parker, Travel time inversion: a geometrical approach. *J. Geophys. Res.*, 84, 3615-3622, 1979.
- Hale, L.D., and G.A. Thompson, The seismic reflection character of the continental Mohorovičić discontinuity. *J. Geophys. Res.*, 87, 4625-4635, 1982.
- Hamilton, E.L., Sound velocity-density relations in sea-floor sediments and rocks. *J. Acoust. Soc. Am.*, 63, 366-377, 1978.
- Healy, J.H., Crustal structure along the coast of California from seismic refraction measurements. *J. Geophys. Res.*, 68, 5777-5787, 1963.
- Herglotz, G., Über das benndorfsche problem der fortpflanzungsgeschwindigkeit der erdbebenstrahlen. *Phys. Z.*, 8, 145-147, 1907.
- Horn, J.R., A snapshot of the Queen Charlotte Fault zone obtained from P-wave refraction data. M.Sc. Thesis. Univ. of British Columbia, Vancouver, 79 pp, 1982.
- Hubbert, M., A line integral method of computing the gravimetric effects of 2-D masses. *Geophysics*, 13, 215-225, 1948.
- Hyndman, R.D., Heat flow measurements in the inlets of southwestern British Columbia. *J. Geophys. Res.*, 81, 337-349, 1976.

- Hyndman, R.D., R.P. Riddihough, and R. Herzen, The Nootka Fault zone - A new plate boundary off western Canada. *Geophys. J. R. Astron. Soc.*, 58, 667-683, 1979.
- Hyndman, R.D., and D.H. Weichert, Seismicity and rates of relative motion on the plate boundaries of western North America. *Geophys. J. R. Astron. Soc.*, in press. 1982.
- Johnson, L.E., and F. Gilbert, Inversion and inference for teleseismic ray data, in *Methods in Computational Physics*, edited by B.A. Bolt, Academic, New York, 11, 231-266, 1972.
- Johnson, R.V. II, C.R.B. Lister, and B.T.R. Lewis, A direct recording ocean bottom seismometer, *Mar. Geophys. Res.*, 3, 65-85, 1977.
- Jurkevics, A., R. Wiggins, and L. Canales, Body-wave inversion using travel time and amplitude data. *Geophys. J. R. Astron. Soc.*, 63, 75-93, 1980.
- Keen, C.E., and R.D. Hyndman, Geophysical review of the continental margins of eastern and western Canada. *Can. J. Earth. Sci.*, 16, 712-744, 1979.
- Kanestrøm, R., O. Øvrebø, Seismic measurements of large underwater shots, *Geophysica, Geophys. Soc. of Finland*, 15, 215-229, 1978.
- Kennett, B.L.N., A Comparison of travel-time inversions. *Geophys. J. R. Astron. Soc.*, 44, 517-536, 1976.
- Kennett, B.L.N., and J.A. Orcutt, A comparison of travel time inversions - marine refraction profiles. *J. Geophys. Res.*, 81, 4061-4070, 1976.
- Krebes, E.S., and F. Hron, Comparison of synthetic seismograms for an elastic media by asymptotic ray theory and the Thomson-Haskell Method. *Bull. Seismol. Soc. Am.*, 71, 1463-1468, 1980.
- Levy, S., and R.M. Clowes, Debubbling: a generalized linear inverse approach. *Geophys. Prosp.*, 28, 840-858. 1980.
- Lister, C.R.B., and B.T.R. Lewis, An ocean-bottom seismometer suitable for arrays. *Deep Sea Res.*, 23, 113-124, 1976.
- McMechan, G.A., and W.D. Mooney, Asymptotic ray theory and synthetic seismograms for laterally varying structures. Theory and application to the Imperial Valley, California. *Bull. Seismol. Soc. Am.*, 70, 2021-2035, 1980.
- McMechan, G.A., and R.A. Wiggins, Depth limits in body wave inversion. *Geophys. J. R. Astron. Soc.*, 28, 459-473, 1972.

- Minster, J.B., and T.H. Jordan, Present day plate motions. *J. Geophys. Res.*, 83, 5331-5354, 1978.
- Molnar, P., Gravity anomalies and the origin of the Puerto Rico Trench. *Geophys. J. R. Astron. Soc.*, 51, 701-708, 1977.
- Moore, J.C., J.S. Watkins, T.H. Shipley, K.J. McMillen, S.B. Bachman, and N. Lundberg, Geology and tectonic evolution of a juvenile accretionary terrane along a truncated convergent margin: Synthesis of results from Leg 66 of the Deep Sea Drilling Project, southern Mexico. *Geol. Soc. Am. Bull.*, 93, 847-861, 1982.
- Morgan, W., Rises, trenches, great faults and crustal blocks. *J. Geophys. Res.*, 73, 1959-1982, 1968.
- Muller, J.E., Evolution of the Pacific Margin, Vancouver Island, and adjacent regions. *Can. J. Earth. Sci.*, 14, 2062-2085, 1977.
- Nafe, J.E., and C.L. Drake, Physical properties of marine sediments, in *The Sea*, edited by M.N. Hill, Wiley, New York, 3, 794-815, 1963.
- O'Brien, P.N.S., The efficient use of large charges, in *Seismic Refraction Prospecting*, edited by A.W. Musgrave. *Soc. Ex. Geophys.*, 152-170, 1967.
- Oldenburg, D.W., The inversion and interpretation of gravity anomalies. *Geophysics*, 39, 527-536, 1974.
- Orcutt, J., K. MacKenzie, and J.S. McClain, The role of X(p) constraints in linear, extremal inversion of explosion profile data. *Bull. Seismol. Soc. Am.*, 70, 2103-2116, 1980.
- Raitt, R.W., The crustal rocks, in *The Sea*, edited by M.N. Hill, Wiley, New York, 85-102, 1963.
- Riddihough, R.P., and R.D. Hyndman, Canada's active western margin - the case for subduction. *Geoscience Canada*, 3, 269-278, 1976.
- Riddihough, R.P., A model for recent plate interactions off Canada's west coast. *Can. J. Earth. Sci.*, 14, 384-396, 1977.
- Riddihough, R.P., Gravity and structure of an active margin - British Columbia and Washington. *Can. J. Earth. Sci.*, 16, 350-363, 1979.
- Riddihough, R.P., Contemporary movements and tectonics on Canada's west coast: a discussion. *Tectonophysics*, 86, 319-341, 1982.
- Riddihough, R.P., M.E. Beck, R.L. Chase, E.E. Davis, R.D.

- Hyndman, S.H. Johnson, and G.C. Rogers. Geodynamics of the Juan de Fuca plate in Geodynamics of the Eastern Pacific, Caribbean and Scotia Arcs, edited by R. Cabre, editor, Geodynamic series of the AGU (in press), 1982.
- Richards, P.G., Calculation of body waves for caustics and tunnelling core phases. Geophys. J. R. Astron. Soc., 35, 243-264, 1973.
- Richards, P.G., Theoretical seismic wave propagation. Rev. Geophys. Space Phys., 17, 312-328, 1979.
- Rogers, G.C., Seismotectonics of British Columbia. Ph.D. Thesis, Univ. of British Columbia, Vancouver, 224 pp., 1982 (submitted).
- Salisbury, M.H., and N.I. Christensen, The seismic velocity structure of a traverse through the Bay of Islands ophiolite complex, Newfoundland. J. Geophys. Res., 83, 805-817, 1978.
- Savage, J.C., M. Lisowski, and W.H. Prescott, Geodetic strain measurements in Washington. J. Geophys. Res., 86, 4929-4940, 1981.
- Seely, D.R., P.R. Vail, and G.G. Walton, Trench slope model, in The Geology of Continental Margins, edited by C.A. Burk and C.L. Drake, Springer-Verlag, New York, 249-260, 1974.
- Shor, G.G., Refraction and reflection techniques and procedure, in The Sea, edited by M.N. Hill, Wiley (Interscience), New York, 30-38, 1963.
- Shouldice, D.H., Geology of the western Canadian continental shelf. Bull. Can. Pet. Geol., 19, No. 2, 405-436, 1971.
- Scholl, D.W., Sedimentary sequences in north Pacific trenches. In the Geology of Continental Margins, edited by C.A. Burk, and C.L. Drake, Springer-Verlag, New York, 493-504, 1974.
- Snively, P.D., Geophysical data collected on continental margin midway between Washington State and Vancouver, B.C. along Line 19, USGS, S.P. Lee Cruise 3-76: U.S. Geol. Surv. Open File Rep., 81, 895-902, 1981.
- Snively, P.D., and H.C. Wagner, Geologic cross-section across the continental margin off Cape Flattery, Washington, and Vancouver Island, British Columbia. U.S. Geol. Surv. Open File Rep., 81, 978-984, 1981.
- Spudich, P., and J. Orcutt, A new look at the seismic velocity structure of the oceanic crust. Rev. Geophys. Space Phys., 18, 627-645, 1980.
- Talwani, M., L. Worzel, and M. Landisman, Rapid gravity

- computations for 2-dimensional bodies with application to the Mendocino submarine fracture zone. *J. Geophys. Res.*, 64, 49-59, 1959a.
- Talwani, M., G.H. Sutton, and J.L. Worzel, A crustal section across the Puerto Rico Trench. *J. Geophys. Res.*, 64, 1545-1555, 1959b.
- Tiffin, D.L., B.E. Cameron, and J.W. Murray, Tectonics and depositional history of the continental margin off Vancouver Island, British Columbia. *Can. J. Earth. Sci.*, 9, 280-296, 1972.
- Treitel, S., and E.A. Robinson, The design of high resolution digital filters, *IEEE Transactions in Geoscience and Electronics GE-4*, 25-38, 1966.
- Tucker, P.M., and H.J. Yorston, Pitfalls in Seismic Interpretation. *Soc. Ex. Geophys., Monograph Series*, No. 2, 1973.
- Vine, F.J., Spreading of the ocean floor - new evidence. *Science* 154 (3755), 1405-1411, 1966.
- Whittall, K.P., and R.M. Clowes, A simple, efficient method for the calculation of travel times and ray paths in laterally inhomogeneous media. *J. Can. Soc. Ex. Geophys.*, 15, 21-29, 1979.
- Wiechert, E., Ein astatische pendel hoher empfindlichkeit zur mechanischen registrierung von erdbeben. *Beitr. Geophys.* 6, 435-450, 1904.
- Wiggins, R.A., and D.V. Helmberger, Synthetic seismogram computation by expansion in generalized rays. *Geophys. J. R. Astron. Soc.*, 37, 73-90, 1974.
- Wiggins, R.A., Body wave amplitude calculations, II. *Geophys. J. R. Astron. Soc.*, 46, 1-10, 1976.
- Willis, H.F., Underwater explosions, time interval between successive explosions, *British Report WA-47-21*. 1941.
- Wood, L.C., R.C. Heiser, S. Treitel, and P.L. Riley, The debubbling of marine source signatures. *Geophysics*, 43, 715-729, 1978.

Appendix A

WKBJ and ART Algorithms

A.1 WKBJ

The WKBJ synthetic seismogram method (Chapman, 1978) is based upon an approximate solution to the wave equation. The computation of the seismogram reduces to the solution of an ordinary differential equation plus the evaluation of inverse transforms, a frequency and a wave number integral. The innovation in Chapman's method is the technique of evaluating the frequency integral first and keeping the wave number real. This method is relatively inexpensive.

The WKBJ approximation (named after Wentzel, Kramers, Brillouin and Jeffreys)

An approximate solution to the second order equation

$$\frac{d^2\phi}{dx^2} + \omega^2 s^2 \phi = 0 \quad (1)$$

where ω is large and positive, and $s = s(x)$

is required.

Try solutions of the form $\phi = e^{\pm i\omega\tau(x)}$

$$i\omega\tau'' - \omega^2(\tau')^2 + \omega^2 s^2 = 0$$

Approximation 1: neglect $\omega\tau''$

implies:

$$\tau'' \sim \pm s(x)$$

and,

$$\tau(x) \sim \pm \int s(x) dx$$

but,

$$\text{this implies: } \tau'' \sim \pm s'$$

Approximation 2:

$$\text{that } (\tau')^2 = s^2 \pm is'/\omega$$

$$\text{i.e. } \tau' = \pm s + is'/2s\omega$$

then,

$$\tau(x) = \pm \int s(x) dx + (i/2\omega) \ln s$$

The corresponding solution for ϕ is:

$$\phi(x) \sim \frac{A}{s^{1/2}(x)} \exp(i\omega \int s dx) + \frac{B}{s^{1/2}(x)} \exp(-i\omega \int s dx)$$

where:

A and B are constants

This is valid if $|s'/\omega| \ll |s^2|$,

Which amounts to validity if

$$|s' \times \lambda| \ll 2\pi|s|, \quad \text{and}$$

the change in $s(x)$ in one λ must be less than s itself.

This method enables an analytical approximation to the wavenumber integral to be made, avoiding the use of slow and costly numerical solutions in cases where no exact analytical solution exists.

A.2 ART

The asymptotic ray theory synthetic seismogram algorithm (McMechan and Mooney, 1980) employs, as the name implies, asymptotic ray theory (ART). (see Červený et al., 1977; Červený, 1979). The method is approximate, but has the advantage of being valid for laterally varying structures.

Asymptotic ray theory:

Assuming that a time-harmonic solution to the linearised equation of motion:

$$\rho \frac{\delta^2 W}{\delta t^2} = (\lambda + \mu) \nabla(\nabla \cdot W) + \mu \nabla^2 W + \nabla \lambda (\nabla \cdot W) + \nabla \mu \times (\nabla \times W) + 2(\nabla \mu \cdot \nabla) W \quad (1)$$

can be expressed in inverse powers of frequency, ω , we may write an expression for the displacement vector:

$$W = \exp[i\omega(t-\tau)] \sum_{k=0}^{\infty} (i\omega)^{-k} W_k \quad (2)$$

where τ and W_k are independent of ω and t .

W_k = kth amplitude coefficient of the ray series.

It is assumed that the ray series (2) exists and is asymptotic to the exact solution of the equation (1).

The function must be analytic and thus the ray expansion (1) is not valid in the vicinity of those points where the T-X curve associated with the propagating wave has end points, cusps, tangent points with the T-X curve of another wave, or, generally, discontinuous derivatives.

Due to the fact that the solution (2) is expressed as an asymptotic expansion in inverse powers of frequency, it yields best results for high frequencies. Except in the close neighbourhood of singular points, the error which arises in keeping only the first few terms in the series tends to zero as ω increases. In many cases it is sufficient to consider only the leading term in (2). Then:

$$W = \exp[i\omega(t-\tau)] W_0$$

This is the zero-order solution, which is the solution obtained according to the principles of geometrical optics.

The zero-order ART algorithm may be expressed by:

$$A = A_0 L^{-1} \prod_j k_j$$

where A = the total complex amplitude associated with a ray

A_0 = the initial amplitude

L = the geometrical spreading, and

Π = the serial product over all the j complex plane-wave transmission and reflection coefficients (k) along the ray path.

The synthetic arrival is constructed by performing a ray trace along which travel time, distance and $\prod_j k_j$ are summed. The amplitude computation proceeds by calculating the area of an element of wave-front surface by determining the distances between points of equal travel time on adjacent rays.

Limitations of WKBJ Algorithm:

- 1) Not strictly correct for waves turning in the vicinity of a low velocity zone or a velocity discontinuity.
- 2) Diffractions beyond triplications or precritical reflections from velocity gradient zones are not correctly calculated. When the geometrical amplitude on a wavefront suddenly changes as in a true shadow, or at a rapid change in velocity gradient, there are two diffraction effects (Chapman, personal communication 1982);

- (a) The geometrical effect of having an incomplete wavefront; completely analagous to classical Fresnel diffraction and accurately described by the WKBJ seismogram method.
 - (b) The non-geometrical diffraction effect depending on the frequency dependent boundary conditions; not described by WKBJ method.
- 3) There is an end-point error from the bottom of the model, but this can be made negligible by making the lowest model boundary sufficiently deep.

Limitations of ART Algorithm

- 1) The zero-order approximation, by definition, excludes arrivals that originate in the higher order terms, such as head waves.
- 2) The method is based on ray theory and thus does not produce wave effects, such as diffractions.

There are two sources of differences between the results obtained using ART and WKBJ.

- 1) The different methods of velocity interpolation employed: ART uses cubic splines whereas WKBJ employs a linear interpolation scheme.
- 2) Different approaches to the physics of energy propagation: WKBJ is an approximate wave-type solution, ART is an approximate ray-type solution.

A comparison of the effects produced by the different algorithms is given in section 4.4.

Appendix B

Instrumentation and data digitization

The ocean bottom seismographs used were of the free fall, pop-up type similar to those described by Lister and Lewis (1976) and Johnson et al., (1977). The spherical OBS package descends at 3 m s^{-1} with the 12 cm thick, 300 kg, concrete anchor attached and is later (usually less than 15 days) released by programmed or acoustic command.

The instrument records signals at a tape speed of 1 mm/s in continuous direct AM mode, from one vertical and two horizontal 4.5 Hz geophones with a 20 Hz time code in the first channel. The overall frequency response of the system is bandlimited between 2 and 100 Hz. Square root signal compression increases the dynamic range, but gives poor signal reproduction fidelity and only approximate amplitudes.

The OBS data tapes are then transcribed from AM to FM at a playback speed of 15/16 inch per second (ips) and a recording speed of 15 ips. The FM tape is then played back at a speed of 15/16 ips for digitization at a sampling rate of 312.5 sps. The overall effect of this process is to give a real-time data sampling rate of approximately 200 sps. The actual sampling rate varies with time and the different instruments due to minor variations in tape drive motor speed and a small degree of tape stretching. In practice, the sample rate fluctuations lead to timing errors of less than 0.003 s, i.e. insignificant in comparison with origin time and picking errors.

Appendix C

Chevron Multichannel Data:

In 1972, Chevron Standard Limited ran a number of multichannel, seismic reflection profiles perpendicular to the continental slope from the deep water to part of the way up the slope. One of these profiles (113-H) crosses the VISP-80 profile-I at an oblique angle, diverging by a maximum of 17 km laterally at the eastern end. Figure C.1 shows the stacked

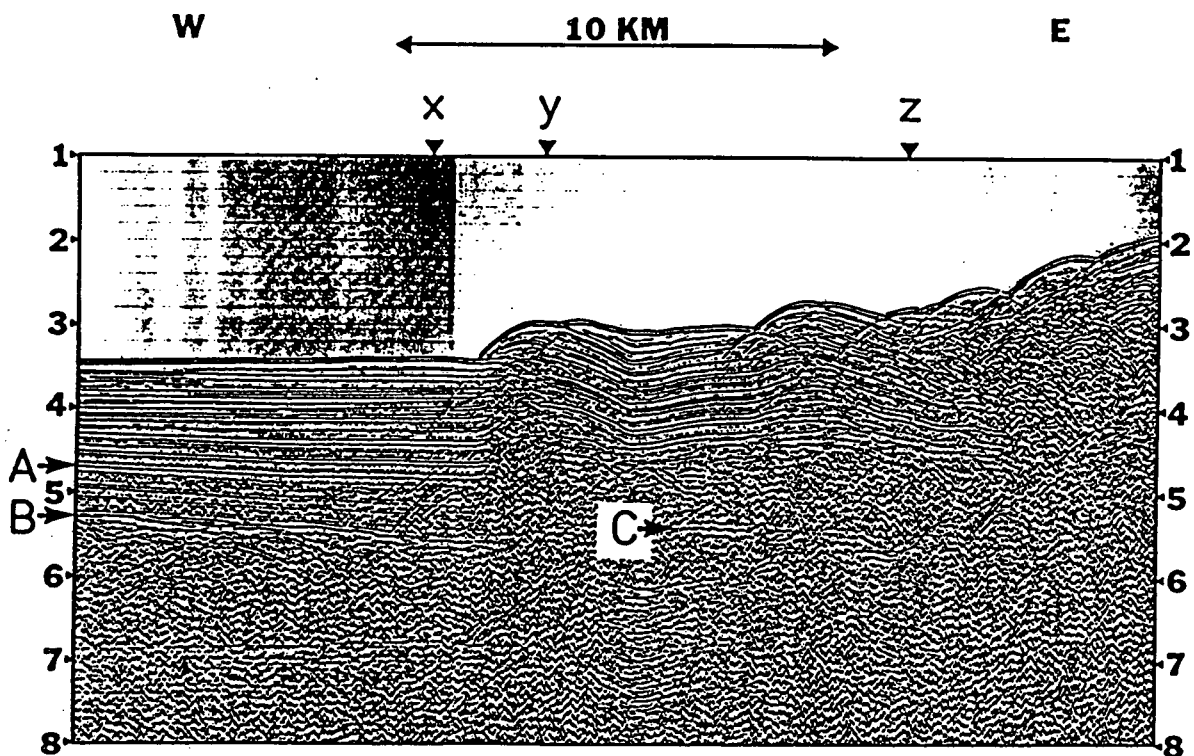


Figure C.1 Chevron Standard multichannel data.

The stacked record section is compiled from 2400%, 24 channel, common reflection point data. Automatic gain control, bandpass filtering and a standard deconvolution process have been applied.

Horizon A is the boundary between the 1.8 km/s and 2.3 km/s regions used in the seismic modelling.

Horizon B is the reflection corresponding to the basement.

Horizon C is the continuation of the basement beneath the continental rise; displaced upwards due to velocity pull-up.

X, Y, and Z are the positions at which NMO velocities were calculated by Chevron Standard Ltd.

record section compiled from 2400% common reflection point data. As has been noted elsewhere (Clowes and Knize, 1979), the data quality is excellent.

To the west there is an upper sequence of plane layered, high amplitude, reflections to a time of approximately 4.8 s two way travel time (T.W.T.T.), (horizon A, figure C.1). This corresponds to the 1.8 km/s velocity region used in the seismic modelling. Below these layers the character of the section changes, the layering is less distinct and the amplitudes are not as pronounced, implying a greater degree of compaction of the material; this is the 2.3 km/s velocity region used in the modelling. A strong, irregular reflection which is clearly identified with the basaltic basement is seen at approximately 5.4 s (horizon B, figure C.1). The appearance of reflectors below this horizon, at approximately 7 s, is due to the presence of water bottom and sedimentary layer multiples.

The oceanic basement is clearly seen dipping to the east, whilst the overlying sediments here have a fan structure (the upper layers being parallel to the sea floor, the lower ones being parallel to the dipping basement).

At the western edge of the continental rise there is a radical change in the character of the section. This is due to the presence of fault-bounded ridges, behind which sediments are ponded (see figure 1.3). The arching of reflecting horizons below the surface expression of the ridges is partly a real effect and partly a result of velocity pull-up (see Tucker and Yorston, 1973), due to replacement of part of the

water column with sub-bottom material.

The continuation of basement beneath the continental rise can be seen (horizon C, figure C.1), displaced upwards due to the velocity pull-up. If the basement dip is assumed to be constant along the whole section then a value for the average sediment velocity under the rise may be obtained from the degree of pull-up (0.3 s T.W.T.T. in this case). The derived velocity is 2.0 km/s; consistent with airgun data obtained over the rise (see section 4.7.1).

TIME	X	Y	Z
2.8			4900
3.0		4900	5000
3.2		4950	5100
3.4	4900	5000	5200
3.6	4950	5000	5200
3.8	5000	5200	5400
4.0	5050	5250	5500
4.2	5150	5350	5700
4.4	5200	5500	5800
4.6	5300	5600	5900
5.0	5400	5700	6100
5.2	5600	6000	6500
5.4	5750	6200	6600
5.6	5900	6400	6800
5.8	6100	6800	7000
6.0	6400	6700	7200
6.5	7200	7500	7600
7.0	8000	8000	8000
8.0	9000	9000	9000

Table C.1 NMO velocities at positions X, Y, and Z (figure C.1). Time is T.W.T.T.(s); velocities in ft/sec.

The normal move-out velocities employed (table C.1) in the data processing were used to generate a v-z curve by use of the Dix (1955) equation:

$$v_n^2 = (v_{r.m.s,n}^2 t_n - v_{r.m.s,n-1}^2 t_{n-1}) / (t_n - t_{n-1})$$

where:

- v_n = interval velocity for nth layer
 $v_{r.m.s,n}$ = r.m.s. velocity for nth reflection, and
 t_n = travel time to nth reflection

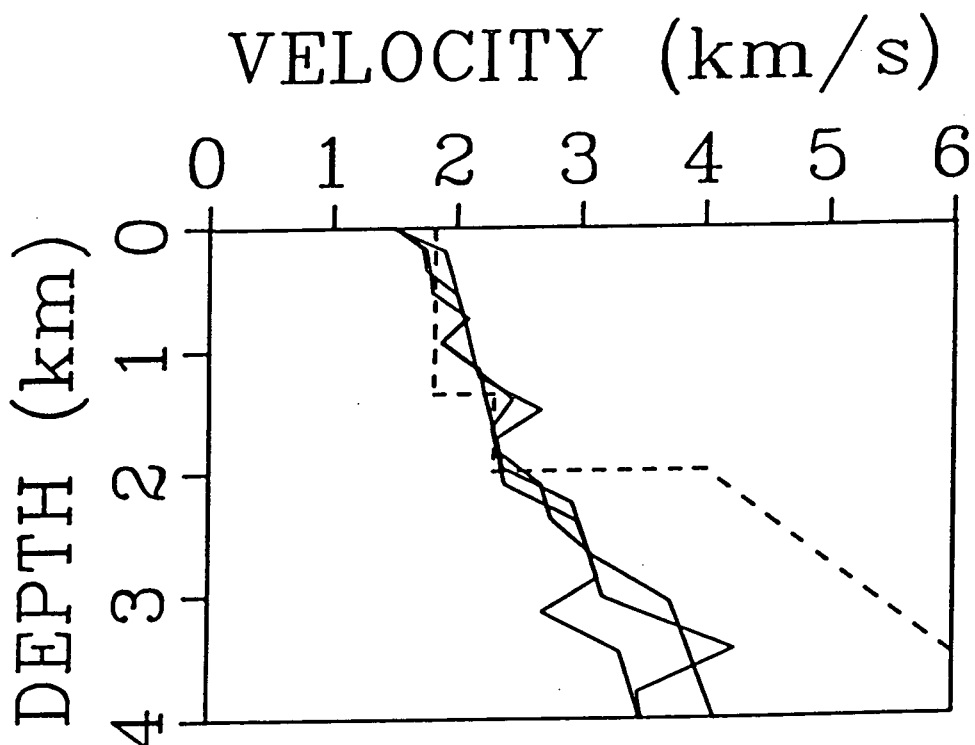


Figure C.2 V-Z structure derived from NMO velocities.

Solid lines represent the velocity-depth curves obtained from NMO velocities at positions X, Y, and Z (figure C.1). The dashed line is the preferred velocity structure just west of the continental rise. Note the divergence of values below the basement level (2 km), which reflects the company's interest in sediment layer information.

The v-z curves (figure C.2.) were generated by adding the terms Vt down to a given reflector, n.

As can be seen from the figure, the agreement between the model velocities and the interval velocities is good. Although use of the Dix formula to determine the v-z structure is an unstable process, the consistency between used and derived values is encouraging. The divergence of values below the basement reflects the lack of resolution of NMO curves at greater depths and the company's interest in sediment layer information.

Appendix D
Shell Cygnet Well

In 1968 Shell Canada limited drilled an exploratory well in the Tofino basin: The Shell Anglo Cygnet Well (Shouldice, 1971). At 48° 19' 40" N, 125° 43' 57" W (see figure H.1) the site is 18 km south-east of OBS #5.

In the spring of 1969 gamma ray and sonic logs were taken down the 2 km deep well. The velocity-depth curve calculated from the interval transit times is given in figure D.1. The velocity variation agrees well with that derived from the OBS #5 airgun data. Geological horizons proposed by Snively and Wagner (1981) have been roughly correlated with features in the sonic log.

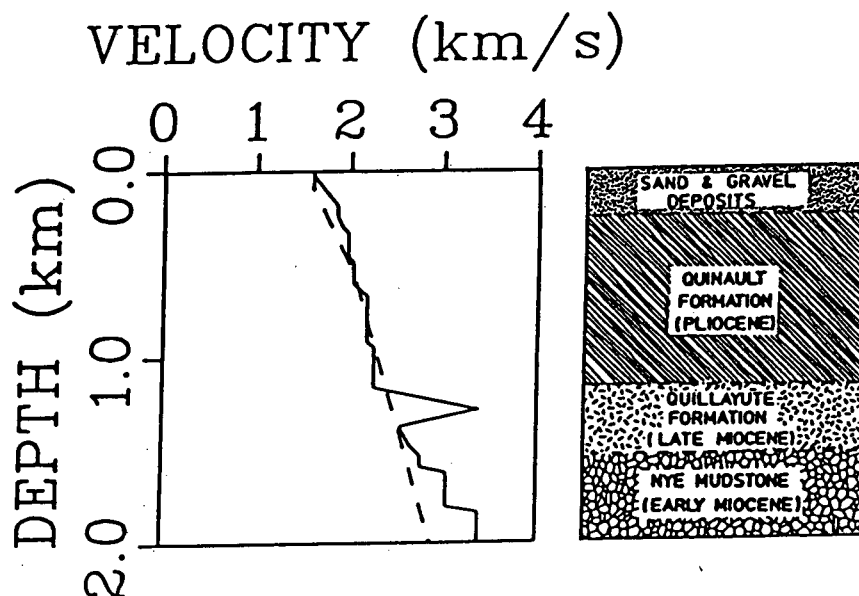


Figure D.1 Sonic log derived velocity structure and geological interpretation.

Solid line is the velocity-depth curve calculated from interval transit times obtained down the Shell Anglo Cygnet well. Dashed line is the structure derived from the OBS #5 airgun data. The geological interpretation on the right is that proposed by Snively and Wagner (1981).

Appendix E
Structure of the Moho

The Mohorovičić discontinuity is most often interpreted as a step-function velocity boundary, although a change in velocity gradient (Au, 1981) and a laminated character (Fuchs, 1969) have also been considered.

Near vertical deep crustal reflection profiling is the most diagnostic method of examining the fine structure of the crust-mantle transition zone (Hale and Thompson, 1982) due to the large data density and high input frequencies used.

Analysis of refraction data, involving a turning ray interpretation of first arrivals, is very poor at resolving features (e.g. discontinuities) in the v-z structure (see section 2.2), but clear sub-critical reflections are diagnostic in this regard.

The variation in character of a record section depending upon the form of the crust-mantle transition has been discussed by Braile and Smith (1974) and Davydova (1975). The various types of Moho considered are illustrated in figure E.1., whilst the effects of these structures on synthetic data is summarised in table E.1.

Structure Type	Effect on seismic data
Step-function boundary	Pre-critical reflection amplitudes increase with velocity contrast, while the critical point moves closer to the source.
Gradient zone	Pre-critical reflection amplitudes very low.
Step with gradient	Large amplitude head waves from below the boundary.
Step with decrease below	Amplitude of head waves from below the boundary very low.
Laminated transition zone	Large amplitude sub-critical reflections for some frequencies, due to constructive interference.

Table E.1. The effects of Moho structure type on seismic data.

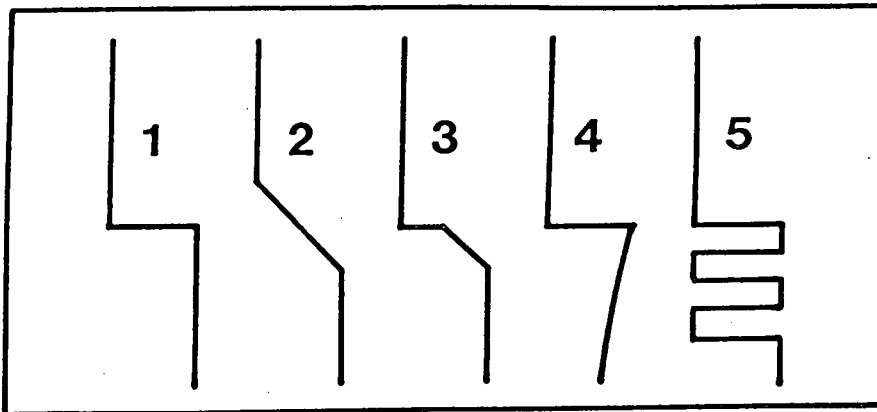


Figure E.1 Possible velocity variations at the Moho.

- (1) Step-function velocity boundary
- (2) High velocity-gradient transition zone
- (3) Velocity contrast with gradient region below
- (4) Velocity contrast with velocity decrease below
- (5) Thin laminated layer transition zones.

The resolution of Moho structure that may be obtained with marine refraction data is very poor. This is due to the inherent data errors and the characteristically long source signature (see appendix F). It should also be remembered that if the Moho is interpreted as a change in velocity gradient (from high to low) , enabling only turning rays above the boundary to be interpreted, then each data set samples the Moho at only one place. Thus, as noted (section 4.5), 3 OBSs will weakly constrain the Moho depth at only 3 places. Lateral heterogeneities in Moho depth of the type which have been inferred from high density reflection data (e.g. Clee et al., 1974) may well be present but are not detectable with refraction data.

Appendix F

Bubble Pulse Oscillations

The long source wavelet characteristic of marine seismic work is a product of bubble pulse oscillations.

The problem is caused by successive oscillations of the gas bubble generated by the energy source. Each cycle of the oscillating bubble corresponds to a signal propagating outward. The source wavelet recorded is then a train of wavelets generated by the individual cycles. The number of pulses and their periods are primarily a function of detonation depth and of the energy released during creation of the bubble. The length of the compound wavelet depends on the number of expand-collapse cycles of substantial energy performed by the bubble before it collapses completely or vents to the atmosphere.

The elimination of bubble pulse effects by compression and simplification of the compound wavelet signature has been attempted by using various methods. Wood, Heiser, Treitel and Riley (1978) employ Wiener shaping filters (Treitel and Robinson, 1966) in their algorithm. This method has the disadvantage that the choice of filter length (an unknown parameter) is critical. Levy and Clowes (1980) have used a generalized linear inverse approach which has the advantage that the solution accuracy may be made consistent with observational errors. The disadvantage of this procedure is that it is computationally expensive.

The period, τ , of the first oscillation of the gas bubble

generated by the explosion may be related to the shot depth, d , and the charge weight, W , by the Rayleigh-Willis bubble formula (Willis, 1941):

$$\tau = \frac{2.13 W^{1/3}}{(d + 10)^{5/6}}$$

where W = energy of the explosion expressed as explosive weight in TNT equivalents.

The maximum possible source signal strength is obtained at optimum depth: where the water reverberation frequency is equal to the bubble oscillation frequency. This is the criterion used to compute the most desirable detonation depths for the various shot sizes.

Appendix G

2-D Gravity Modelling Algorithm

This algorithm computes the gravitational attraction due to individual polygons, of given density, at different depths and calculates the total force per unit mass which would be measured at any point on the surface. Any two-dimensional structure may be modelled to any required degree of accuracy, by considering a sufficiently large number of polygons.

Analytic expressions for the vertical and horizontal components of gravitational attraction due to an arbitrary polygon are derived below:

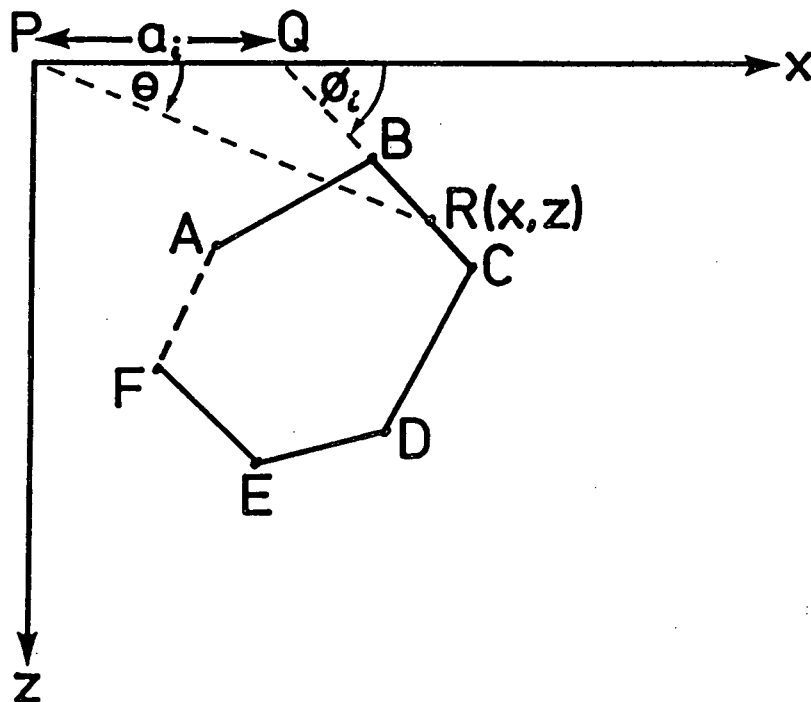


Figure G.1 Geometrical elements involved in the gravitational attraction of an n-sided polygon (after Talwani et al., 1959).

ABCDEF (figure G.1) is a polygon with n sides and P is

the point at which the gravitational attraction is to be computed. Hubbert (1948) shows that the vertical component of the attraction due to such a two-dimensional body is equal, at the origin, to

$$2G\rho \int z d\theta$$

where the line integral is taken along the periphery of the body,

G is the universal constant of gravitation, and ρ is the volume density of the body.

The corresponding expression for the horizontal component of gravitational attraction is given by

$$2G\rho \int x d\theta$$

(Talwani et al., 1959a). Computation of the contribution to $\int z d\theta$ from BC:

$$z = x \tan \theta$$

for any arbitrary point R on BC, also:

$$z = (x - a) \tan \phi$$

from (1) and (2):

$$z = \frac{a \tan \theta \tan \phi}{\tan \phi - \tan \theta}$$

or:

$$\int_{BC} z d\theta = \int_B^C \frac{a \tan \theta \tan \phi}{\tan \phi - \tan \theta} d\theta = z$$

similarly

$$\int_{BC} x d\theta = \int_B^C \frac{a \tan \phi}{\tan \phi - \tan \theta} d\theta = x$$

The vertical component of gravitational attraction, V , and the

horizontal component, H, due to the whole polygon, are then given respectively by:

$$V = 2G\rho \sum_{i=1}^n Z_i$$

$$H = 2G\rho \sum_{i=1}^n X_i$$

- the summations being made over the n sides of the polygon.

The integrals involved in the expressions for Z_i and X_i may be easily solved analytically; for details see Talwani et al., (1959a).

Appendix H

U.S.G.S. Multichannel Data

A 24-channel seismic-reflection profile was collected aboard the U.S. Geological Survey R/V S.P. Lee (Snively, 1981), and a geological cross section has been constructed, based on the section (Snively and Wagner, 1981). The profile extends northeastward (figure H.1) from the abyssal plain near latitude $48^{\circ} 00' N$ and longitude $126^{\circ} 43' W$, passes 1 km south of the Shell Anglo Cygnet exploratory well (Appendix D), and terminates at a point on the coast of Vancouver Island just southeast of Nitinat Lake.

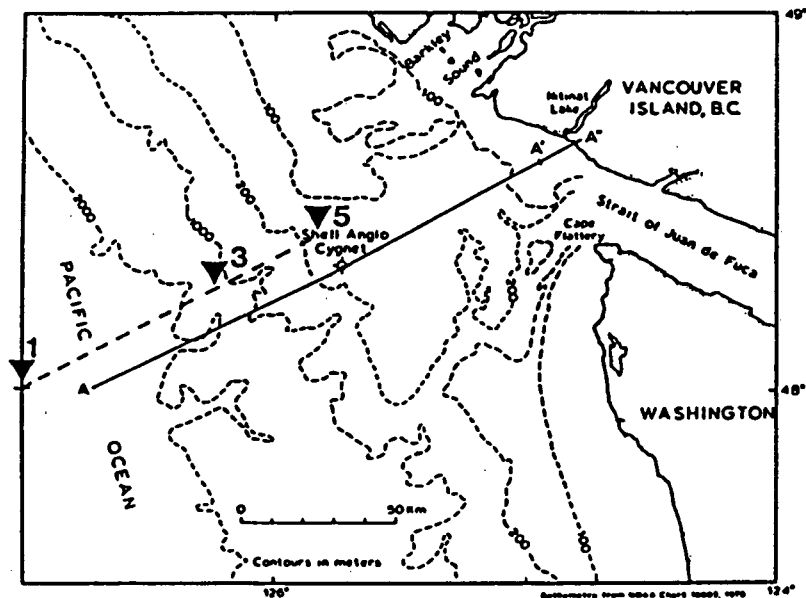


Figure H.1 Location map of the U.S.G.S. multichannel section.

The 24 channel seismic reflection profile extends northeastward from A to A". The positions of the three OBSs, #1, #3, and #5 are indicated by the inverted triangles. Note the position of the Shell Anglo Cygnet well (see Appendix D for details).

The section (figure H.2) was obtained using a tuned array of five airguns totalling 1326 in³ as a sound source. The recording system consisted of a 24 - channel streamer and a Global Universal Science model 4300 digital recording instrument. The lower diagram in figure H.2 is the geological

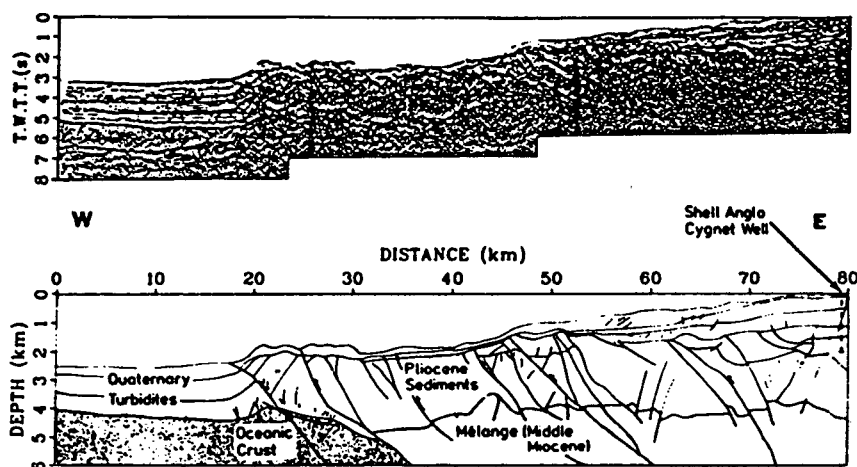


Figure H.2 U.S.G.S. multichannel data and geological interpretation.

Upper: 24 channel seismic reflection data obtained along the profile extending from 'A' to the position of the Shell Anglo Cygnat well (see figure H.1). The data are unmigrated.

Lower: A geological interpretation based on the multichannel data (after Snavely and Wagner, 1981). The structural horizons which were picked on the travel time section have been rescaled to depth by using the refraction velocities derived in the VISIP-80 data interpretation (Chapter 4).

Note the position of the Shell Anglo Cygnat well at the eastern end of the section.

interpretation of the multichannel profile. The structural horizons which were picked on the travel time section have been rescaled to depth by using the refraction velocities derived in the interpretation of the VISIP-80 data set (see Chapter 4). The cross section indicates Quaternary and upper Tertiary strata which have been deformed into a series of asymmetric folds and northeastward dipping imbricate thrusts.

These compressive structures are thought to result from the relative northeastward underthrusting of the Juan de Fuca plate beneath the North America plate.

The interpretation of Snavely and Wagner proposes the existence of a mass of highly sheared and compressed *mélange* lying beneath the sediments of the continental rise. This middle Miocene unit is thought to have been uplifted prior to deposition of the continental slope Pliocene strata.